NASA CONTRACTOR REPORT

NASA CR-2574

STUDY OF NOISE SOURCES
IN A SUBSONIC FAN USING MEASURED
BLADE PRESSURES AND ACOUSTIC THEORY

Donald B. Hanson

NATIONAL AERONAUTICS AND SPACE ADMINISTRATION · WASHINGTON, D. C. · AUGUST 1975

1. Report No. NASA CR -2574	2. Government Accession No.	3. Recipient's Catalog No.
4. Title and Subtitle Study of Noise Sources in a Subsonic Fan Using Measured Blade Pressures and Acoustic Theory		5. Report Date AUGUST 1975
		6. Performing Organization Code
7. Author(s) Donald B. Hanson		8. Performing Organization Report No.
		10. Work Unit No.
9. Performing Organization Name and Address Hamilton Standard, Division of United Technologies Corp. Windsor Locks, Connecticut 06096		11. Contract or Grant No. NAS 1-12505
		13. Type of Report and Period Covered Contractor Report
12. Sponsoring Agency Name and Address National Aeronautics and Space Administration Washington, D. C. 20546		14. Sponsoring Agency Code

15. Supplementary Notes
FINAL REPORT

16. Abstract

Sources of noise in a 1.4m (4.6 ft) diameter subsonic tip speed propulsive fan running statically outdoors are studied using a combination of techniques.

Signals measured with pressure transducers on a rotor blade are plotted in a format showing the space-time history of inlet distortion. Study of these plots visually and with statistical correlation analysis confirms that the inlet flow contains long, thin eddies of turbulence. Turbulence generated in the boundary layer of the shroud upstream of the rotor tips was not found to be an important noise source.

Fan noise is diagnosed by computing narrowband spectra of rotor and stator sound power and comparing these with measured sound power spectra. Rotor noise is computed from spectra of the measured blade pressures and stator noise is computed using the author's stator noise theory. It is concluded that the rotor and stator sources contribute about equally at frequencies in the vicinity of the first three harmonics of blade passing frequency. At higher frequencies, the stator contribution diminishes rapidly and the rotor/inlet turbulence mechanism dominates.

Two parametric studies are performed by using the rotor noise calculation procedure which was correlated with test. In the first study, the effects on noise spectrum and directivity are calculated for changes in turbulence properties, rotational Mach number, number of blades and stagger angle. In the second study the influences of design tip speed and blade number on noise are evaluated.

17. Key Words (Suggested by Author(s))		18. Distribution Statement
Acoustic Noise	Propulsion Noise	
Noise Theory	Inlet Turbulence	
Fan Noise	Blade Pressure	
		Subject Category 71

19. Security Classif. (of this report) Unclassified	20. Security Classif. (of this page) Unclassified	21. No. of Pages 137	22. Price* $5.75

CONTENTS

iii

STUDY OF NOISE SOURCES IN A SUBSONIC FAN
USING
MEASURED BLADE PRESSURES AND ACOUSTIC THEORY

By Donald B. Hanson
Hamilton Standard
Division of United Technologies Corporation

SUMMARY

Sources of noise in a 1.4m (4.6 ft) diameter propulsive fan designed to operate at subsonic tip speeds were studied using a combination of theoretical, experimental, and computer plotting techniques developed specifically for diagnostic purposes. With the fan running statically outdoors, the dominant sources of both random and tone noise were found to be interaction of the rotor with inlet turbulence and interaction of the stator with wakes from the rotor blades.

To assess the structure of inlet turbulence, a technique was developed whereby signals measured from pressure transducers on a rotor blade are plotted in a format showing the space-time history of inlet distortion. Study of these plots visually and with statistical correlation analysis confirms that the inlet flow contains long, thin eddies of turbulence. Turbulence generated in the boundary layer of the shroud upstream of the rotor tips was not found to be an important noise source. However, this boundary layer does contain large amplitude velocity disturbances caused by the inlet turbulence which, could be an important cause of rotor noise in fans with inlets having diffusion upstream of the rotor.

Fan noise was diagnosed by computing narrowband spectra of rotor and stator sound power and comparing these with measured sound power spectra. Rotor noise was computed from spectra of the measured blade pressures via an improved version of the theory published previously by the author for rotor noise due to atmospheric turbulence (J. Acoust. Soc. Am., vol.56, no. 1, July 1974). Stator noise was computed using empirical cascade loss coefficients and a strip analysis version of the author's stator noise theory (J. Acoust. Soc. Am., vol. 54, no. 6, Dec. 1973). The work summarized in this report showed that the rotor and stator sources contribute about equally at frequencies in the vicinity of the first three harmonics of blade passing frequency. At higher frequencies, the stator contribution diminishes rapidly and the rotor/inlet turbulence mechansim dominates. These conclusions apply equally to broadband and tone spectrum components.

Two parametric studies were performed by using the rotor noise calculation proceedure correlated with test as described above. In the first study, the effects on noise spectrum and directivity were calculated for changes in turbulence length scales, rotational Mach number, number of blades, stagger angle, and modulation parameters. Trends in this study provide the background for use of the theory as a diagnostic tool. In the second study the influences of design tip speed and blade number on noise were evaluated. The study shows reduced noise for designs with many blades and low tip speed.

The accuracy of any theoretical prediction proceedure for rotor dipole noise depends on ability to assess unsteady blade loads. The currently available lift response theories are not adequate at the high Mach numbers and frequencies where propulsive fans operate. This problem was avoided in the noise diagnosis section of this report by measuring surface pressures with blade-mounted transducers, but could not be avoided in the parametric studies. In studying the measured blade pressure spectra, two discoveries were made. First, the blade load harmonic peaks, L_n, for harmonic order n obeyed the Lowson-Scheiman loading law (J. Sound and Vibration, Vol. 9, No. 2, March 1969) out to n = 100 or more. (The law states that, on a log - log plot, the harmonic loads fall on a straight line: $L_n = L_o n^{-k}$). In fact, the form of this empirical relation was shown to be a consequence of the theoretical model used for blade response to inlet turbulence. The second discovery was that the intercepts and slopes (L_o and k) varied in an unexpected way with fan operating conditions. In particular, it was found when the fan was operated at constant pressure ratio, but varying tip speed and blade angle, that the blade unsteady loads dropped with increasing tip speed, contrary to expectations. This effect may be caused by the change in steady blade lift coefficient and should be explored for its potential as a noise reduction method.

2

SECTION 1
INTRODUCTION

Inside a propulsive fan, the airflow which participates in noise generation is so complex as to be impractical to define completely either by current analytical methods or by experimental techniques. Swirling wakes interact with boundary layers, strong pressure and shear gradients exist, and compressibility is an important factor. In general, the flow is highly turbulent and three dimensional. Noise is generated by the interaction of these flows with solid surfaces or, in some cases, by flow-flow interactions (quadrupole sources). Calculation of noise requires knowledge of pressure distributions over the surfaces and of velocity products throughout the volume.

With this complexity, it may seem futile to model the noise generation process as a set of monopole, dipole, and quadrupole mechanisms each operating more or less independently. However, in recent years, this technique has been very profitable partly because of great advances in acoustic theory but mostly because of new data measurement and analysis techniques. For example, internal flows at a high Mach number and high frequency can be measured with hot wire anemometers and miniature transducers can be installed on stationary and rotating surfaces. Modern signal analyzers can calculate spectra, correlation functions, and signal enhanced waveforms in real time. The use of computers for data analysis is becoming commonplace, particularly through implementation of the fast Fourier transform and computer plotting.

In this report, experience with all of these tools is brought to bear on the problem of identifying the dominant noise generation mechanisms in a subsonic tip speed fan running statically. The test vehicle is the Hamilton Standard Q-Fan^{TM} Demonstrator, a 1.4 meter (4.6 ft) diameter, 1.18 design pressure ratio, single stage fan designed for low noise propulsion. The analytical tools in this study are extentions and detailed applications of fan noise source analysis methods published previously (refs. 1 and 2).

The organization of the report is as follows. Section 2 briefly reviews the previous analysis methods, previous results of hot wire and blade pressure measurements, and an apparent paradox on sources of rotor inlet turbulence. Section 3 describes the facility, instrumentation, and experimental program used to acquire data for analysis in this report. Section 4 is a diagnosis of inlet turbulence using a new computer technique for plotting signals from blade-mounted pressure transducers. In Section 5 the fan noise is diagnosed using the same blade pressure signals to compute rotor noise and a strip analysis version of reference 1 to compute rotor/stator interaction noise. Section 6 presents results of parametric studies using the rotor noise prediction methodology. Conclusions from the report are summarized in Section 7. Some mathematical details from Section 5 are given in appendices.

SECTION 2
BACKGROUND

A brief review is given below of previous results which directly influenced the design of the experiments and the development of analytical methods used in this study.

Structure of Inlet Turbulence

It has been recognized for some time that turbulence in the flow entering a fan rotor can cause significant noise by interacting with the blades. Hanson (refs. 2 and 3) used hot wire anemometers to establish the structure of turbulence typically entering an inlet during an outdoor static fan test in a relatively unobstructed environment. Even with winds of only 1 to 3 knots, turbulence levels in the 3% to 4% range were found entering the 53 cm diameter inlet. Turbulence length scales can be inferred from the correlegrams in figure 2. The autocorrelation coefficient at the top shows that the inlet flow disturbances tend to be correlated for times up to about 1/2 second. At the inlet velocity of 70 m/sec this corresponds to turbulent eddies with apparent length of 35 meters. The transverse correlation coefficient shown at the bottom in figure 2 suggests a transverse scale of 6 to 8 cm corresponding to a probe separation of 30°. These measurements led to the image of long, thin "sausages" of turbulence being sucked into the inlet.

Some of the velocity signals had correlation functions with two sections as shown in figure 3. This suggests two basic scales in the turbulence: one very long which would produce a partially coherent (tone like) rotor noise component and one very short which would produce a broadband noise component.

The mechanism for development of the long, thin eddies is suggested at the top in figure 4 where turbulence generated by wind over the earth's surface or over obstacles is stretched as it is drawn into the inlet. The streamlines shown correspond to static operation. In forward flight, the streamlines would be as shown at the bottom in figure 4 resulting in little modification of the turbulence.

Rotor Noise
Caused By Inlet Turbulence

The longer eddies in the inlet flow are interferred with many times by the blades as they pass through the rotor. In order to calculate the resulting noise, this interference was modeled as an eddy chopping process in reference 2. As it is chopped, each eddy causes lift pulses to occur on a blade once per revolution and sound pulses

to occur B times per revolution for a rotor with B blades. The pulse statistics were handled with the aid of random envelope functions whose lengths corresponded to the eddy lengths and therefore determined how many times any eddy was chopped. It was shown that eddies long enough to produce 50 or more pulses would produce sound with a spectrum containing peaks at blade passing frequency harmonics which are so narrow as to appear like true tone components. Thus, it was shown that despite being a random phenomenon, turbulence can produce noise with nearly the characteristics of a tone.

<div align="center">

The Shroud Boundary Layer
as a Source of Turbulence

</div>

Cumpsty and Lowrie (ref. 4) studied two sources of rotor inlet turbulence as causes of the tone at blade passing frequency: the atmospheric turbulence described above and the turbulence generated in the boundary layer of the shroud, upstream of the rotor blade tips. They concluded from correlations of boundary layer thickness with tone levels that the boundary layer was an important contributor under some circumstances. In particular, they concluded that at low subsonic tip speeds the boundary layer was the dominate cause of tone noise whereas at higher subsonic tip speed atmospheric turbulence was dominant.

Now, the idea of boundary layer turbulence as a cause of tone like noise is difficult to accept if one thinks in terms of classical flat plate boundary layers. The measurements of Favre, et al (ref. 5) and of Schubauer and Klebanoff (ref. 6) both suggest eddy lengths in the streamwise direction up to about 3/4 of the boundary layer thickness and transverse dimensions about 3 times smaller based on integral lengths scales. Since any one of these eddies would be chopped by no more than one blade, this sort of boundary layer turbulence could not result in tone noise.

To resolve the observations of Cumpsty and Lowrie with this fundamental contradiction, a test was designed in which unsteady surface pressures were measured on a rotor blade. One transducer was placed near the blade tip so as to scrub in the shroud boundary layer and one transducer was placed well away from the tip so as to be influenced only by turbulence from outside the fan. The results which are described in detail in Section 4 show that thinking in terms of classical boundary layers is too simlistic for this problem. Disturbances with very long correlation times do indeed appear in the boundary layer. However, these are not boundary layer turbulence in the usual sense but disturbances impressed on the boundary layer by turbulence in the outer flow. This effect is shown clearly by blade pressure waveform plots in Section 4.

6

SECTION 3
DESCRIPTION OF TEST

This section describes the test fan and instrumentation used to acquire the sound and blade pressure data analyzed later in the report. Test conditions, ambient conditions, and corresponding run numbers are identified.

Test Facility

The test vehicle for the program was the Hamilton Standard Q-Fan Demonstrator. Since the Q-Fan geometry, performace, and noise have been fully described by Levintan (ref. 7), only a brief discussion is given here. Figure 5 is a section view of the fan showing the bellmouth inlet and major components. The 13 bladed rotor has variable pitch so that a given pressure ratio can be achieved at a variety of tip speeds and blade angles. At the design blade angle the axial distance from rotor trailing edge to stator leading edge is about 2 blade chords. The stator, with 7 vanes, serves to straighten the exit flow and to support the core engine, gearbox, and rotor assembly. No attempt was made to suppress the tone at blade passing frequency by use of many vanes (acoustic cutoff) because it appears at approximately 700 Hz where it has little influence on noise ratings. The design pressure ratio of the fan is 1.18 at a tip speed of 247 m/sec (810 ft/sec) and a blade angle of 56° measured at the 3/4 radius. However the maximum pressure ratio tested was 1.15 due to limited power of the core engine.

Figure 6 shows the fan installed on the test stand. The core engine noise suppressor shown in the figure was removed for the test described here because of noise caused by the fan jet interferring with the suppressor supports (ref. 5). The platform under the fan is open grill work to minimize the formation of inlet vortices. The guard rail was removed for the test. With its location well above the ground in an unobstructed area, the fan environment was considered nearly ideal for an outdoor noise test.

Test Instrumentation

Far-field noise data were measured by a redundant pair of microphones at the fan centerline height of 6 meters. These indexed around the fan on a 7.62 meter (25 ft) arc, stopping every 10°. The acoustic platform shown in figure 6 halfway between the fan and the traveling microphones moved with the microphones to minimize the influence of noise reflected from the ground.

Two miniature pressure transducers were installed on one blade in a manner to respond strongly to disturbances in the inlet flow. A similar installation from a different program is shown in figure 7. In the present application the middle location was omitted and the tip location was only 1/3 as far from the tip. Thus, the tip transducer was 0.6 cm (0.25 in.) from the tip, where the fan shroud boundary layer was expected to be most turbulent, and the mid blade transducer was 8.9 cm (3.5 in.) from the tip, or well outside the shroud boundary layer. The chordwise location was 0.078% chord from the blade leading edge on the pressure side of the blade. (The pressure side was chosen to avoid confusion due to a possible leading edge separation bubble). Transducers and leadwires were installed flush with the blade surface and care was taken to strain-isolate the transducer cases from the blade so that blade bending would not influence output.

Blade pressure signals were recovered via slip rings inside the spinner. Rotating amplifiers were used to boost signal levels well above slip ring electrical noise. The microphones, blade pressure transducers, and the FM recording system had frequency responses essentially flat to 20 kHz. The excellent signal-to-noise ratio as a function of frequency is illustrated in figure 8. For these two spectra the only difference in the record/playback/analysis procedure and parameters was that the transducer excitation was off for the plot labeled "electrical noise". Thus, the slip ring noise, tape noise, spectrum analyzer floor, etc. are well below the signal level across the entire audio spectrum.

Test Conditions

All the data analyzed in this report were recorded early on the morning of March 26, 1974. Noise and blade pressure data were simultaneously recorded first with and then without an intentional inlet flow distrubance as shown in figure 9. As shown later, the purpose of the post in the inlet was to produce noise which could be related to a measured blade pressure signal. For both configurations the fan was run at a series of points with constant blade angle and varying tip speeds. The fan test points and the identifying run numbers are shown on the map in figure 10. Table 1 lists the test conditions with ambient wind speed and direction which were tape recorded with the other data. An "I" or an "O" is used with the test point number to indicate whether the distortion post was "in" or "out".

Directivity data was recorded for five of the test conditions with the clean inlet.

SECTION 4
INLET FLOW DIAGNOSIS

It is now practical to measure unsteady surface pressures on high speed rotor blades using miniature pressure transducers and rotating electronic equipment. These pressures are of direct interest as a source of noise and blade vibration. However, blade pressure signals can also be used to study the structure of non-uniform flow entering the rotor as described in this section. The principal employed is that as a blade rotates and chops through a disturbance in the inflow, it responds with a pressure pulse whose timing and length can be related to the location and size of the disturbance. A new method of data reduction has been developed in which waveforms of the blade pressure signals are plotted in an especially revealing format and statistical calculations are perfomed which can be interpreted in terms of turbulence length scales.

Types of inflow distrubances include fixed flow distortion due, for example, to crosswinds and installation effects; atmospheric turbulence generated by the motion of air over the ground or over local obstacles; and turbulence generated inside the fan, for instance, in the inlet shroud boundary layer upstream of the rotor tips. A special series of tests was performed to study these effects during a static fan test.

Blade Pressure Waveform Plots
and their Interpretation

To introduce blade pressure waveform plots as inlet distortion space-time histories, the waveforms recorded with the intentional inlet disturbance shown in figure 9 are presented first. The instrumentated blade chops through the cylinder's wake once per revolution producing a once per revolution blade pressure pulse. Signal waveforms from the mid blade and tip pressure transducers are shown in the upper and lower plots, respectively, of figure 11. Each trace in these plots represents the pressure signal during one revolution, starting and ending (except for small overlaps) as the instrumented blade passes through the top of its rotation. Fifty-one traces from 51 consecutive revolutions are shown. On each channel the influence of the distortion cylinder mounted in the bottom of the inlet is clearly seen at the center of the plot, which represents the 180° or bottom location in the inlet. Thus, the waveform plotting technique accurately shows the location and size of the inlet disturbance in the circumferential sense.

In order to generate figure 11, analog tape data were digitized using a special clock with a frequency multiplier which generated exactly 150 equally spaced pulses per pulse of the once-per-revolution pipper. The 150 clock pulses caused the blade pressures to be digitized at 150 angles of rotation. Because the clock output is phase-locked to the input pipper, the samples are taken at the same location in the inlet during each

revolution. That is, sample number 75 is always taken as the blade passes through 180°.

This digitizing system allows the computer to perform statistical operations on the 150 data points as if they had been acquired by 150 hot wire anemometers fixed around the circumference. The samples in the tip transducer channel are labeled $p_{m,n}$ where the subscript m identifies the number of the revolution and n counts the sample (or angle) during that revolution starting with n = 1 at the top of the fan. The mid blade signals are $q_{m,n}$. The index m runs from 1 to M, the total number of revolutions analyzed, and n runs from 1 to N, the number of samples per revolution. Figure 11 was generated using M = 51 and N = 150.

For the first statistical analysis, the program computes the average, or signal enhanced, waveform according to

$$\bar{p}_n = \frac{1}{M} \sum_{m=1}^{M} p_{m,n} \tag{1}$$

which is plotted after the instantaneous waveforms in figure 11. The average pulse due to chopping a presumably symmetrical wake is seen to have a rapid rise and slower decay as predicted by unsteady airfoil theory. The last traces in figure 11 are the standard deviations of the signals computed in the streamwise direction,

$$\sigma_{pn} = \left[\frac{1}{M} \sum_{m=1}^{M} (p_{m,n} - \bar{p}_n)^2 \right]^{1/2} \tag{2}$$

which is an indication of the distribution of turbulence around the inlet circumference. In figure 11 the turbulence is largely in the wake of the distortion cylinder.

With the waveform plotting system thus explained, it is of interest to study similar plots made with a clean inlet as in figure 12. There, M = 706 revolutions, or about 15 seconds of fan operation, were analyzed with a higher gain on the pressure transducer signals so as to see effects of inlet disturbances occurring under moderate wind conditions (6-10 knots). At both transducer locations, several eddies are seen to pass through more or less axially, although they tend to drift circumferentially either in the direction of rotation or against it. Also, running the full length of the plot can be seen the effect of a signal cable stretched across the right side of the inlet. A cable connector was inadvertently placed in line with the mid-blade transducer.

The eddy seen at the beginning of figure 12 has a width of about 1/20 of a revolution (or 18°) and persists for 200 revolutions (or 4 seconds at 50 revolutions/ second). At

the axial flow velocity of 150 m/sec, this corresponds to an eddy effectively 600 meters long by about 15 cm wide. Thus, the waveform plot verifies the picture of inlet flow containing long, narrow "sausages" of turbulence.

At the beginning, middle, and end of figure 12 eddies are shown which appear simultaneously at both the tip and mid-blade transducer locations. Thus, persistent disturbances (which cause a tone-like noise component) do indeed appear in the shroud boundary layer as postulated by Cumpsty and Lowrie (ref. 4). However, in this example these are not boundary layer disturbances in the sense of a classical turbulent boundary layer with a laminar outer flow, but rather are disturbances impressed on the boundary layer by eddies ingested from the atmosphere. This cause-and-effect relationship will be reinforced in the ensuing discussion.

Waveforms from another flow condition are shown in figure 13. The most interesting feature of this plot is the eddy (or vortex) found between revolution numbers 340 and 500 which first appeared at the fan bottom and, in the course of 3 seconds, moved all the way around the inlet in the direction of rotation. This is shown in expanded view in figure 14 where it also can be seen that the pressure pulses measured by the two transducers have the opposite sign. Thus, the core of this disturbance must lie at a radius between the two transducers.

The next two figures represent one fan operating condition, but with different levels of wind coming from the right of the fan, as viewed from the front. The wind was 1-3 knots for figure 15 and 10-16 knots for figure 16. In the low wind case the circumferential eddy tracking is again apparent and the wake of the signal cable is prominent. In the high wind condition these features are masked and the inflow loses some of its orderly appearance as might be expected.

Figure 17 and its expanded view in figure 18 represent a case for low axial and low wind velocities. Again, a disturbance producing blade pressure pulses with opposite signs on the two transducers is shown.

Study of these waveform plots and others indicates that inlet disturbances tend to be randomly distributed around the circumference, particularly as measured at the mid-blade transducer location. However, at the tip location, it is frequently found that a higher level of activity exists near the bottom of the inlet suggesting influence from the ground or the test rig. In particular the forward flow over square support post shown in figure 5 causes a turbulent wake in this region.

Blade Pressure Statistics
and their Interpretation

In addition to the qualitative physical picture of the inlet flow developed above, quantative assessments of turbulence structure can be made from blade pressure sig-

nals by use of blade pressure statistics as described below. In the following discussion, turbulence correlation functions are computed as if the blade pressure signal measured at a point were a function only of the inlet turbulence velocity at that point. This simplification, although crude, is useful for the acoustician, structural dynamicist, and possible the aerodynamicist who are more directly interested in blade pressures resulting from inlet turbulence than they are in the turbulence itself.

RMS Pressure Levels – In the discussion of waveform plots so far, nothing has been said about pressure amplitudes. The system used was to compute rms signal levels

$$\sigma_p = \left[\frac{1}{MN} \sum_{m=1}^{M} \sum_{n=1}^{N} p_{m,n}^2 \right]^{1/2} \qquad (3)$$

and

$$\sigma_q = \left[\frac{1}{MN} \sum_{m=1}^{M} \sum_{n=1}^{N} q_{m,n}^2 \right]^{1/2} \qquad (4)$$

and then scale each plot so that the rms level was equivalent to 1/2 the distance between waveforms for successive revolutions. The rms levels for the clean inlet runs are given in table 2 where it can be seen that pressures measured at the tip are generally 1.7 to 2.2 times the mid-blade pressures. Because only about 5% of the blade span experiences this higher pressure level in the shroud boundary layer, a simple argument based on area weighting would indicate that the boundary layer is not an important cause of noise for the fan studied. However, since the inlet flow has a favorable pressure gradient all the way to the rotor face, this statement might not apply to high speed flight type or partial sonic inlets with diffusion upstream of the fan face. In future test programs more pressure measuring locations should be included to evaluate flow over the entire blade span.

Cause-and-Effect Relationships– In earlier investigations of sources of inlet turbulence and associated rotor noise (e.g. Cumpsty and Lowrie, Ref. 4; Hanson, reference 2), it was convenient to use two categories: turbulence ingested from outside (hereafter called atmospheric turbulence) and internally generated turbulence (internal shroud boundary layer). This breakdown permitted use of well known properties of boundary layers with turbulent inner flow and laminar outer flow. Using this approach, Cumpsty and Lowrie concluded that under some conditions the boundary layer turbulence could cause tone noise by interfering with the rotor. However, this conclusion appeared inconsistent with known properties of turbulent boundary layers and rotor acoustics. For example, Favre, et al (ref. 5) and Schubauer and Klebanoff (ref. 6) showed that the eddies in flat plate turbulent boundary layers with zero pressure gradient have a streamwise length about equal to 3/4 the boundary layer thickness (roughly 2 cm in

12

the present case) based on integral scale. But, it was shown in reference 2 that an eddy must be chopped 50 or more times to produce a tone like spectrum component. Since an eddy no longer than 2 cm could be chopped by one blade of the rotor, at most, tone noise could not result. Nevertheless, in the waveform plots presented above, disturbances appear in the boundary layer which persist for many rotor revolutions. In some cases it is clear that these are the same disturbances measured also at the mid-blade station (about 4 boundary layer thicknesses from the wall). In fact, both flow regimes have the same physical appearance in the waveform plots. A major point of this report, argued in the next paragraphs, is that the important, noise producing disturbances in the boundary layer are largely caused by atmospheric turbulence. In forward flight, where the effect of atmospheric turbulence should be greatly diminished, the disturbances in the boundary layer should also diminish.

From the similarity of the waveform plots measured in and outside of the boundary layer, it is clear that the two flow regimes are intimately related and that the appealing idea of separating the two flow regions is not consistent with the data. Because there is a plausible mechanism for turbulence with large axial length scales outside the boundary layer (the contraction effect discussed in Section 2 with reference to figure 4), it seems clear that the boundary layer is merely responding to these disturbances.

A good statistical measure of the extent of this cause-and-effect relationship is the crosscorrelation between the two blade pressure signals at zero time lag. This has been performed in two ways: first the total crosscorrelation is represented by the average value of the products $p_{m,n} q_{m,n}$ for many revolutions. When this is normalized to fall in the range ±1, the total crosscorrelation coefficient becomes

$$\rho_{pq} = \frac{1}{MN \, \sigma_p \, \sigma_q} \sum_{m=1}^{M} \sum_{n=1}^{N} p_{m,n} \, q_{m,n} \tag{5}$$

Computed values for ρ_{pq} are shown in table 2 to be between 0.4 and 0.7. Were the mid-blade transducer just at the edge of the boundary layer, the result would certainly have been higher.

Now ρ_{pq} contains effects of fixed as well as unsteady flow distortion. If a cross-relation coefficient more directly related to turbulence is desired, the steady distortion effect can be removed as in the product $(p_{m,n} - \bar{p}_n) (q_{m,n} - \bar{q}_n)$. When this is averaged over m and n and normalized, the following crosscovariance coefficient results

$$\rho'_{pq} = \frac{\dfrac{1}{M}\sum_{m=1}^{M}\sum_{n=1}^{N}(p_{m,n}-\bar{p}_n)(q_{m,n}-\bar{q}_n)}{\left(\sum_{n=1}^{N}\sigma_{pn}^2\right)^{1/2}\left(\sum_{n=1}^{N}\sigma_{pn}^2\right)^{1/2}} \tag{6}$$

The term covariance rather than correlation is used to indicate that the local mean value has been removed. Computed values of ρ'_{pq} which are also given in table 2 show values nearly as high as those for ρ_{pq}. Thus, in addition to the "eyeball" correlations possible with waveform plots, the formal statistical calculations show a strong relation between flow regions. This will be clearer on examination of other statistical correlations in the next section.

<u>Streamwise Correlation and Length Scale</u> – When a fixed hot wire anemometer is placed in an inlet to measure inlet turbulence velocity, the streamwise correlation function is determined by sampling the velocity signal at equal time intervals, $v_m = v(m\,\Delta t)$, and determining values of the products $v_m v_{m+k}$ averaged over m. A plot of this function versus time lag k was shown at the top in figure 2 for hot wire data from a previous program. The slow dropoff of the function shows that the flow remains coherent for about 1/2 second.

An analogous calculation can be made from a blade pressure signal by using the samples measured once per revolution at a given location (constant n) in the inlet. In this case the correlation products are $(p_{m,n}-\bar{p}_n)(p_{m+k,n}-\bar{p}_n)$ where the local mean value $\bar{p}_n$ has been subtracted to give the desired covariance function. Thus, the local streamwise covariance coefficient becomes

$$R_k^n = \frac{\sum_{m=1}^{M-k}(p_{m,n}-\bar{p}_n)(p_{m+k,n}-\bar{p}_n)}{\sum_{m=1}^{M-k}(p_{m,n}-\bar{p}_n)^2} \tag{7}$$

which is a function of the lag k (or increment in number of revolutions) and the location n, in the inlet.

Examples of these streamwise covariance coefficients are shown in figures 19 and 20 which were computed for the same fan operating condition but low and high wind levels, respectively. In most cases the covariance drops to negligible values for lags of 50 to 100 revolutions (one to two seconds of fan operation). The functions measured at the top, bottom, left, and right are different in detail but generally have the same features. Each plot shows two curves – one for each transducer. Covariance functions

in and outside the boundary layer are similar except that the outer flow sometimes exhibits greater length scales. Also, the length scales appear to be greater for the low wind condition. The low wind data has a kind of bimodal behavior: the covariance drops rapidly in the course of one revolution and then much more slowly after that. This suggests two basic length scales in the turbulence, one short which produces incoherent loading and broadband noise, and one long which produces paritally coherent loading and narrowband (or apparent tone) noise. This same feature was found in the hot wire data shown in figure 3. For the higher wind case, this effect is less pronounced.

Transverse Correlation and Length Scale – It is also possible to correlate across the waveform plots to study transverse correlation properties. In this case pressures measured at angle n are multiplied by pressures measured k samples away (or $\frac{k}{N}$ • 360 degrees of rotation away) as if $p_{m,n}$ and $p_{m,n+k}$ were measured at the same instant. When these products are averaged over many revolutions and properly normalized, the final result is

$$C_k^n = \frac{\frac{1}{M} \sum_{m=1}^{M} (p_{m,n} - \bar{p}_n) (p_{m,n+k} - \bar{p}_{m+k})}{\sigma_{pn} \ \sigma_{p(n+k)}} \tag{8}$$

which is a function of the separation in measureing points, k and the initial measuring point, n.

Examples of these local transverse covariance functions are given in figures 21 and 22 for the same operating conditions studied in the preceding two figures. Plots for origins at the top, right, bottom, and left of the inlet are given and as before show that turbulence properties are different at different locations in the inlet. Tip and mid-blade regions are substantially the same, although eddies appear somewhat narrower in the boundary layer. Comparing the figures for high and low wind shows transverse scales greater for the high wind. Thus, from this and the discussion of axial correlations, it is concluded that lower wind speeds result in longer, narrower eddies. This is consistent with the eddy stretching model previously put forward by the author (ref. 2). The large negative correlation shown in some cases indicates that for some separations, the signal at the origin has one sign while the signal k samples away tends to have the opposite sign. This suggests a vortex-like structure in the flow.

Signal Spectra and Coherence – Frequency spectra are examined here primarily to demonstrate the random nature of the blade loading in a quantitative way. This is accomplished by comparing the power spectral density (PSD) of the blade pressure signals with the spectrum of the signal enhanced waveforms $\bar{p}_n$ given in equation 1.

Consider the N pressures sampled from the m th revolution of the rotor: $p_{m,n}$ for n=1, $\cdots$,N. These represent a waveform which can be analyzed to find its Fourier coefficients A_{bm} and B_{bm} using well known formulas (e.g. Bendat and Piersol, ref. 8):

$$A_{bm} = \frac{2}{N} \sum_{n=1}^{N} p_{m,n} \cos \left(\frac{2\pi bn}{N} \right) \qquad b = 1, 2, \cdots, \frac{N}{2} - 1$$

$$A_{(N/2)m} = \frac{1}{N} \sum_{n=1}^{N} p_{m,n} \cos \pi n \qquad\qquad (9)$$

$$B_{bm} = \frac{2}{N} \sum_{n=1}^{N} p_{m,n} \sin \left(\frac{2\pi bn}{N} \right) \qquad b=1, 2, \cdots, \frac{N}{2} - 1$$

where b is the harmonic of the shaft rotation frequency. By using these coefficients, the original waveform can be reconstructed exactly from

$$p_{m,n} = \sum_{b=1}^{N/2} A_{bm} \cos \left(\frac{2\pi bn}{N} \right) + \sum_{b=1}^{\frac{N}{2}-1} B_{bm} \sin \left(\frac{2\pi bn}{N} \right) \qquad (10)$$

Thus, for the mth revolution, the b th harmonic is represented by a sine wave of amplitude $(A_{bm}^2 + B_{bm}^2)^{1/2}$ and phase arctan (B_{bm}/A_{bm}). The power in (or mean square value of) a sine wave of this amplitude is

$$S_{bm} = \frac{1}{2} (A_{bm}^2 + B_{bm}^2) \qquad\qquad (11)$$

and the power of the entire waveform from revolution number m is the sum of the S_{bm}'s from b = 1 to b = N/2. Thus the power has been broken down into N/2 frequency bands each centered on a harmonic of the rotor rotation frequency, and it follows that the function S_{bm} plotted versus b is a crude form of the PSD. A correctly averaged form of the PSD is given by

$$S_b = \frac{1}{M} \sum_{m=1}^{M} S_{bm} \qquad\qquad (12)$$

This average over many revolutions is known as "time slice averaging" in signal analysis.

16

It is straightforward to demonstrate that the S_b's do represent the entire power of the blade pressure signal by proving that

$$\overline{p^2} = \frac{1}{M}\sum_{m=1}^{M} \frac{1}{N}\sum_{n=1}^{N} p_{m,n}^2 = \sum_{b=1}^{N/2} S_b \tag{13}$$

Some examples of the PSD normalized to $\overline{p^2}$ are given by the top traces in each plot of figure 23, where tip and mid-blade spectra are compared for high and low wind conditions. Also shown by the lower traces in each plot are the harmonic coefficients H_b of the signal enhanced waveforms $\bar{p}_n$. These are computed from equation 9 with $p_{m,n}$ replaced by $\bar{p}_n$ to find the coefficients A_b and B_b and evaluating

$$H_b = \frac{1}{2}\left(A_b^2 + B_b^2\right) \tag{14}$$

(Only 50 harmonics are shown because higher frequencies were cut off with anti-aliasing filters). Since figure 23 is plotted in decibels, it is clear that only small portions of the signals are harmonic at frequencies of interest. The exceptions occur at multiples of harmonic number 7 which happens to be the number of vanes in the stator assembly. (The rotor "feels" the downstream stator's potential field). This will be demonstrated more clearly later with narrower band spectrum curves. Figure 23 also shows that the signal tends to be less coherent in the high wind condition.

Finally, it should be noted the computation of spectra via Equations 9, 11, and 12 would be prohibitive in computer time. Instead these formulas can be transformed in a manner similar to the Blackman-Tukey (ref. 9) spectrum calculation method. This is valuable because it requires computation of correlation functions which are of interest in their own right. First, the transverse correlation function is computed for each starting point n and these are averaged over n to give the average transverse correlation coefficient. This is Fourier transformed to find the PSD.

The average transverse correlation coefficients are shown in figure 24 for both transducers. Because it uses products of every pair of pressures from a given revolution, it is much better smoothed than the local covariance coefficients shown in figures 10 and 11. Note that in figure 24 the effect of the mean distortion has not been subtracted. Again, larger transverse length scales are apparent at the mid-blade position and for higher wind.

The Mechanism
For Higher Pressures at the Blade Tip

In the preceding discussion it has been demonstrated by several techniques that the flows in the tip and midblade regions are very similar and are highly correlated.

It has also been claimed that the disturbances in the outer flow (atmospheric turbulence) are the cause and that disturbances in the boundary layer are the effect. In the next paragraph a simple mechanism is offered to explain how this could be so despite the fact that the effect (tip rms pressures) is larger than the cause (mid blade rms pressures). The author is indebted to Dr. Werner Pfenninger of the Boeing Company for this explanation.

Consider a streamline just outside the boundary layer with energy $p_o + \frac{1}{2}\rho v_o^2$ which becomes disturbed with no loss in energy so that $\Delta p_o + \rho v_o \Delta v_o = 0$. Then consider another streamline inside the boundary layer with energy $p_i + \frac{1}{2}\rho v_i^2$ which responds so that $\Delta p_i + \rho v_i \Delta v_i = 0$. One of the foundations of boundary layer theory is the assumption that static pressures are transmitted undiminished across the boundary layer so that $\Delta p_i = \Delta p_o$. From this it follows that $v_i \Delta v_i = v_o \Delta v_o$ which can be rearranged to read $\Delta v_i / v_i = (v_o/v_i)^2 (\Delta v_o/v_o)$. Since the blade pressure responds to fluctuating angle of attack, which is essentially $\Delta v/v$, and since $v_o/v_i > 1$, this provides a plausible explanation for the larger signal levels measured at the blade tip.

SECTION 5
NOISE DIAGNOSIS

The noise generation process in a turbofan is highly complex, even for a single stage, subsonic machine such as the Q-Fan Demonstrator. There are many mechanisms which can produce noise spectra with broadband components and peaks at harmonics of blade passing frequency. In this section a new methodology is described and used for diagnosis of fan noise sources to determine which mechanisms are most important at various frequencies in the audio range. The analysis focuses on two dipole mechanisms: rotor radiation due to interaction with inlet turbulence (hereafter called rotor noise) and stator radiation due to interaction with viscous wakes from the rotor blades (hereafter called stator noise). Quadrupole mechanisms, which can be important at high tip speed and high blade loading (see Goldstein, ref. 10), are not treated in this report. However, because the test fan operates at relatively low tip speed and because the dipole analysis accounts for the observed noise, it appears that the quadrupole mechanisms are negligable here. Also, noise due to the steady blade load is negligible because of duct cutoff.

Both broadband and narrowband (the apparent tone) components are predicted using extensions of the unified source analysis techniques previously published by the author. In particular, the stator noise is calculated using a ten station strip analysis version of reference 1, as described by Magliozzi et al (ref. 11). Viscous wakes are calculated from cascade loss coefficients established via earlier performance measurements (Levintan, ref. 7). Initial wake formation is computed from the Silverstein formulas (ref. 12) and wake decay is computed assuming conservation of momentum using a technique adapted from Hill, Schaub, and Senoo (ref. 13). Rotor noise is predicted using an improved verision of the author's theory for rotor noise caused by atmospheric turbulence (ref.2) in which spanwise and chordwise blade pressure distributions are accounted for and the blade pressure statistics have been generalized. The development of this new rotor noise diagnostic tool is sketched in figure 25 where at the top it is shown that a blade loading model has been generated which fits blade pressure observations described in Section 4 of this report. The model is in terms of the statistics of blade pressure pulses caused by the rotor chopping eddies of inlet turbulence. This can be used to compute theoretical spectra of both blade pressure and sound pressure. Once the theoretical relations have been derived, they can be applied as in the lower half of figure 25. A measured blade pressure spectrum is used to determine the statistical parameters for that operating condition; then the same parameters are used with the blade loading model to predict the sound spectrum. The rotor sound power spectrum thus predicted and the stator spectrum predicted as above are compared with the measured power spectrum to diagnose fan noise.

In the remainder of this section, trends in the measurements of blade pressure and noise over the fan operating range are shown, the noise diagnosis methodology is

described, and finally, application of that methodology to sample fan data is presented.

Experimental Trends

A spectrum of blade pressure as measured by a current generation, 500 line, real time spectrum analyzer is shown at the top in figure 26. The spectrum has been averaged over 128 seconds of fan operation. Because the blade passes through the nearly fixed inlet distortion once per revolution, spectrum peaks appear at multiples of the shaft rotation frequency of 50 Hz. It is inevitable, however, that the fan rpm will drift slightly during the course of a long data run tending to smear the higher harmonics. For example, if the speed varied ±1%, then the 50th harmonic would be spread from 2475 Hz to 2525 Hz and the 51st harmonic would be spread from about 2525 Hz to 2575 Hz, etc. In this case the harmonics would appear to be absent above 2500 Hz. To correct for these rpm variations, an rpm tracking adapter was used with the spectrum analyzer to produce the results at the bottom in figure 26 where 100 harmonics can be found. The two portions of figure 26 represent analyses of the same section of tape recorded data. In one case the frequency axis is plotted in Hz; in the other case it is plotted in harmonics. For obvious reasons, analysis and plotting versus harmonic order were used to generate most of the spectra analyzed in this report.

As described in Section 3, the test fan was operated over a range including 7 combinations of tip speed and blade angle first with and then without a distortion cylinder mounted in the inlet as in figure 9. Simultaneous recordings were made of far field sound pressure on the fan axis and of surface pressure at two locations on a blade surface. Figures 27 through 33 show spectra measured for the 7 runs with the cylinder in place and figure 34 through 40 show spectra for the corresponding runs with a clean inlet. The on-axis noise spectra exhibit a peak at the meshing frequency of the main gearbox (116 teeth/revolution) as indicated for example in figure 33. Since this does not appear in the off-axis measurements, it does not contribute to sound power. Note the occasional emergence of the vane passing harmonics (multiples of 7) on the blade pressure spectra for the clean inlet as in figure 38. This effect, which was mentioned in Section 4, is caused by the rotor sensing the potential field of the stator.

The spectrum peaks at the 13 th harmonic (i.e. blade passing frequency) from both the sound spectra and the mid-blade pressure spectra are cross plotted versus tip speed in figures 41 and 42 for distorted and clean flow, respectively. The erratic trends in figure 41 are believed to be due to generating too large a wake with the inlet cylinder. This caused blade to plunge or oscillate at its natural frequency after hitting the wake as shown in figure 11. In the signal enhanced waveforms $\bar{p}_n$ and $\bar{q}_n$, two blade pressure peaks can be seen after the main peak.

With the clean inlet, the trends in figure 42 are more regular. Noise and blade pressure increase monotonically with tip speed for constant rotor blade angle. However,

along the constant pressure ratio operating line, the tendency is for both noise and blade pressure to drop with increasing tip speed. Since all of the points on the constant pressure ratio line were run in quick succession, this is believed to be a valid trend. Also, the reduced noise (on a PNdB basis) at higher tip speeds was noted in the original Q-Fan Demonstrator test series as reported by Metzger (ref. 14). This may be the effect anticipated by Goldstein and Atassi (ref. 15) whereby the potential field of a blade (associated with its loading) modifies the incoming distortion so as to reduce blade lift response. This should be examined further for potential as a noise reduction method.

Finally, far field noise spectral directivity was measured by indexing the microphone by 10° steps in an arc around the fan. Directivity patterns of the spectrum peaks and troughs (harmonics and 1/2 harmonics) were integrated to determine narrowband sound power as shown in table 3. These are used below in the noise diagnosis.

Description of Noise Diagnosis Methodology

The theory developed here for rotor noise diagnosis is an extension of the analytical techniques published previously by the author (refs. 2 and 16) and reference to that work is made occasionally below to shorten a rather lengthly derivation. Also, to preserve continuity of the text, some of the statistical details are relegated to appendices.

The central concept of the procedure for calculating the spectra of blade pressure and sound pressure due to interaction of the rotor with inlet turbulence is that the turbulence consists of discrete eddies. Thus, in principle, the flow could be observed for a long period of time and the eddies could be counted and categorized as to their length, width, point of entry on the rotor disc, and any other variables of interest. The observed values of these variables would be sets of random numbers whose statistical properties are given by their joint probability density function. In practice, it is not the eddies themselves which are observed but the blade pressure waveform which results from interference of the rotor blade with the eddies. The statistical property of the waveform measured is its spectrum rather than a probability density function. Nevertheless, the analytical model is in terms of a probability density function although this never needs to be measured directly. The statistics are in terms of time and space variables rather the more frequently used Fourier transform variables of frequency and wavenumbers.

Derivation of the spectrum equations requires the following steps. A form is chosen for the pressure pulse in the rotor disc due to a blade chopping an eddy one time. From this the associated far field pressure pulse is calculated. If the eddies are counted by the index v, the blades by u, and the successive chops (once per revolution) by m, then the Fourier transform of the acoustic pressure pulse can be designated P_{vum}.

It remains then to choose a joint probability density function for the statistical variables (i.e. formulate the statistical model) which has enough generality to fit a wide variety of flow conditions. Then the power spectral density of the sound pressure is computed from

$$G_s(\omega) = \lim_{V \to \infty} \frac{2\pi N}{2(V+1)T} \left| \sum_{-V}^{V} \sum_{u=1}^{B} \sum_{m} P_{vum} \right|^2 \tag{15}$$

where N/T is the average number of eddies per revolution entering the rotor. Since $(2V+1)T/N$ is the time for entry of $2V+1$ eddies, equation 15 is read "the power spectral density equals the limit as time goes to infinity of the expected value (ensemble average) of the energy spectral density per unit time". Finally, it must be noted that for signals with extremely narrowband components such as fan noise, it is not practical to measure the power spectral density without bias because the PSD peaks and the filters have about the same bandwidth. The best solution for comparing experimental and theoretical spectra is to analyze the theoretical PSD with a set of mathematical filters whose characteristics match the electronic spectrum analyzer used with the test data. Then in the diagnosis process, filtered spectra are compared rather than PSD's.

Blade Loading Model – The blade loading model consists of a form for an arbitrary blade pressure pulse plus the statistics relating all the pulses. The model was formulated specifically to relate to blade pressure as measured by a surface pressure transducer.

Arbitrary Blade Pressure Pulse: Consider the coordinate system and rotor geometry given in figures 43 and 44. The dipole strength is $\vec{f}(\vec{r}_o, t_o)$, the force per unit volume on the fluid as described in the source coordinates r_o, θ_o, ϕ_o, and t_o. The Fourier transform of the acoustic pressure pulse at the field point (r, θ, ϕ) due to the source pulse $\vec{f}(\vec{r}_o, t_o)$ was shown by the author in reference 16 (and by Ffowcs-Williams and Hawkings (ref. 17) in a different notation) to be

$$P(\vec{r}, \omega) = \frac{-ike^{ikr}}{8\pi^2 r^2} \iiiint \vec{r} \cdot \vec{f}(r_o, t_o) e^{i\omega t_o}$$

$$\cdot e^{-ikr_o} \left[\cos\theta \cos\theta_o + \sin\theta \sin\theta_o \cos(\phi - \phi_o) \right] d\vec{r}_o \, dt_o \tag{16}$$

in the geometric and acoustic far field if the effects of solid boundaries and fluid motion are ignored.

The general form for the dipole pulse distribution is taken to be

$$f(\vec{r}_o, t_o) = f_r(r_o) \ \delta(\theta_o - \frac{\pi}{2}) \ f_\phi(\phi_o - \phi_u - \Omega t_o) \ p(t_o) \tag{17}$$

as sketched in figure 45; the direction of the resultant force is assumed to be normal to the blade whose stagger angle is β. The location of the blade trailing edge at $t_a = 0$ is ϕ_u. The above form for the blade loading pulse is interpreted as follows. By use of the delta function $\delta(\Theta_o - \frac{\pi}{2})$, it is assumed that the source lies in the $x_1 = 0$ plane or that the wavelength of interest is larger than the projected blade thickness. Thus, the blade pressure distribution is $f_r(r_o) \ f_\phi(\phi_o - \phi_u - \Omega t_o) \ p(t_o)$. The spanwise distribution of pressure on a radial line passing through the pressure transducers is $f_r(r_o) \ p(t_o)$. The chordwise pressure distribution is $f_\phi(\phi_o - \phi_u - \Omega t_o)$ which can be expanded as a complex Fourier series:

$$f_\phi(\phi_o - \phi_u - \Omega t_o) \ p(t_o) = p(t_o) \frac{C_e}{2\pi r_o} \sum_{m=-\infty}^{\infty} \nu_m \ e^{-im(\phi_o - \phi_u - \Omega t_o)} \ . \tag{18}$$

The constants in this series were chosen so that, when the lift/unit span is obtained by integrating pressure over the chord according to $\int f_r(r_o) \ f_\phi(\phi_o - \phi_u - \Omega t_o) \ r_o \ d\phi_o$, the result evaluated at the transducer location $r_o = R_x$, is $\nu_0 C_e f_r(R_x) p(t_o)$ where $f_r(R_x) p(t_o)$ is the actual measured pressure. It is convenient to set $\nu_0 = 1$ so that the coefficients ν_m govern only the shape of the pressure distribution. The amplitude effect is handled by C_e, the effective chord which, when multiplied by the measured pressure, gives the true section lift.

The effective chord C_e could be calculated if the chordwise pressure distribution were known accurately. For example, if the airfoil is assumed to be thin and uncambered and if the flow is assumed to be at low Mach number and low frequency, the unsteady pressure distribution has been shown by several authors to have the same shape as the steady pressure distribution. However, in any propulsive fan all these assumptions would be violated and there is no existing theory which could give C_e accurately. Thus in practice C_e is best determined by relating a measured, intentionally caused blade pressure to the resulting sound pressure. This is done at each fan operating condition of interest so that, in effect, C_e becomes a calibration constant which accounts for chordwise location of the pressure transducer, Mach number and cascade effects, and whether the transducer is a differential or single surface type. The effective chord analysis is given in Appendix A and the values of C_e for each flow condition are given in table 4.

It should be pointed out that the form chosen for the chordwise pressure distribution $f_\phi(\phi_o - \phi_u - \Omega t_o)$ implies that there are no traveling waves over the chord. That is, an incoming velocity disturbance produces an airfoil pressure response simultaneously over the entire chord as in the Sears unsteady airfoil theory (ref. 18). This approximation is not good at high Mach number and high frequency but is used here for expediency.

In order to apply techniques from random pulse modulation theory, the pressure pulse of interest (call it now $p_{vum}(t_o)$ rather than $p(t_o)$) is expressed in terms of a standard pulse shape $p_s(t)$ as shown at the bottom in figure 45. Thus,

$$p_{vum}(t_o) = A_{vum}\, p_s\left(\frac{t_o - t_{vum}}{w_{vum}}\right). \tag{19}$$

This allows the pulse height A_{vum}, width w_{vum}, and time of occurence t_{vum} to be random variables governed by the eddy statistics mentioned above.

When equations 17, 18, and 19 are substituted into equation 16, the integrals can be performed analytically, yielding

$$P_{vum}(r,\omega) = \frac{ike^{ikr}}{4\pi r} C_e A_{vum} w_v \sum_{n=-\infty}^{\infty} F\left[w_v(\omega+n\Omega)\right] e^{i(\omega+n\Omega)t_{vum}}$$

$$\cdot e^{in(\phi_u - \phi - \frac{\pi}{2})} \int_{R_H}^{R_T} \nu_n(r_o) f_r(r_o)\left(\sin\beta\,\cos\theta + \frac{n\cos\beta}{kr_o}\right)\, J_n(kr_o\sin\theta)\, dr_o \tag{20}$$

for the acoustic pressure pulse due to the blade pressure pulse $f_r(r_o)\, f_\phi(\phi_o - \phi_u - \Omega t_o)$ $p_{vum}(t_o)$. $F(\omega)$ is the Fourier transform of $p_s(t_o)$ and R_H and R_T are the hub and tip radii of the rotor. Note also that the last two subscripts have been dropped from w_{vum} leaving w_v as the common width of all pulses due to eddy #v.

Up to this point in derivation, no approximations have been made beyond using the open space Green's function and assuming the source is thin in the axial dimension. However, because of the blade ends, no function $f_r(r_o)$ could be found which permitted equation 20 to be integrated exactly. Nevertheless, a very satisfactory result is obtained by expressing $f_r(r_o)$ as

$$f_r(r_o) = \left[1 + \left(\frac{r_o - R_V}{2\pi R_e \mu w_V}\right)^2\right]^{-1} \tag{21}$$

which has the form shown in figure 45. R_V is the eddy entry radius, R_e is an effective radius introduced here for dimensional purposes, and μ is kind of an eddy aspect ratio (i.e. ratio of dimensions in r_o and ϕ_o directions). If $f_r(r_o)$ is rewritten as

$$f_r(r_o) = 2\pi^2 R_e \mu w_V f'_r(r_o) \tag{22}$$

where

$$f'_r(r_o) = (2\pi^2 R_e \mu w_V)^{-1} \left[1 + \left(\frac{r_o - R_V}{2\pi R_e \mu w_V}\right)^2\right]^{-1} \tag{23}$$

then $f'_r(r_o)$ behaves like a Dirac delta function for small values of w_V. Now w_V is proportional to the tangential size of the eddy and typically it is expected that μ will be less than 1. But the important noise generating eddies for a subsonic rotor have a tangential size of the order of a blade gap and smaller. Thus, it appears to be acceptable to replace $f_r(r_o)$ with $2\pi^2 R_e \mu w_V \delta(r_o - R_V)$ for the acoustic calculations. The distribution of the eddy over the span has two effects on the acoustic radiation: a wide eddy causes a large integrated lift. This effect is accounted for correctly through the proportionality factor μw_V. However, the spanwise distribution also causes a mutual interference effect like a line source. This is suppressed by the δ function approximation.

The delta function form for $f_r(r_o)$ allows integration of equation 20, yielding finally

$$P_{vum}(\vec{r}, \omega) = \frac{ike^{ikr}}{2r} \pi C_e R_e \mu A_{vum} w_V^2 \sum_{n=1}^{\infty} \nu_n \nu_{-n} \; F\left[w_V(\omega + n\Omega)\right] \tag{24}$$

$$\cdot J_n(kR_V \sin\theta)(\sin\beta\cos\theta + \frac{n\cos\beta}{kR_V}) \; e^{in(\phi_u - \phi - \frac{\pi}{2})} e^{i(\omega + n\Omega)t_{vum}} \; .$$

Blade Pressure Statistics: The sound spectrum is to be computed from equation 15 with P_{vum} given by equation 24. However, the blade pressure statistics for the random variables A_{vum}, w_V, R_V, and t_{vum} must be specified before the ensemble average can be computed. The statistics have the same form as in references 2 and 16 except that the new variable R_V, the eddy entry radius, has been added and the joint

statistics of the eddy amplitude a_V, width w_V, and length λ_V have been greatly gener-alized to permit greater flexibility in matching experimental blade pressure spectra.

The pulse amplitudes A_{vum} are governed by the envelope function shown in figure 46,

$$A_{vum} = a_v (1+C_{vum}) \; g \left(\frac{mUT+uUT/B-y_v}{\lambda_v} \right) \tag{25}$$

which allows the once–per–revolution pulses due to a given eddy to grow and then decay as the eddy passes through the disc. Random amplitude jitter above and below the smooth envelope is permitted by the pulse amplitude modulation (PAM) variable C_{vum} which has standard deviation σ_a and zero mean. The random length of the eddy is given by λ_V which essentially controls the number of pulses caused by the eddy. The vari-able y_V is uniformly distributed on the interval 0 to UT to allow some of the short eddies to pass between blades without being touched.

The envelope function in equation 25 is expressed in terms of a standard envelope,

$$g(y) = \frac{1}{1 + (y/UT)^2} \tag{26}$$

which is convenient for computational purposes. The form of the last two equations is such that the convection velocity U cancels out of the calculation.

The pulse timing is given by

$$t_{vum} = t_v + (u/B+m+b_{vum})T \tag{27}$$

where t_V is the random arrival time of the eddy and b_{vum} is the random time jitter about a perfect once–per–revolution pulse rate. b_{vum} is the pulse position modulation (PPM) variable and is taken to be Gaussian with standard deviation σ and zero mean.

Averaging over the eddy entry radius R_V, which is uniformly distributed over the blade span (R_H to R_T), results in an effective radius which is taken to be the same R_e introduced above.

The statistics of the eddy amplitude a_V, width w_V, and length λ_V are described in Appendix B. An interesting consequence of the statistical model is that the Lowson – Scheiman "loading law" is predicted from theory for very general conditions. This empirical law which gives the nth harmonic blade load in terms of the Nth harmonic as

$$L_n = L_N(n-N)^{-k} \qquad (28)$$

is used commonly to predict harmonic rotor noise for propellers, helicopter rotors, and fan rotors. However, it is shown in Appendix C to follow from the statistical inlet turbulence model.

Power Spectral Density Equations – The limit, sums, and averages up to the point of averaging over a_v, w_v, and λ_v are the same as in references 2 and 16 so that intermediate power spectrum results can be written down directly. Results are given below for the PSD of sound pressure, sound power, and blade pressure in terms of the effective radius Mach number $M = \Omega R_e/c$. Frequency is expressed as a generalized harmonic order of blade passing frequency, $y = \omega/B\Omega$, for the sound results and as a harmonic of rotation frequency, $x = \omega/\Omega$, for the blade pressure results.

Spectrum of Sound Pressure: The power spectral density of the far field sound pressure is

$$G_s(B\Omega y) = \frac{2\pi N}{T} \left(\frac{\pi \mu C_e M}{r}\right)^2 \sum_{n=-\infty}^{\infty} \nu_n \nu_{-n} Z_n \left\{ e^{-(By+n)^2 (2\pi\sigma)^2} Q_n(B,y) \right.$$

$$\left. + \left[\sigma_a^2 + 1 - e^{-(By+n)^2 (2\pi\sigma)^2}\right] S_n(B,y) \right\} \qquad (29)$$

where

$$Z_n = \frac{1}{4}\left(yB\sin\beta \, \cos\theta + \frac{n\cos\beta}{M}\right)^2 J_n^2 \, (yBM\sin\theta) \qquad (30)$$

$$Q_n(B,y) = \overline{a_v^2 \, w_v^4 \, \left|F[w_v\,\Omega\,(By+n)]\right|^2} \, (2\pi B\lambda_v) \, H(2\pi B\lambda_v, y)$$

and

$$S_n(B,y) = \overline{a_v^2 \, w_v^4 \, \left|F[w_v\,\Omega\,(By+n)]\right|^2} \, (2\pi B\lambda_v) \qquad (31)$$

The standard pulse used here has the same form as in reference 2 with the dimensions of pressure rather than force:

$$P_s(t) = \frac{p_o}{1+(t/T)^2} \qquad (32)$$

where p_o is the usual acoustic pressure reference of $20\,\mu$Pa. It is assumed that the chordwise pressure distribution is triangular with its peak at the airfoil leading edge. This leads to

$$\nu_o{}^2 = 1$$

$$\nu_n \nu_{-n} = 4\left(\frac{R_e}{nC_B}\right)^4 \left[2+\left(\frac{nC_B}{R_e}\right)^2 - 2\cos\left(\frac{nC_B}{R_e}\right) - \frac{2nC_B}{R_e}\sin\left(\frac{nC_B}{R_e}\right)\right] \ , \ n \neq 0. \tag{33}$$

Finally, $H(2\pi B\lambda_v, y)$ is the spectrum peak function defined in reference 2 by

$$H(2\pi B\lambda_v, y) = \frac{N_p}{\sinh N_p} \sum_{m=0}^{\infty} \cosh\left\{N_p\left[2y-(2m+1)\right]\right\} \tag{34}$$

and shown in figure 47 where $N_p = 2\pi B\lambda_v$ is essentially the number of pulses caused by the eddy with length parameter λ_v. (For each term in the sum, $m < y \leq m + 1$).

Spectrum of Sound Power: The spectral density $G_W(\omega)$ of sound power is obtained by integrating the intensity spectrum $\frac{1}{\rho c} G_S(\omega)$ over the spatial angles according to

$$G_w(\omega) = \frac{1}{\rho c} \int_{-\pi}^{\pi}\int_0^{\pi} G_s(\omega)\, r^2\sin\theta\ d\theta\ d\phi \tag{35}$$

or

$$G_w(B\Omega y) = \frac{2\pi N}{\rho cT}(\pi\mu C_e M)^2 \sum_{n=-\infty}^{\infty} \nu_n \nu_{-n} \alpha_n \left\{ e^{-(By+n)^2(2\pi\sigma)^2} Q_n(B,y) \right.$$

$$\left. + \left[\sigma_a{}^2+1-e^{-(By+n)^2(2\pi\sigma)^2}\right]S_n(B,y)\right\} \tag{36}$$

where

$$\alpha_n = \int_{-\pi}^{\pi}\int_0^{\pi} Z_n \sin\theta\ d\theta\ d\phi \tag{37}$$

28

Evaluation of α_n requires the Bessel function integrals,

$$\int_0^{\pi/2} J_n^2 (z\sin\theta) \sin\theta \, d\theta = \frac{1}{z} \sum_{k=0}^{\infty} J_{2n+2k+1}(2z) \tag{38}$$

and

$$\int_0^{\pi/2} J_n^2 (z\sin\theta) \cos^2\theta \, \sin\theta \, d\theta = \frac{2}{z^2} \sum_{k=0}^{\infty} \frac{(k+1)\,(2n+k+1)\,(n+k+1)}{(2n+2k+3)\,(2n+2k+1)} \, J_{2n+2k+2}(2z) \tag{39}$$

These requirements appeared previously in the work of Embleton and Theissen (ref. 19) and Lowson (ref. 20) who were aware of equation 38 but not equation 39. Lowson converted equation 39 to a numerical series which converged only for a limited range of z. However, Bailey (ref. 21) worked out an integral of which equations 38 and 39 are both special cases. This discovery means that sound power spectrum calculations can be made for nearly the same computer time as sound pressure calculations whereas, previously, the direct numerical integrations or series were prohibitively expensive or non-convergent.

Spectrum of Blade Pressure: According to the blade loading model, the pressure pulses measured by a transducer located at R_x are $f_r(R_x) \, p_{vum} (t_o)$ which have Fourier transforms

$$P_{vum}^x (R_x, \omega) = \frac{A_{vum} \, w_v \, e^{i\omega t_{vum}} \, F(w_v \omega)}{1 + \left(\dfrac{R_x - R_v}{2\pi R_e \mu w_v} \right)^2} \tag{40}$$

The averaging in the equation for the blade pressure spectrum,

$$G_x(\omega) = \lim_{V \to \infty} \frac{2\pi N}{(2V+1)T} \overline{\left| \sum_{v=-V}^{V} \sum_{m} P_{vum}^x (R_x, \omega) \right|^2} \tag{41}$$

requires averaging $\left[1 + \left(\dfrac{R_x - R_v}{2\pi R_e \mu w_v} \right)^2 \right]^{-1}$ over the eddy entrance radius R_v to

29

account for the fact that, in general, eddies don't arrive at a radius centered on the transducer. If it is assumed that eddies are equally likely anywhere on the blade span and that R_x is independent of the other random variables, then the required probability integral is

$$I_p = \frac{1}{R_T - R_H} \int_{R_H}^{R_T} \frac{dR_v}{\left[1 + \left(\dfrac{R_x - R_v}{2\pi R_e \mu w_v}\right)^2\right]^2} \tag{42}$$

To produce tractable analytical results, the transducer is taken to be near the tip $(R_x \approx R_T)$ and μw_v is assumed to be small as before. A simple change of variable yields:

$$I_p \approx \frac{2\pi R_e \mu w_v}{R_T - R_H} \int_0^{\frac{R_T - R_H}{2\pi R_e \mu w_v}} \frac{dx}{(1+x^2)^2} \tag{43}$$

Now for eddy widths (pulse 1/2 amplitude points) equal to a blade gap, it can be shown that $w_v = \frac{1}{2B}$. For the Q-Fan Demonstrator $B = 13$ and $R_H = \frac{1}{2}R_T$ and taking $\mu = \frac{1}{2}$ and $R_e = 0.8\ R_T$ the upper limit on the integral for I_p becomes 5.1. Since the intergrand is 0.0013 for $x = 5.1$ versus 1 for $x = 0$, an excellent approximation to I_p is found by setting the upper limit equal to ∞ giving

$$I_p \approx \frac{\pi^2 R_e \mu w_v}{2(R_T - R_H)}. \tag{44}$$

With this result, the blade pressure spectrum becomes

$$G_x(x\Omega) = \frac{2\pi N}{T}\ \frac{\pi^2 R_e \mu}{2(R_T - R_H)}\left\{ e^{-(2\pi x\sigma)^2} Q_o^x(x) + \left[\sigma_a^2 + 1 - e^{-(2\pi x\sigma)^2}\right] S_o^x(x) \right\} \tag{45}$$

30

where

$$\overline{Q_o{}^x(x) = a_v^2 w_v^3 \left| F(w_v \Omega x) \right|^2 (2\pi\lambda_v) \, H(2\pi\lambda_v, x)}$$

and

(46)

$$\overline{S_o{}^x(x) = a_v^2 w_v^3 \left| F(w_v \Omega x) \right|^2 (2\pi\lambda_v)} \qquad .$$

Equations for Filtered Spectra – When an extremely narrowband signal such as fan noise is analyzed with a spectrum analyzer, the result is strongly biased due to the finite bandwidth of the filter. Thus, the effect of the filter characteristics must be included in the theoretical analysis. Figure 48 shows the filter shape of the 500 line, time compression analyzer used for data analysis plus the theoretical filter fit to this shape by the equation

$$G_{\beta 0}(f) = \begin{cases} \cos\left(\dfrac{1.52\,f}{\beta}\right) & |f| < 0.7\beta \\[3mm] 2.51 \, \exp\left(-\dfrac{2.302\,|f|}{\beta}\right) & |f| \geq 0.7\beta \end{cases}$$

(47)

for a set of filters with frequency spacing β. The filters at frequencies $m\beta$ are given by $G_{\beta 0}(f)$ shifted as follows.

$$G_{\beta m}(f) = G_{\beta 0}(f - m\beta)$$

(48)

where $m = 1, 2, \cdots, 500$. The noise bandwidth of the filter is $\displaystyle\int_{-\infty}^{\infty} G_{\beta m}(f) \, df = 1.58$.

The success of the theoretical filters is shown in figure 49 where, on the left side, the same theoretical PSD is analyzed with filter sets of 3 different bandwidths and on the right a signal is shown analyzed with the corresponding electronic filters. The main differences between the theoretical and experimental results is that the original PSD's were not the same; the effect of the filters appears to be adequately reproduced.

Spectra for blade pressure, sound pressure, and sound power are calculated according to the following definitions. The filtered spectrum levels for the blade pressure are

$$L_{xm} = 10 \log_{10} \left[\frac{2 \displaystyle\int_o^{\infty} G_x(2\pi f) \, G_{\beta m}(f) \, df}{p_o^2} \right]$$

(49)

31

where $p_o = 20$ μ Pa (0.0002 dynes/cm^2). Similarly for the sound pressure

$$L_{sm} = 10 \log_{10} \left[\frac{2 \int_o^\infty G_s(2\pi f) \, G_{\beta m}(f) \, df}{p_o^2} \right] \tag{50}$$

and for the sound power,

$$L_{wm} = 10 \log_{10} \left[\frac{2 \int_o^\infty G_W(2\pi f) \, G_{\beta m}(f) \, df}{W_o} \right] \tag{51}$$

where $W_o = 10^{-13}$ watts. The factors of 2 appear because the PSD's are two sided. Plots of these levels for m running from 1 to 500 are the theoretical filtered spectra.

The above frequency integrals can be performed analytically with good accuracy if it is recognized that the terms in the PSD formulas vary slowly with frequency except for the function $H(2\pi B \lambda_v, \frac{\omega}{B\Omega})$. Thus, the results will be in terms of the integrals

$$L_m = \frac{1}{2\pi B \lambda_v} \int_{-\infty}^\infty H(2\pi B \lambda_v, \frac{\omega}{B\Omega}) \, G_{\beta m}(f) \, df \tag{52}$$

where it is implicit that $B = 1$ in the blade pressure spectrum calculations.

Now the spectrum equations can be written as follows. The blade pressure spectrum becomes

$$L_{xm} = 10 \log_{10} \left(\frac{2\pi^3 N \mu R_e \beta_x T}{R_T - R_H} \right) \left\{ \underbrace{Q_{xm} e^{-(2\pi x \sigma)^2}}_{\text{peaked component}} + S_{xm} \left[\underbrace{\sigma_a}_{\text{PAM}} + \underbrace{1 - e^{-(2\pi x \dot\sigma)^2}}_{\text{PPM}} \right] \right\} \tag{53}$$

where β_x is the frequency spacing of the filters and

$$Q_{xm} = a_v^2 w_v^3 (2\pi \lambda_v)^2 \left| F(w_v \Omega x) \right|^2 L_m \Big/ T^2 p_o^2$$

$$S_{xm} = 1.58 \, a_v^2 w_v^3 (2\pi \lambda_v) \left| F(w_v \Omega x) \right|^2 \Big/ T^2 p_o^2 . \tag{54}$$

32

The sound pressure spectrum becomes

$$L_{sm} = 10 \log_{10} \frac{\pi^3 N \mu^2 C_e^2 \beta_s T}{r^2} \sum_{n=-\infty}^{\infty} \nu_n \nu_{-n} Z_n \left\{ e^{-(By+n)^2 (2\pi\sigma)^2} Q_{smn} \right. \quad (55)$$

$$\left. + \left[\sigma_a^2 + 1 - e^{-(By+n)^2 (2\pi\sigma)^2} \right] S_{smn} \right\}$$

where β_s is the frequency spacing of the filters and

$$Q_{smn} = \overline{a_v^2 \ w_v^4 \ (2\pi B \lambda_v)^2 \ \left| F \left[w_v \Omega (By_m + n) \right] \right|^2 \ L_m} \Big/ T^2 \ p_o^2 \quad (56)$$

$$S_{smn} = 1.58 \ \overline{a_v^2 \ w_v^4 \ (2\pi B \lambda_v) \ \left| F \left[w_v \Omega (Bym+n) \right] \right|^2} \Big/ T^2 \ p_o^2$$

And the sound power spectrum becomes

$$L_{wn} = 10 \log_{10} \left(\frac{\pi^3 N p_o^2 C_e^2 \mu^2}{W_o \rho_c} \right) \left(\beta_s T \right) \sum_{n=-\infty}^{\infty} \nu_n \nu_{-n} \alpha_n \left\{ e^{-(By+n)^2 (2\pi\sigma)^2} Q_{smn} \right. \quad (57)$$

$$\left. + \left[\sigma_a^2 + 1 - e^{-(By+n)^2 (2\pi\sigma)^2} \right] S_{smn} \right\} \quad .$$

The working forms of the probability integrals Q_{xm}, S_{xm}, Q_{smn}, and S_{smn} are given in Appendix B.

Application of Noise Diagnosis Methodology

The statistical blade loading model presented above was based on some rather intuitive ideas which are best justified by demonstrating a good fit of theoretical spectra to measured spectra. This is done below in detail for five flow conditions. Signals from the mid-blade pressure transducer are used for the calculations of this section because they appear to more representative of the majority of the noise producing portion of the inlet flow as shown in Section 4.

33

Figure 50 shows the mid-blade pressure spectrum for test condition 0-3B at the top. The fit of the theory by adjusting blade pressure statistics is at the bottom. (The exact statistical parameters used are given in Appendix B and table 5). Three spectrum components corresponding to the peak, PAM, and PPM terms identified in equation 53 are shown in addition to the sum. The fit of the peaks and valleys of the spectra are made to match very well as shown by the dashed envelope lines in the top half of the figure and fine structure of the spectra are well matched.

Figure 51 shows test sound pressure spectra measured for condition 0-3B at microphone locations 60° and 120°. These, compared with rotor noise spectra predicted from the same statistical parameters which yielded figure 50, are convincing evidence that most of the Q-Fan static noise is due to inlet turbulence.

Rotor noise directivity predictions are compared with test for the same flow condition in figure 52 for both broadband and the peak at blade passing frequency. The comparison is reasonably good considering the simplicity of the acoustic formulation. In particular, the fore-and-aft power split seems well predicted.

Finally, in figure 53 predictions of rotor and stator noise contributions are compared with measurements on the basis of narrowband sound power spectra. At frequencies up to the third harmonic of blade passing frequency, rotor and stator sources are about equally important while at higher frequencies the stator noise drops rapidly and the rotor clearly dominates the broadband and harmonic peak levels.

The above observations have been checked at four other fan operating conditions. Figure 54 shows the results of matching theoretical blade pressure spectra to measurements (with statistical parameters listed in Appendix B and table 5). The corresponding sound power comparisons are shown in figures 55 and 56 where the previous conclusions on relative importance of rotor and stator sources are reinforced over a substantial range of tip speeds and pressure ratios.

SECTION 6
PARAMETRIC STUDIES

Two analytical studies of the effect on rotor noise of changing various design and operating parameters were performed: an Acoustic Parametric Study and an Aero-acoustic Parametric Study. The Acoustic Parametric Study was done first to explore the rotor/inlet turbulence interaction noise radiation theory which had been published previously by the author (ref. 2). This was a point source analysis giving noise spectra in terms of specified blade lift statistics (as opposed to the measured blade pressure statistics used in the current version of the analysis). In this study the parameters in the radiation formulas such as number of blades, rotational Mach number, turbulence scales, etc. were varied one at a time to study purely acoustic effects without regard for whether those changes were reasonable aerodynamically.

The Aeroacoustic Parametric Study was performed with the more advanced version of the theory described in Section 5. In this study using a baseline case measured on the Q-Fan Demonstrator, the influences on the rotor noise of changing design tip speed and changing number of rotor blades were calculated. The parameters were varied in such a way as to keep the rotor operating with the same aerodynamic performance.

Acoustic Parametric Study

The measure of sound pressure spectrum level used was the PSD normalized as in reference 2:

$$H_s(y) = \frac{T}{N} \quad \frac{1}{\overline{a^2 w \lambda}} \quad \left(\frac{cr}{F_o} \right)^2 \quad G_s(B \Omega y) \tag{58}$$

This amounts to dividing G_s by the mean square value of the lift pulses on one blade, neglecting modulation effects. $G_s(B\Omega y)$ was as given by equations 29, 30 and 31 except that $(\pi \mu C_e M/r)^2$ was replaced by $(1/crT)^2$, w_v^4 was replaced by w_v^2 and $\nu_n \nu_{-n}$ was unity for all n because of the assumption of point chordwise loading. The joint probability density function used to evaluate $Q_n(B\Omega y)$, $S_n(B\Omega y)$ and $\overline{a^2 w \lambda}$ was

$$f(a, w, \lambda) = \frac{w \lambda e^{-a^2/2A^2} e^{-w/W} e^{-\lambda/L}}{A W^2 L^2 \sqrt{2\pi}} \tag{59}$$

where $A = A_1 w/W$ and $W = W_1 \lambda/L$. These statistics are explained in detail in reference 2 and will be found to be a special case of the $f(a, w, \lambda)$ given in Appendix B.

Sound power spectra were also normalized as in equation 58, yielding

$$H_w(y) = \int_{-\pi}^{\pi} \int_0^{\pi} H_s(y) \sin \theta \, d\theta \, d\phi \qquad (60)$$

where the integral was done analytically via equations 38 and 39.

The base case for the study represented the Q-Fan Demonstrator running statically and was the same as in reference 2 except that for convenience the effective radius Mach number was 0.5 rather than 0.58, the number of blades was 12 rather than 13 and the blade stagger was changed from 40° to 45°. The modulation parameters were $\sigma_a = 0.2$ and $\sigma = 0.015$. W_1 was 0.0025 implying $\overline{w} = 0.01$ or an average pulse width between 1/2 amplitude points of 7° of rotor rotation. $\overline{\lambda}$ was 3 meaning that the average number of chops between 1/2 amplitude points on an eddy envelope function was 6 per blade. The sound power PSD for this baseline condition is shown in figure 57 where the three spectrum components are shown in addition to the total spectrum.

The first effect studied was that of varying the level of pulse amplitude modulation (PAM) as shown in figures 58 and 59. The PAM broadband component power varies as σ_a^2 but this effect does not appear until the PPM broadband component is overcome. Directivity is unaffected by the level of PAM.

The effect of pulse position modulation (PPM) was studied in similar fashion with the results shown in figures 60 and 61. Increased PPM is seen to modify the spectrum shape drastically by reducing energy in the harmonic peaks in exchange for broadband energy. The upper harmonics are affected first. Directivity is affected in a complex way because the PPM variable σ changes modal amplitudes as shown in equation 29.

The turbulence transverse length scale has a strong effect on the noise spectrum as shown in figure 62. Very narrow eddies lead to a spectrum with a relatively high level of high frequency content as shown at the top. Wide eddies lead to a spectrum which rolls off much faster and generally has a lower level because broad blade pressure pulses are acoustically less efficient than narrow pulses. Turbulence transverse scale also affects directivity as shown in figure 63. Apparently, blade pressure pulses occurring over a larger portion of a blade revolution have more of an opportunity for self interference. The wide eddy directivities ($\overline{w} = 0.1$) are similar to steady loading directivity patterns for propellers.

The streamwise length scale of the turbulence affects the coherence of sound as shown by the spectra in figure 64. As length scale increases, the broadband com-

ponent remains unchanged but the harmonic peaks emerge more strongly. Beyond a certain point, this increase in PSD peak levels would not be measured by filters in a spectrum analyzer because the integral of the narrow peaks is constant. (The narrowing of the peaks with increased height does not appear in figure 64 beyond $\lambda = 1.0$ because of a 200 frequency point limitation in the spectrum calculation routine). Figure 65 shows that the streamwise turbulence length scale does not affect directivity of broadband or peak components.

The effects of changes in rotational Mach number (with constant rpm and constant blade force levels and statistics) are shown in figures 66 and 67. Conceptually, this corresponds to given forces, rotating at a given rpm but with the radius varying to vary the Mach number $\Omega R_e / c$. The M = 0 plot is a limiting case for $R_e \rightarrow 0$. With increasing Mach number, the level and number of harmonic peaks increase; then, particularly near M = 1, the broadband level increases. Beyond M = 1 there is little change. The effect on directivity shown in figure 67 is to change from a spherical pattern at M = 0 to an aft – dominated pattern for increased Mach number.

The effect on the noise spectrum of number of blades, with the same force statistics and level per blade, is shown in figure 68. The full scale values of the frequency axes were chosen to correspond to the same frequency in Hertz or the same harmonic of the shaft rotation frequency. As would be expected, the broadband level increases at 3 dB per doubling of blade number. The harmonic peaks are either cancelled or increase at 6 dB per doubling of number of blades at a given rotation harmonic. Changes in directivity for the BPF peak and the broadband level at 1.5 x BPF are shown in figure 69.

Finally, the effect of blade stagger angle is shown in figures 70 and 71. There is slightly more power radiated for the forces in the rotor plane ($\beta = 0°$) than for the forces aligned with the fan axis ($\beta = 90°$). The reason for the difference in power is apparent from the directivity plots in figure 71 where it is seen that the intensity reaches its maximum value in the plane of rotation for $\beta = 0°$ and on the axis for $\beta = 90°$.

Aeroacoustic Parametric Study

The accuracy of any study of effects due to changes in fan design parameters or operating conditions depends strongly on the form chosen for the unsteady lift response function. The various unsteady lift response theories and their assymptotic behaviors have been reviewed recently by Amiet (ref. 22) who gives the various solutions for different combinations of 2 versus 3 dimensionality of the flow and high versus low Mach number. The solutions are in terms of reduced frequency $k = \dfrac{\pi C_B}{\ell}$ where ℓ is the wavelength of the incoming disturbance and C_B is the blade chord. The lift response function S(k) is the ratio of unsteady lift to the unsteady lift which would have been obtained due to a disturbance of the same magnitude but occurring at very low frequency. Thus, the lift due to upwash harmonic u_n is given by

$$L_n = \frac{1}{2}\rho W^2 \, C_B \, \frac{dC_L}{d\alpha} \, \frac{u_n}{W} \, S(k) \tag{61}$$

where W is the mean inflow velocity. In the present study the behavior of S(k) for large k is needed. This was shown by Amiet to be either $S(k) \to (2\pi k)^{-1/2}$ or $S(k) \to (2\pi k)^{-1}$ depending on which assumptions are used for the calculation. For the present study, the relation

$$\lim_{k \to \infty} S(k) = (2\pi k)^{-1/2} \tag{62}$$

as in the Sears (ref. 18) theory is used.

The first portion of the Aeroacoustic Parametric Study was to investigate the effect of changes in number of rotor blades on rotor noise. Since the fan is assumed to be operating at a fixed rpm, pressure ratio, weight flow, diameter, etc., it is logical to assume that the incoming disturbances (i.e. u_n and ℓ_n) will be the same. However, when the number of blades B is changed, the blade chord C_B will be changed to preserve solidity (B C_B = constant). Thus, the variation in lift forces with B is given by

$$\frac{L_n}{L_{no}} = \frac{\frac{1}{2}\rho W^2 C_B \dfrac{dC_L}{d\alpha} \dfrac{u_n}{W} \sqrt{\dfrac{\ell_n}{2\pi^2 C_B}}}{\frac{1}{2}\rho W^2 C_{Bo} \dfrac{dC_L}{d\alpha} \dfrac{u_n}{W} \sqrt{\dfrac{\ell_n}{2\pi^2 C_B}}} = \sqrt{\frac{C_B}{C_{Bo}}} \tag{63}$$

or $L_n/L_{no} = \sqrt{B_o/B}$. Once the changes in force levels are defined, the noise spectra can be computed using the acoustic theory of Section 5 assuming that blade pressure levels vary as L_n/L_{no}. When the Q-Fan at flow condition 0-3B is used as the base case, the variation in noise with number of blades is as shown by the filtered power spectra in figure 72. The broadband component is unchanged but the harmonic peak levels can be reduced indefinitely by adding blades.

The second portion of the Aeroacoustic Parametric Study was to investigate the effect of variations in design tip speed of the rotor on rotor noise. Blade chord C_B and stagger β were varied to keep the same rotor thrust T at the same blade lift coefficient C_L according to the velocity diagram in figure 72. The axial velocity C_x was held constant at 138 m/sec (452 ft/sec). Lift at the 80% radius was calculated from $L = 1/2 \, \rho \, W_{0.8}^2 \, C_B \, C_L$ and thrust from $T = L \sin\beta$. With the steady flow condi-

tions determined as shown in the table of figure 73, the variations in unsteady blade pressures follow the ratio of lift harmonics:

$$\frac{L_n}{L_{no}} = \frac{\frac{1}{2}\rho W^2 C_B \frac{dC_L}{d\alpha} \frac{u_n}{W} \sqrt{\frac{\ell_n}{2\pi^2 C_B}}}{\frac{1}{2}\rho W_o^2 C_{Bo} \frac{dC_L}{d\alpha} \frac{u_n}{W_o} \sqrt{\frac{\ell_n}{2\pi^2 C_{Bo}}}} = \frac{W}{W_o} \sqrt{\frac{C_B}{C_{Bo}}} \qquad (64)$$

where it was assumed that $dC_L/d\alpha$, ℓ_n, and u_n are independent of blade chord and tip speed. The resulting variations in rotor noise power spectra for static operation due to changes in design tip speed are shown in figure 73. Reduced tip speed reduces broadband and harmonic peaks mostly at higher frequencies.

In the Aeroacoustic Parametric Study, investigation of the effect of varying number of blades or design tip speed was made possible by preserving fan diameter and axial velicity and assuming that the inlet turbulence structure was also preserved. This was required because no reliable theory exists which will predict variations in inlet turbulence with axial velocity or diameter. Even accepting this restriction, the accuracy of the study still depends on the accuracy of the lift response function used. Thus it is clear that further aeroacoustic studies of this nature should be based on a firmer understanding (either theoretical or empirical) of inlet turbulence fluid dynamics and unsteady lift response at high Mach number and frequency.

SECTION 7
SUMMARY AND CONCLUSIONS

The study of fan noise and inlet flow reported above was divided into three major areas. Conclusions from these are summarized below.

Conclusions From Inlet Flow Diagnosis

Turbulent flow entering the rotor of a subsonic tip speed fan during static, outdoor operation has been analyzed by use of pressure signals acquired from the surface of a rotating blade. A special type of waveform plot and a new form of blade pressure statistics have given qualitative and quantitative measures of the flow structure. The following are the major conclusions from the discussion in Section 4.

1. The inlet flow contains long, narrow "sausages" of turbulence. The flow remains partially coherent for 50 to 100 rotor revolutions and has a transverse correlation length corresponding to 15 to 30 degrees of rotor rotation.

2. Some of the eddies have a vortex-like structure and move circumferentially around the inlet as they pass through.

3. At low wind speeds the inlet turbulence exhibits a bimodal behavior. In one group the eddies are so short that they are chopped by a blade only once and and in the other group they are so long that they are chopped many times per revolution. This is the reason that inlet turbulence induced rotor noise appears to consist of two components: broadband and tones.

4. Pressure measured at the blade tip was compared with pressure measured at mid span to compare turbulence in the boundary layer of the shroud with turbulence ingested from the atmosphere. It was concluded that boundary layer turbulence in the usual sense is not an important noise source for the test fan. However, there are large disturbances induced in the boundary layer by the ingested turbulence. For fans with thicker boundary layers, these might be an important noise source.

Conclusions From Noise Diagnosis

A statistical blade loading model has been developed which fits measured rotor blade pressure spectra very satisfactorily and permits calculation of rotor sound power spectra due to interaction with inlet turbulence. These, coupled with theoretical predictions of rotor/stator interaction noise, have been compared with measured narrowband sound power spectra from a fan running statically outdoors. The following are the major conclusions from the discussion in Section 5.

41

1. Fan noise at frequencies near the first three harmonics of blade passing frequency is influenced about equally by rotor and stator radiation. However, at higher frequencies the stator influence diminishes rapidly and the rotor radiation dominates. This conclusion applies to broadband and harmonic peak components (apparent tones) over pressure ratios from 1.08 to 1.15 and tip speeds from 170 m/sec (580 ft/sec) to 240 m/sec (800 ft/sec).

2. Measured blade pressure spectra contain a broadband component plus up to 100 peaks at harmonics of the shaft rotation frequency.

3. The trend in measured spectrum level for both noise and blade pressure at constant fan pressure ratio but varying tip speed is to decrease at higher tip speeds.

4. The Lowson – Scheiman blade "loading law" which was developed originally for calculation of tone noise due to harmonic blade forces was found to be a consequence of the statistical blade loading model derived here for calculation of noise due to inlet turbulence.

5. A form for the Bessel function power integral was found which permits calculation of sound power for about the same computer time as a single sound pressure field point.

Conclusions From Parametric Studies

The theory developed for rotor diagnosis was used in two parametric studies. In the first, effects on rotor noise spectra and directivity were evaluated for changes in turbulence properties, rotational Mach number, stagger angle, and number of blades. Understanding the sensitivity to these variables provided the basis for using the rotor theory as a diagnostic tool.

In the second study variations in design tip speed and number of blades were studied using a test fan as the base case. Results indicate reduced noise for many blades and low tip speed (high solidity).

Future Direction For Fan Noise Research

The ability to measure unsteady surface pressures inside a fan is invaluable in the analysis of noise sources since they cannot be predicted reliably at high Mach number and high frequency. Further work using this technique should be conducted for the study of stator as well as rotor sources and should be applied to the forward flight condition to find the effect on the structure of inlet turbulence and the role of the shroud boundary layer.

The discovery that rotor blade pressures dropped with increased tip speed (reduced blade loading) at constant fan pressure ratio holds important potential for noise reduction. Since Goldstein and Atassi (ref. 15) have provided an analytical basis for this effect, a combined theoretical and experimental program would be useful for exploring the effect of steady blade loading on airfoil unsteady pressures and noise. Understanding this phenomenon may lead to fan designs with reduced rotor and stator noise.

APPENDIX A
EFFECTIVE CHORD ANALYSIS

In deriving the theory of Section 5 an effective chord C_e was introduced which was defined to be that length, which when multiplied by the measured blade pressure, gives the true lift/unit span at the radius of the pressure transducer. Since C_e is to be used to predict rotor noise from the blade pressure, it is best determined by an acoustic "calibration" in which blade pressure and the resulting sound pressure are measured simultaneously. To be sure that the blade pressure was truely the source of the measured sound, the inlet flow was intentionally distorted by the cylindrical post shown in figure 9 which raised the noise and blade pressure about 10 dB. The effective chord can be calculated from the ratio of sound pressure on the fan axis to blade pressure by treating the cylindrical post as a single inlet guide vane for each blade stagger and tip speed of interest. Thus, the acoustic calibration automatically takes into account effects on blade pressure response of compressibility, reduced frequency, camber, thickness, and cascading which cannot be calculated reliably with existing unsteady aerodynamic theory.

From the results of reference 23 and the effect of chordwise pressure distribution introduced in Section 5, it can be shown that the rms sound pressure on the fan axis at observer distance r due to a single inlet guide vane is

$$\sqrt{\overline{p_{sm}^2}} = \frac{m \left| \nu_{mB} \right| B^2 \, M \sin\beta}{4\pi r \, R_e} \sqrt{\overline{L_{mB}^2}} \tag{65}$$

at the m th harmonic of blade passing frequency. $\sqrt{\overline{L_{mB}^2}}$ is the rms value of blade lift at the mB th harmonic of shaft rotation frequency which, by definition is $C_e (R_T - R_H) \sqrt{\overline{p_{bmB}^2}}$. This leads to

$$\frac{C_e}{C_B} = \frac{4\pi}{m \left| \nu_{mB} \right| B^2 \, M \sin\beta} \left(\frac{R_e}{R_T - R_H} \right) \left(\frac{r}{C_B} \right) \sqrt{\frac{\overline{p_{sm}^2}}{\overline{p_{bmB}^2}}} \tag{66}$$

as the ratio of effective chord to chord. Table 4 shows values of C_e/C_B computed for the blade passing frequency fundamental (m = 1) for conditions corresponding to the clean inlet conditions where sound power spectra are available.

These values of C_e/C_B were used in the rotor noise predictions which appeared in figures 53, 55, and 56 using equations 55 and 57. There was one exception, however: the value $C_e/C_B = 0.224$ for test condition I-7 gave predicted values judged to be abnormally low for condition 0-7B. For this case only (figure 56 b) the average value 0.701 for C_e/C_B was used.

In order to compute the spectrum levels given by equations 53, 55, and 57, the quantities Q_{xm}, S_{xm}, W_{smn}, and S_{smn} have to be evaluated from:

$$Q_{xm} = \overline{a_v^2 \, w_v^3 \, (2\pi\lambda_v)^2 \, \left| F(w_v \Omega_x) \right|^2 \, L_m} \Big/ T^2 \, p_o^2$$

$$S_{xm} = 1.58 \, \overline{a_v^2 \, w_v^3 \, (2\pi\lambda_v) \, \left| F(w_v \Omega_x) \right|^2} \Big/ T^2 \, p_o^2 \tag{54}$$

and

$$Q_{sm} = \overline{a_v^2 \, w_v^4 \, (2\pi B \lambda_v)^2 \, \left| F\left[w_v \Omega (By_m + n) \right] \right|^2 \, L_m} \Big/ T^2 \, p_o^2$$

$$S_{smn} = 1.58 \, \overline{a_v^2 \, w_v^4 \, (2\pi B \lambda_v) \, \left| F\left[w_v \Omega (By_m + n) \right] \right|^2} \Big/ T^2 \, p_o^2 \tag{56}$$

The overbars imply ensemble averages over the random variables a, w, and λ according to probability integrals of the type $\overline{(\quad)} = \iiint (\quad) f(a, w, \lambda) \, da \, dw \, d\lambda$. Thus, a form for the joint probability density function $f(a, w, \lambda)$ must be chosen which is general enough to permit empirical fitting of the theoretical spectra to the measured spectra.

$f(a, w, \lambda)$ can be expressed in terms conditional probability functions:

$$f(a, w, \lambda) = f_{a/w, \lambda}(a/w, \lambda) \, f_{w/\lambda}(w, \lambda) \, f_\lambda(\lambda) \tag{67}$$

where $f_{a/w, \lambda}(a/w, \lambda)$ is the "probability density of a, given w and λ"; $f_{w/\lambda}(w/\lambda)$ is the "probability density of w, given λ"; and $f_\lambda(\lambda)$ is the probability density function for λ. This form permits the statistics of the width of an eddy to depend on its length (i. e. long eddies tend to have different widths than short eddies), etc.

Very general forms for the density functions were chosen as follows.

$$f_{a/w, \lambda} \ (a/w, \lambda) = \frac{e^{-a^2/2A^2}}{A \sqrt{2\pi}} \tag{68}$$

$$f_{w/\lambda} \ (w/\lambda) = \frac{w^{(\gamma_1 - 1)} \ e^{-w/W}}{W^{\gamma_1} \ \Gamma(\gamma_1)} \tag{69}$$

$$f_\lambda(\lambda) = \frac{\lambda^{(\gamma_2 - 1)} \ e^{-\lambda/L}}{L^{\gamma_2} \ \Gamma(\gamma_2)} \tag{70}$$

where

$$A^2 = \sum_i A_i \left(\frac{w}{W}\right)^i + \sum_j B_j \left(\frac{\lambda}{L}\right)^j \tag{71}$$

$$W = \sum_k W_k \left(\frac{\lambda}{L}\right)^k \tag{72}$$

Equation (68) states that the eddies with given w and λ have a Gaussian distribution for pulse envelope amplitude a. The mean square value of a is given by the power series for A^2 in equation 71 which shows its dependence on eddy width w and length λ . The density function for the eddy width $f_{w/\lambda}$ (w/λ) is a gamma density function of order γ_1 with mean value depending an eddy length through a power series for W. Finally the density function for eddy length f_λ (λ) is a gamma function of order γ_2 and mean eddy length $\gamma_2 L$.

When the above form for f(a, w, λ) is used to compute the Q's and the S's, the intergrals over a and w can be evaluated analytically leaving single integrals over λ

which must be done numerically. With the substitution $z = \lambda/L$, the results for computing blade pressure spectra are

$$
Q_{xm} = \frac{\pi^2 L^2}{\Gamma(\gamma_1) \Gamma(\gamma_2)} \sum_i A_i \; \Gamma(i + \gamma_1 + 3) \int_0^\infty \frac{z^{\gamma_2+1}}{W^{\gamma_1+i}} \frac{L_m(z) \; e^{-z} dz}{(4\pi x + 1/W)^{\gamma_1+i+3}}
$$

$$
+ \frac{\pi^2 L^2 \gamma_1 (\gamma_1+1)(\gamma_1+2)}{\Gamma(\gamma_2)} \sum_j B_j \int_0^\infty \frac{z^{\gamma_2+j+1} L_m(z) \; e^{-z} \; dz}{W^{\gamma_1} (4\pi x + 1/W)^{\gamma_1+3}}
$$

(73)

and

$$
S_{xm} = \frac{1.58 \pi L}{2 \Gamma(\gamma_1)\Gamma(\gamma_2)} \sum_i A_i \Gamma(\gamma_1 +i+3) \int_0^\infty \frac{z^{\gamma_2} \; e^{-z} \; dz}{W^{\gamma_1+i} (4\pi x + 1/W)^{\gamma_1+i+3}}
$$

$$
+ \frac{1.58 \pi L \gamma_1 (\gamma_1+1)(\gamma_1+2)}{2 \Gamma(\gamma_2)} \sum_j B_j \int_0^\infty \frac{z^{j+\gamma_2} \; e^{-z} \; dz}{W^{\gamma_1} (4\pi x + 1/W)^{\gamma_1+3}}
$$

(74)

For the sound pressure and sound power spectra the results are

$$
Q_{smn} = \frac{(\pi BL)^2}{\Gamma(\gamma_1) \Gamma(\gamma_2)} \sum_i A_i \; \Gamma(\gamma_1 +i +4) \int_0^\infty \frac{z^{\gamma_2+1} L_m(z) \; e^{-z} \; dz}{W^{\gamma_1+i} (4\pi |By+n| + 1/W)^{\gamma_1+i+4}}
$$

$$
+ \frac{(\pi BL)^2 \gamma_1 (\gamma_1+1)(\gamma_1+2)(\gamma_1+3)}{\Gamma(\gamma_2)} \sum_j B_j \int_0^\infty \frac{z^{\gamma_2+j+1} L_m(z) \; e^{-z} \; dz}{W^{\gamma_1} (4\pi |By+n| + 1/W)^{\gamma_1+4}}
$$

(75)

49

and

$$S_{smn} = \frac{1.58\pi BL}{2\Gamma(\gamma_1)\Gamma(\gamma_2)} \sum_i A_i \Gamma(\gamma_1 + i + 4) \int_0^\infty \frac{z^{\gamma_2} e^{-z} dz}{W^{\gamma_1 + i} (4\pi |By + n| + 1/W)^{\gamma_1 + i + 4}}$$

(76)

$$+ \frac{1.58\pi BL \gamma_1(\gamma_1 + 1)(\gamma_1 + 2)(\gamma_1 + 3)}{2\Gamma(\gamma_2)} \sum_j B_j \int_0^\infty \frac{z^{\gamma_2 + j} e^{-z} dz}{W^{\gamma_1} (4\pi |By + n| + 1/W)^{\gamma_1 + 4}}$$

The integrals were performed with a 10 point Laguerre scheme as described by Abramowitz and Stegun (ref. 24). In order to achieve the fit of theoretical to measured spectra the statistical parameters listed in table 5 were used.

APPENDIX C
LOADING LAWS FOR ROTOR BLADE FORCES

In their study of helicopter rotor noise Lowson and Ollerhead (ref. 25) generated a theoretical equation giving noise harmonic levels in terms of blade harmonic loads. In their study it was found that typically 60 blade load harmonics were required for accurate noise predictions. Since this data was not available, an empirical loading law was developed in a form which has since been used by other investigators for noise prediction of propellers and fan rotors as well as helicopters. In developing the loading law concept, Lowson and Ollerhead noticed that Scheiman's measured load data (ref. 26) for 10 harmonics fell approximately on straight lines when plotted on log - log paper. This observation was extrapalated to any desired harmonic order by the "loading law",

$$L_n = L_N (n - N)^{-k}$$

which gives the n th loading harmonic L_n in terms of an intercept L_N for the N th harmonic and a slope $-k$. The best fit to the data was obtained with N = 0 giving $L_n = L_0 n^{-k}$. The use of the loading law has since been carried to the point where measured noise levels are used to compute blade loads.

In the present study the loading law concept was verified both expermentally and theoretically. When the same spectra plotted in figures 50 and 54 were plotted with logarithmic frequency axis as shown at the top in figure 74, the harmonic peaks indeed fall nearly on a straight line for the spectrum from the mid blade transducer. The tip transducer spectrum shown at the bottom deviates more from the straight line behavior, particularly at high frequency. Similar results are shown in figures 75 and 76 for the 6 other flow conditions tested.

An attempt was made to find a systematic dependence on pressure ratio and tip speed of the slopes and intercepts of the straight lines in figure 75. It was found that the intercepts increased monotonically with pressure ratio at constant blade angle (flow conditions 0-1, 0-2, 0-3, and 0-4). However, at constant pressure ratio (conditions 0-5, 0-3, 0-6, and 0-7), no simple relation was found. The outstanding case was 0-7 which had a flatter slope and lower intercept than the others. It is not known whether this is due to an extreme of tip speed, blade angle, or loading because not enough parameters could be varied in the test. However, future development of unsteady aerodynamics would be greatly aided by further tests of this sort.

It was found that the theoretical blade loading model presented in Section 5 establishes a theoretical basis for Lowson - Scheiman loading law. This can be seen by examination of equation (73) in which frequency dependent terms are

$$P_Q = (x + 1/4\pi W)^{-(\gamma_1 + i + 3)} \tag{78}$$

and

$$P_S = (x + 1/4\pi W)^{-(\gamma_1 + 3)} \tag{79}$$

where $x = \omega/\Omega$ is the harmonic of shaft rotation frequency. These have the same form as equation (77) and, since equation (73) is a linear combination of the terms P_Q and P_S, it follows that the theory predicts blade pressure spectra with peaks behaving according to the older loading law. If more than one of the A_i's in equation 73 is non-zero, the log-log plot of harmonic loads will consist of more than one straight line section.

Now Scheiman's original observations were for blade section lift coefficient which corresponds to blade pressure as far as spectrum slope is concerned. However, the noise radiation equations required integrating the blade pressure distributions spanwise to get the total lift per pulse. Since lift pulse amplitude is proportional to the spanwise scale of the pressure pulse, the lift statistics must be different from the blade pressure statistics. In fact, it can be deduced from equation (75) that the frequency dependent terms in the lift spectrum which correspond to P_Q and P_S are

$$L_P = (x + 1/4\pi W)^{-(\gamma_1 + i + 4)} \tag{80}$$

$$L_Q = (x + 1/4\pi W)^{-(\gamma_1 + 4)} \tag{81}$$

Thus, the slope of the lift spectrum is greater than the slope of the blade pressure spectrum by −1. On an amplitude (rather than power) basis the difference would be − 1/2.

This difference in loading laws for blade pressure or section lift (which has been measured) versus integrated lift (which is used in the noise formulas) was recognized by Lowson and Ollerhead (ref. 25). By incorporating a spanwise correlation length,

a concept from random flow analysis, in their loading law for harmonic rotor radiation, Lowson and Ollerhead arrived at exactly the same difference of $-1/2$ in the slope of the loading law which has been derived from the blade pressure model of this report.

The frequency dependence of blade loading spectra revealed above arose from the fact that there is a distribution of eddy widths and amplitudes (and therefore pulse widths and amplitudes). The generality of the straight line loading law results is impressive when it is recognized to hold for any statistical distribution of the eddy parameters, that is any values for γ_1, γ_2, L, and the A_i's, B_j's and W_k's of equations (68) through (72). Thus, the older loading law originally used in the analysis of discrete noise appears to be an inevitable result of the rotor operating in turbulent flow. Note also that the law, in generalized form, also applies to the broadband loading component as well as the narrowband component.

REFERENCES

1. Hanson, Donald B.: Unified Analysis of Fan Stator Noise. J. Acoust. Soc. Am., vol. 54, no. 6, Dec. 1973.

2. Hanson, Donald B.: Spectrum of Rotor Noise Caused by Atmospheric Turbulence. J. Acoust. Soc. Am., vol. 56, no. 1, July 1974.

3. Hanson, Donald B.: Measurements of Static Inlet Turbulence. Preprint no. 75-467, Am. Inst. Aeron. and Astronaut., March 1975.

4. Cumpsty, N. A.; and Lowrie, B. W.: The Cause of Tone Generation by Aero-Engine Fans at High Subsonic Tip Speeds and the Effect of Forward Speed. J. Eng. Power, vol. 96, no. 3, July 1974.

5. Favre, A. J.; Gaviglio, J. J.; and Dumas, R. J.: Further Space-Time Correlations of Velocity in a Turbulent Boundary Layer. J. Fluid Mech., vol. 3, 1957-58.

6. Schubauer, G. B.; and Klebanoff, P. S.: Investigation of Separation of the turbulent Boundary Layer. NACA TR-1030, 1951.

7. Levintan, R. M.: The Q-Fan^{TM} Demonstrator Engine. Preprint no. 73-1215, Am. Inst. Aeron. and Astronaut., Nov. 1973.

8. Bendat, J. S.; and Piersol, A. G.: Measurement and Analysis of Random Data. John Wiley and Sons, Inc., 1966.

9. Otnes, Robert K.; and Enochson, Loren: Digital Time Series Analysis. John Wiley and Sons, Inc., 1972.

10. Goldstein, Marvin E.; Dittmar, James H.; and Gelder, Thomas F.: Combined Quadrupole - Dipole Model for Inlet Flow Distortion Noise from a Subsonic Fan. NASA TN-D-7680, 1974.

11. Magliozzi, B.; Hanson, D. B.; Johnson, B. V.; and Metzger, F. B.: Noise and Wake Structure Measurements in a Subsonic Tip Speed Fan. NASA CR 2323, 1973.

12. Silverstein, Abe; Katzoff, S.; Bullivant, Kenneth W.: Downwash and Wake Behind Plain and Flapped Airfoils. NACA Rept. No. 651, 1939.

13. Hill, P. G.; Schaub, U. W.; and Senoo, Y: Turbulent Wakes in Pressure Gradients. J. App. Mech., vol. 30, no. 4, Dec. 1963.

14. Metzger, F. B.: Progress in Source Noise Supression of Subsonic Tip Speed Fans. Preprint no. 73-1032, Am. Inst. Aeron. and Astronaut., Oct. 1973.

15. Goldstein, Marvin E.; and Atassi, H.: A Complete Second Order Theory for the Unsteady Flow About an Airfoil Due to a Periodic Gust. Paper submitted to J. Fluid Mech. 1974.

16. Hanson, Donald B.: The Spectrum of Turbomachine Rotor Noise Caused by Inlet Guide Vane Wakes and Atmospheric Turbulence. Ph.D. Thesis, Univ. of Conn., 1973.

17. Ffowcs-Williams, J.E.; and Hawkings, D.L.; Theory Relating to the Noise of Rotating Machinery. J. Sound and Vib., vol. 10, no. 1, 1969.

18. Sears, W.R.: Some Aspects of Nonstationary Airfoil Theory and Its Practical Application. J. Aerospace Sci., vol. 8, no. 2, 1941.

19. Embleton, T.W.F.: Relation of the Mechanical Power of a Propeller to Radiated Power of the Resulting Acoustic Sources. J. Acout. Soc. Am., vol. 34., no. 6, 1962.

20. Lowson, M.V.: Theoretical Studies of Compressor Noise. NASA CR-1287, 1969.

21. Bailey, W.N.: Some Integrals Involving Bessel Functions. Quart. J. Math. Oxford Ser. 9, 1938.

22. Amiet, R.K.: Effects of Compressibility in Unsteady Airfoil Lift Theories. Paper presented at Symposium on Unsteady Aerodynamics, U. of Arizona, March 1975.

23. Hanson, Donald B.: Spectrum of Rotor Noise Caused by Inlet Guide Vane Wakes. J. Acoust. Soc. Am., vol. 55, no. 6, June 1974.

24. Abramowitz, Milton; and Stegun, Irene A.; eds.: Handbook of Mathematical Functions. NBS Appl. Math. Ser. 55, U.S. Dept of Commerce, June 1964.

25. Lowson, M.V.; and Ollerhead, J.B.: A Theoretical Study of Helicopter Rotor Noise., J. Sound and Vib., vol. 9, no. 2, 1969.

26. Scheiman, J.: A Tabulation of Helicopter Rotor-Blade Differential Pressures, Stresses, and Motions as Measured in Flight. NASA TM-X-952, 1964.

TABLE 1

FAN TEST CONDITIONS

Test cond	Blade angle degrees (a)	Tip speed (m/sec)	Tip speed (ft/sec)	Axial velocity (m/sec) (b)	Fan pressure ratio	Wind speed (knots)	Wind direction degrees from inlet axis (c)	Sound power spectrum available?
Distortion cylinder in								
I-1	56.8	124	406	81	1.045	1-2	Variable	No
I-2	56.8	167	557	110	1.084	1-2	Variable	No
I-3	56.8	203	668	133	1.120	1-2	Variable	No
I-4	56.8	231	758	156	1.149	1-2	Variable	No
I-5	59.8	191	627	129	1.115	1-2	Variable	No
I-6	51.8◆	223	733	138	1.127	1-2	Variable	No
I-7	46.8	238	782	132	1.116	1-2	Variable	No
Distortion cylinder out								
0-1	56.8	124	406	81	1.045	1-2	180	No
0-2	56.8	167	557	110	1.084	1-3	90	Yes
0-3A	56.8	203	668	133	1.170	1-3	90	No
0-3B	56.8	203	668	133	1.170	3-6	180	Yes
0-4	56.8	231	758	156	1.149	6-10	90	Yes
0-5A	59.8	191	627	129	1.115	1-3	90	No
0-5B	59.8	191	627	129	1.115	10-16	90	Yes
0-6	51.8	223	733	138	1.127	2-4	90	No
0-7A	46.8	238	782	132	1.116	2-4	180	No
0-7B	46.8	238	782	132	1.116	3-6	90	Yes

[a]At 3/4 radius.

[b]As calculated at 3/4 radius.

[c]Wind direction typically varied ±50° during 20 second runs.

TABLE 2

BLADE PRESSURE RMS VALUES AND CROSSCORRELATION COEFFICIENTS

Test cond	RMS pressures				Ratio: $\dfrac{\text{Tip}}{\text{Mid}}$	Crosscorrelation coef		Ratio: $\dfrac{\text{Turb}}{\text{Total}}$
	Tip location		Mid blade			Turbulent only ρ'_{pq}	Total ρ_{pq}	
	Pa	psi	Pa	psi				
0-1	643	0.0933	293	0.0426	2.19	0.468	0.624	1.33
0-2	1000	.145	492	.0713	2.03	.436	.670	1.54
0-3A	2190	.318	1000	.146	2.18	.330	.663	2.01
0-4	2030	.295	1030	.149	1.98	.387	.450	1.17
0-5A	1220	.163	670	.0974	1.68	.510	.662	1.29
0-5B	2760	.400	1540	.224	1.78	.670	.684	1.02
0-6	983	.143	558	.0811	1.76	.312	.477	1.52
0-7	1060	.154	608	.0882	1.74	.310	.453	1.46

TABLE 3

NARROW BAND SOUND POWER SPECTRA[a]

| Harmonic of blade passing frequency | Test cond | 0-2 | 0-3B | 0-4 | 0-5B | 0-7B |
	Bandwidth Hz	24	28	32	27	33
0.5		128.1	133.2	135.3	133.5	131.1
1.0		134.5	145.2	145.3	143.6	140.8
1.5		125.6	130.1	131.6	130.3	127.2
2.0		131.2	137.6	141.2	139.6	134.0
2.5		121.4	124.7	126.7	125.8	122.5
3.0		127.1	134.3	135.8	133.9	129.7
3.5		118.0	122.0	124.7	123.0	120.4
4.0		122.7	128.7	130.3	129.2	126.0
4.5		114.9	119.8	122.6	121.0	117.8
5.0		120.2	126.4	128.1	126.7	124.9
5.5		112.8	119.1	120.7	120.1	116.4
6.0		117.7	123.5	125.2	123.7	121.7
6.5		111.9	117.3	119.6	118.3	115.3
7.0		116.5	121.0	121.8	121.4	120.5

[a] dB relative to 10^{-13} watts in stated bandwidth. Calculated from narrowband spectra measured every 10° around fan at 7.62 meters (25 ft).

TABLE 4

VALUES OF EFFECTIVE CHORD

Test cond	Tip speed m/sec	Rotor stagger (0.8 radius)	Ambient temp °C	SPL_1 dB	BPL_{13} dB	$\left(p^2_{s1}/p^2_{b13}\right)^{1/2}$	C_e/C_B
I-2	167	40°	−6	112	138	0.0501	0.746
I-3	203	40°	−4	109.5	133	.0668	.831
I-4	231	40°	+6	111.5	139.5	.0398	.443
I-5	191	37°	−4	112	133	.0891	1.263
I-7	238	50°	−4	110.5	142.5	.0251	.224

Average   0.701

TABLE 5

STATISTICAL PARAMETERS USED IN FIT OF BLADE PRESSURE SPECTRA

[Notation defined in Appendix B]

Test cond	σ_a	C_e/C_B	N	γ_1	B_1	W_0	$\bar{w}$
0-2	0.7	0.746	1.44×10^{17}	3.0	0.08	0.01667	0.050
0-3B	.7	0.831	1.28×10^{18}	3.1	.05	0.00645	.020
0-4	.7	0.443	2.56×10^{19}	3.5	.01	0.00428	.015
0-5B	.8	1.263	6.42×10^{16}	2.9	.08	0.03448	.100
0-7B	.6	0.224	4.05×10^{16}	2.0	.60	0.01500	0.030

These values apply for all test conditions:

$$\sigma = 0.004$$

$$\mu = 0.5$$

$$R_e/R_T = 0.8$$

$$\gamma_2 = 1.0$$

$$L(= \bar{\lambda}) = 1.5$$

$$A_{-4} = 1.0$$
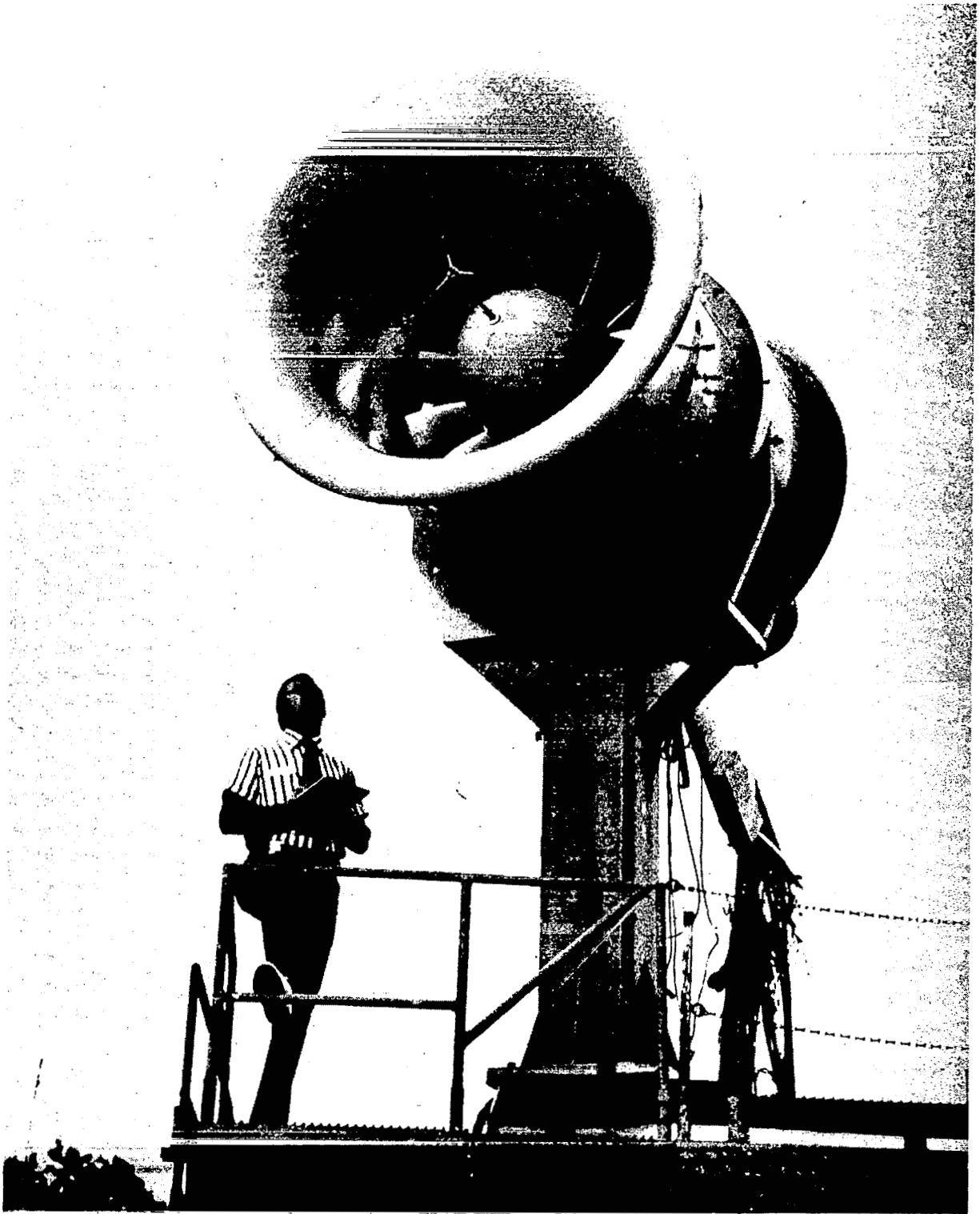
FIGURE 1. TEST FAN FOR INLET FLOW AND NOISE STUDIES
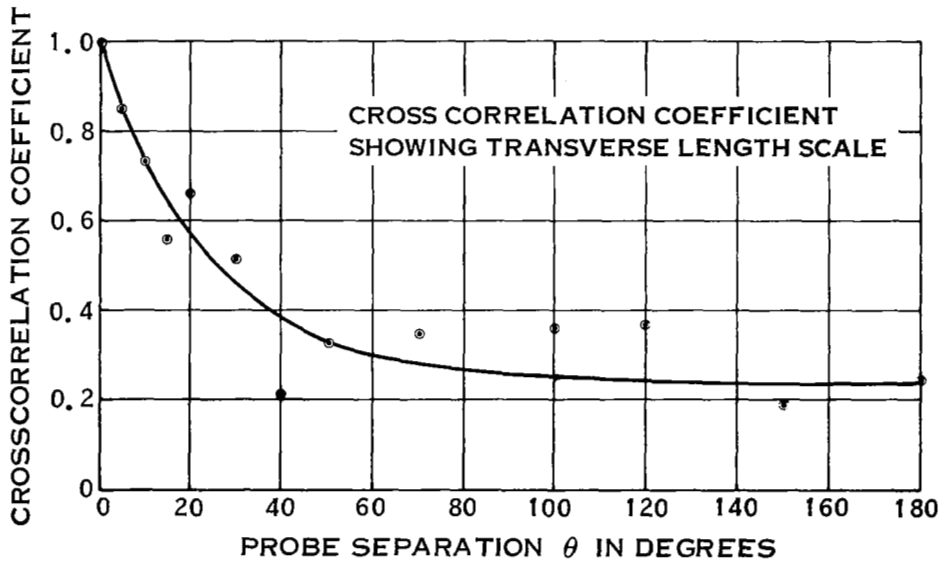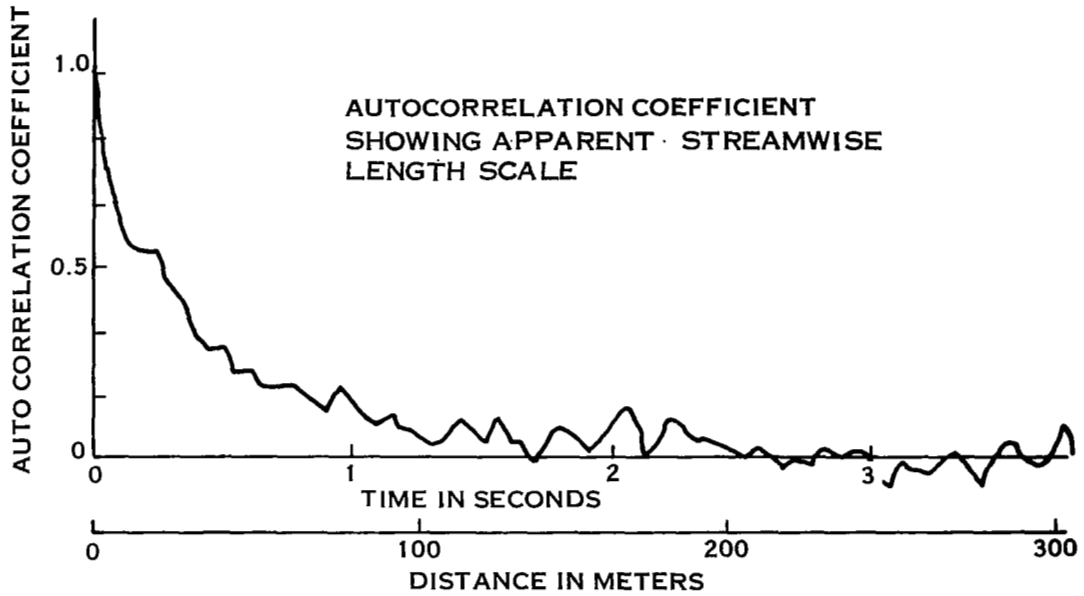
FIGURE 2   TURBULENCE CORRELATION COEFFICIENTS
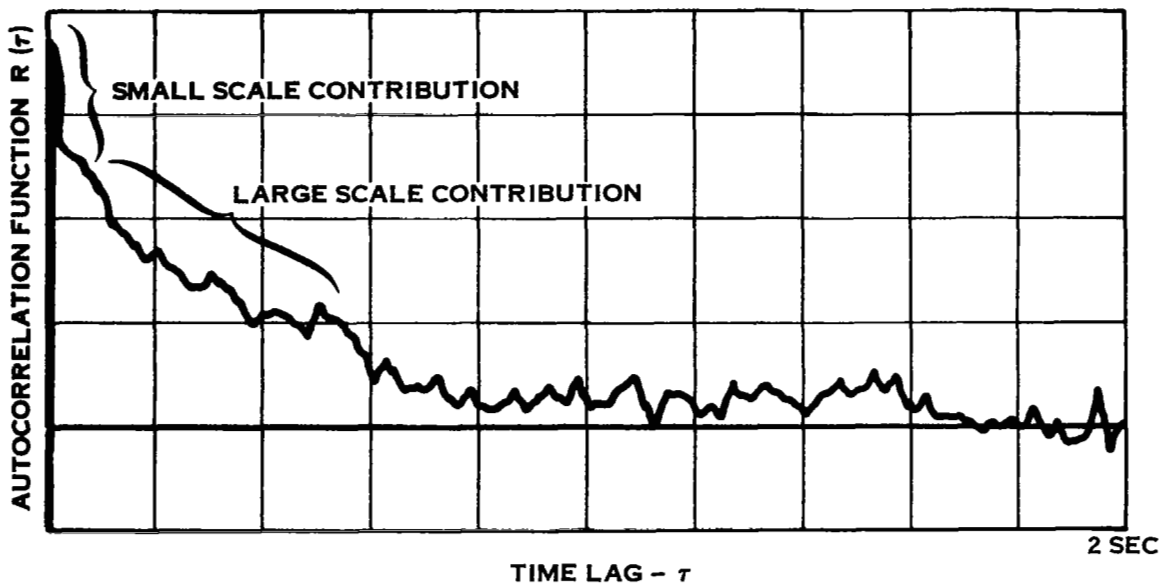
FIGURE 3 CORRELEGRAM SHOWING EVIDENCE OF TWO LENGTH SCALES

STATIC POTENTIAL
FLOW FIELD

TURBULENT EDDY

STREAMLINE

TRANSVERSE
VELOCITY COMPONENTS
INCREASE DURING
CONTRACTION TO
PRESERVE ANGULAR
MOMENTUM

TURBULENCE EDDIES STRETCHED BY CONTRACTING FLOW

INLET POTENTIAL FLOW FIELD IN FORWARD FLIGHT

TURBULENT
EDDY

FLIGHT DIRECTION ➤

TURBULENT EDDIES NOT SUBSTANTIALLY
MODIFIED IN FORWARD FLIGHT
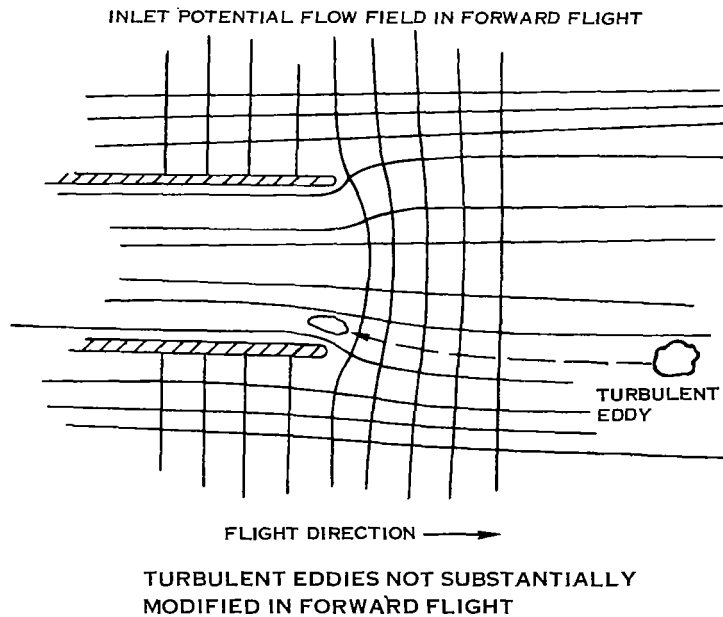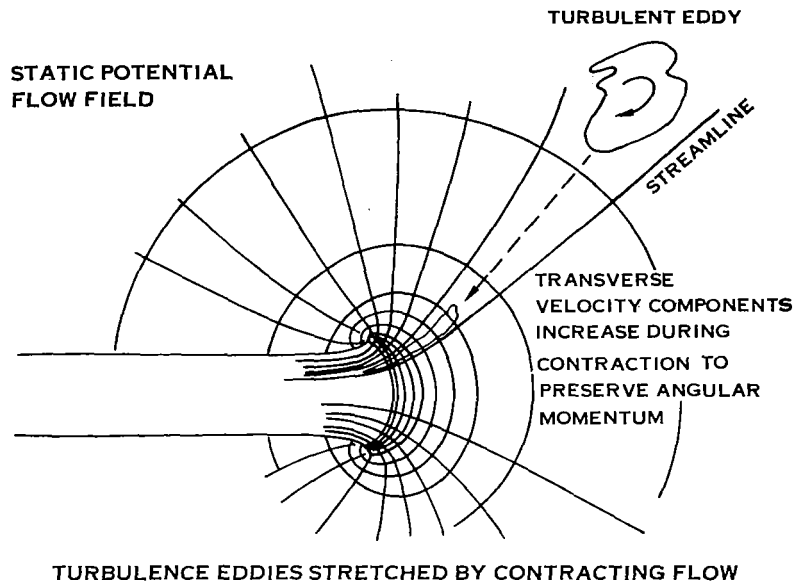
FIGURE 4.   EFFECT OF FORWARD FLIGHT ON
INGESTED ATMOSPHERIC TURBULENCE

66

1.40 M (55 IN.)
DIAMETER

13 BLADES

7 VANES

SUPPORT POST
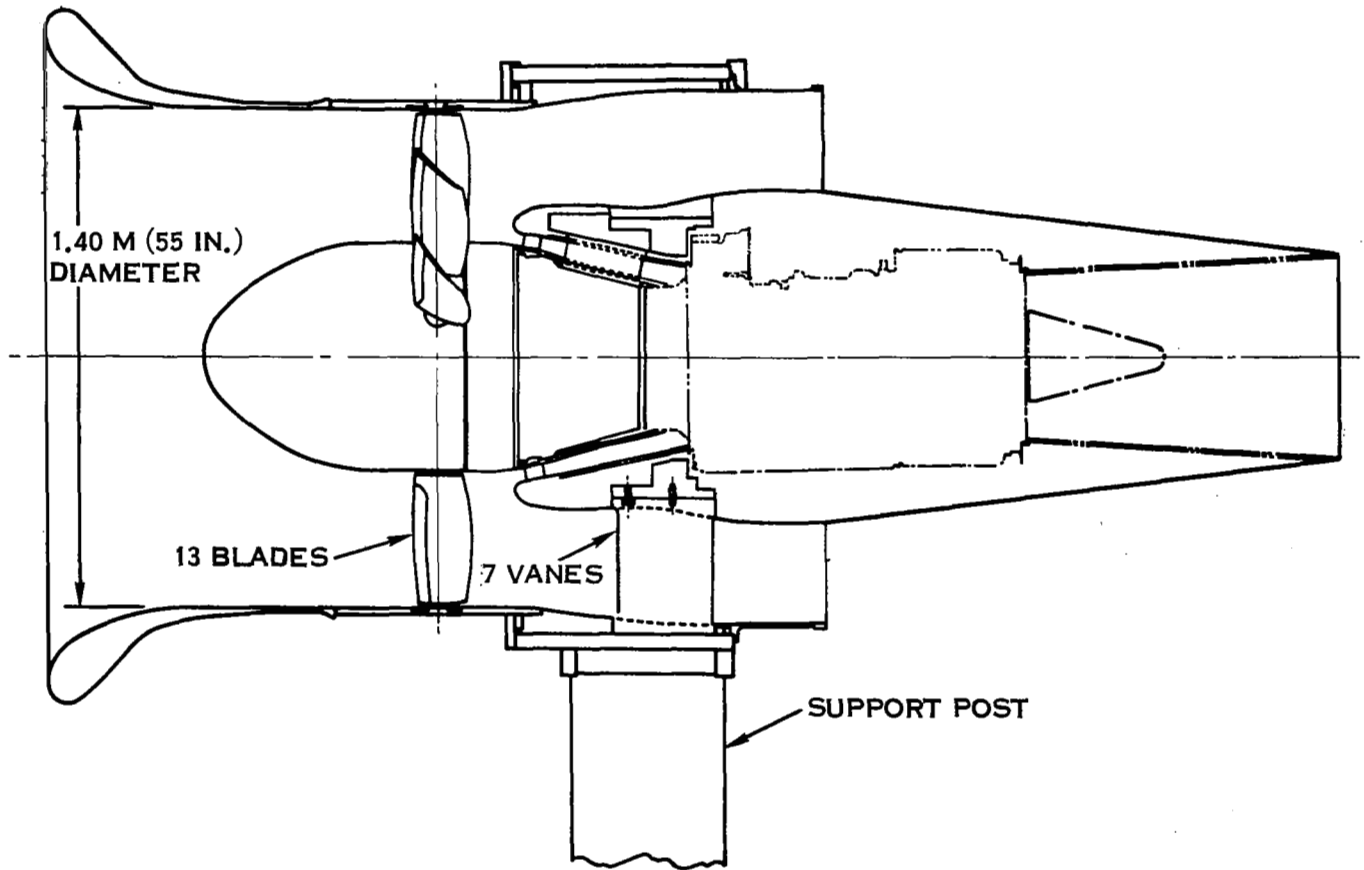
FIGURE 5. TEST VEHICLE — 1.4 M DIAMETER Q-FAN DEMONSTRATOR
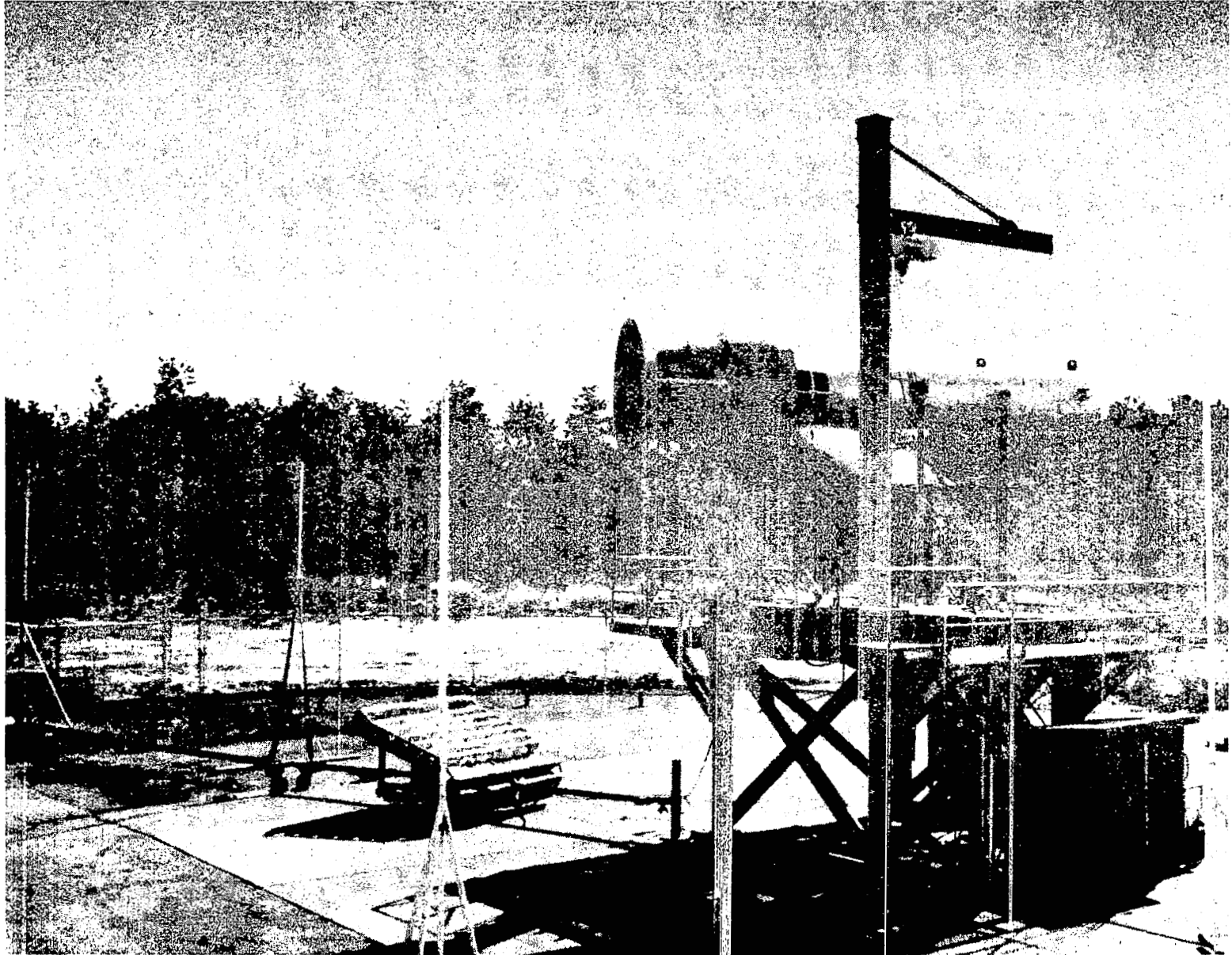
FIGURE 6. TEST FAN WITH TRAVELLING MICROPHONE

LEADING EDGE

PRESSURE SIDE

(INCHES)
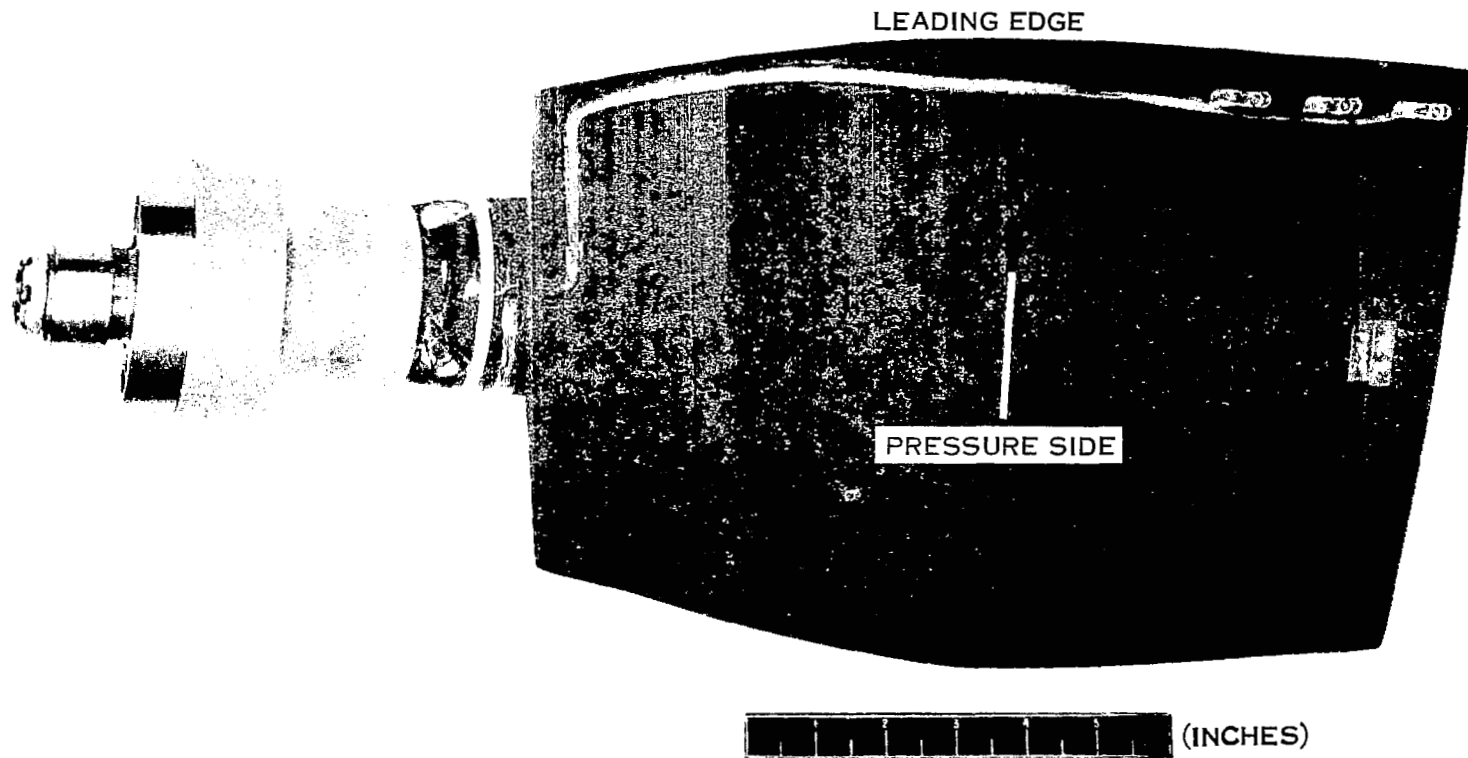
FIGURE 7. TYPICAL INSTALLATION OF PRESSURE TRANSDUCERS ON FAN BLADE
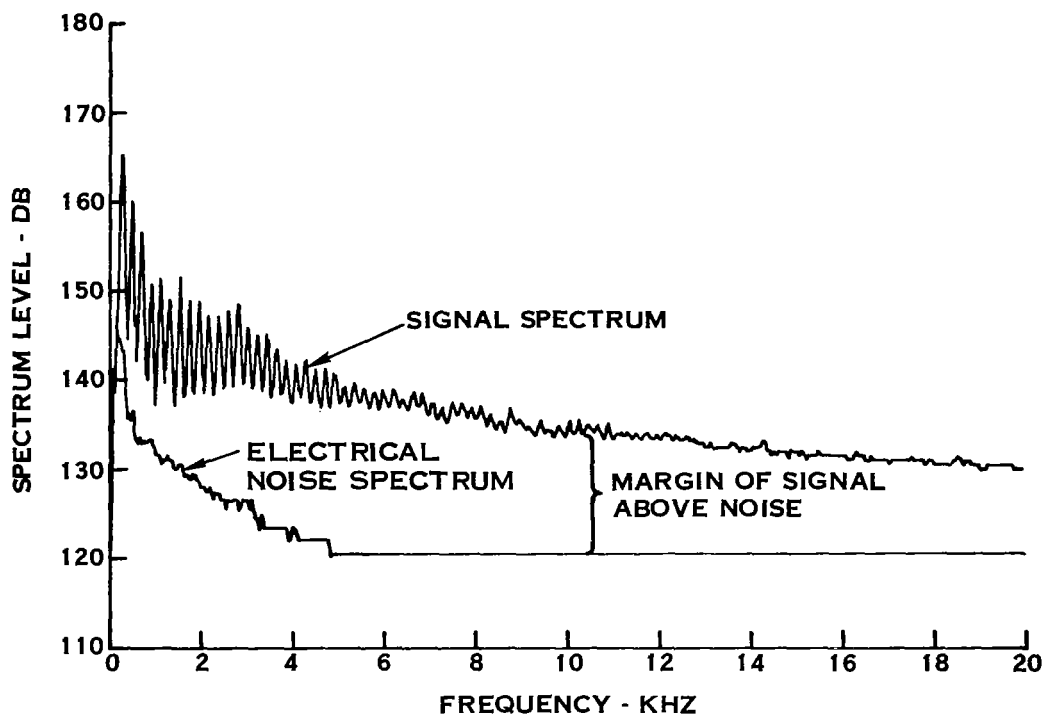
FIGURE 8   MARGIN OF SIGNAL OVER NOISE VS. FREQUENCY
(SIGNAL-TO-NOISE RATIO)
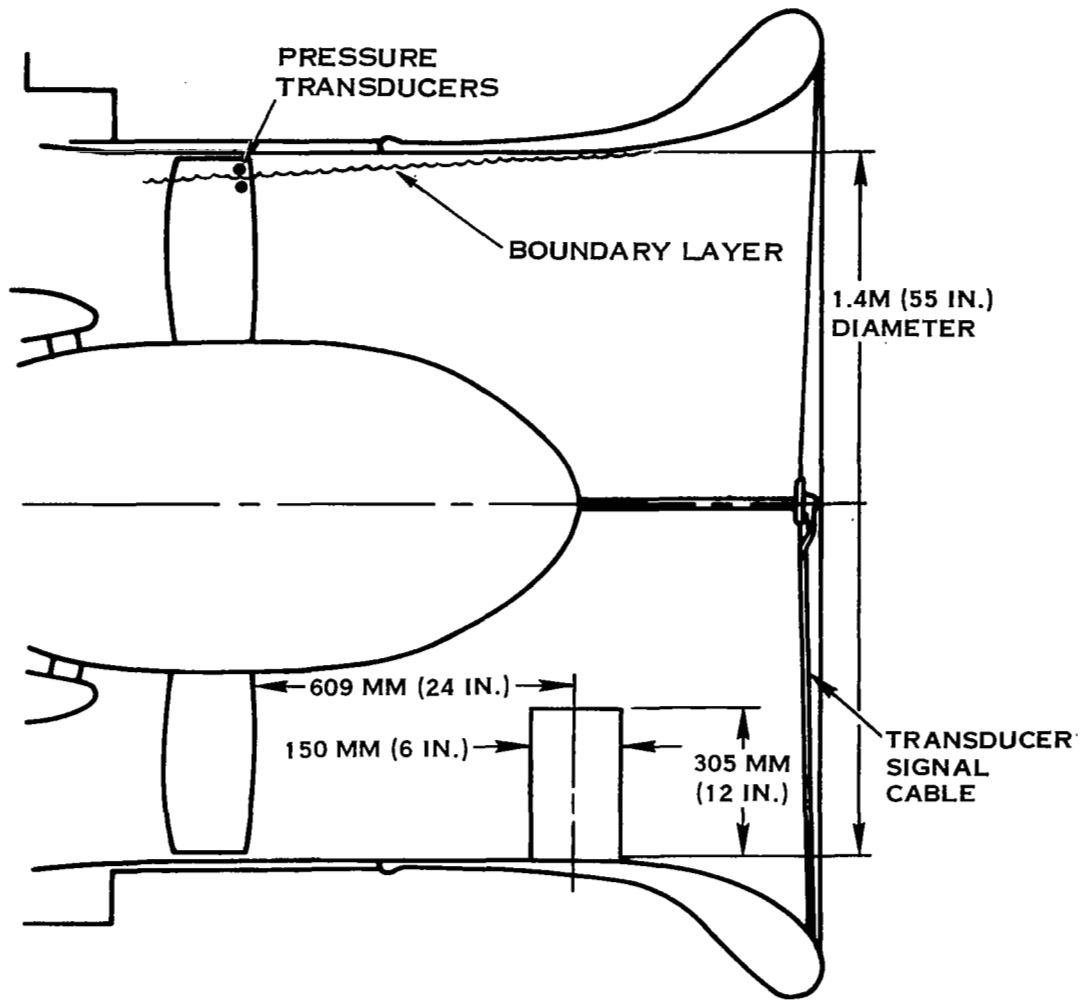
**FIGURE 9. CYLINDRICAL POST CAUSING
WAKE IN ROTOR INFLOW**
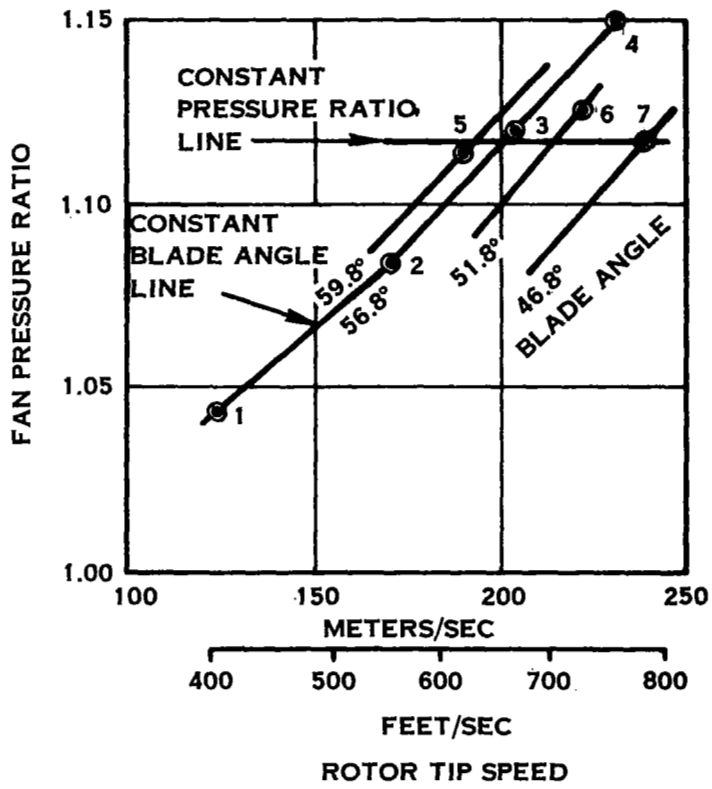
FIGURE 10. FAN TEST POINTS
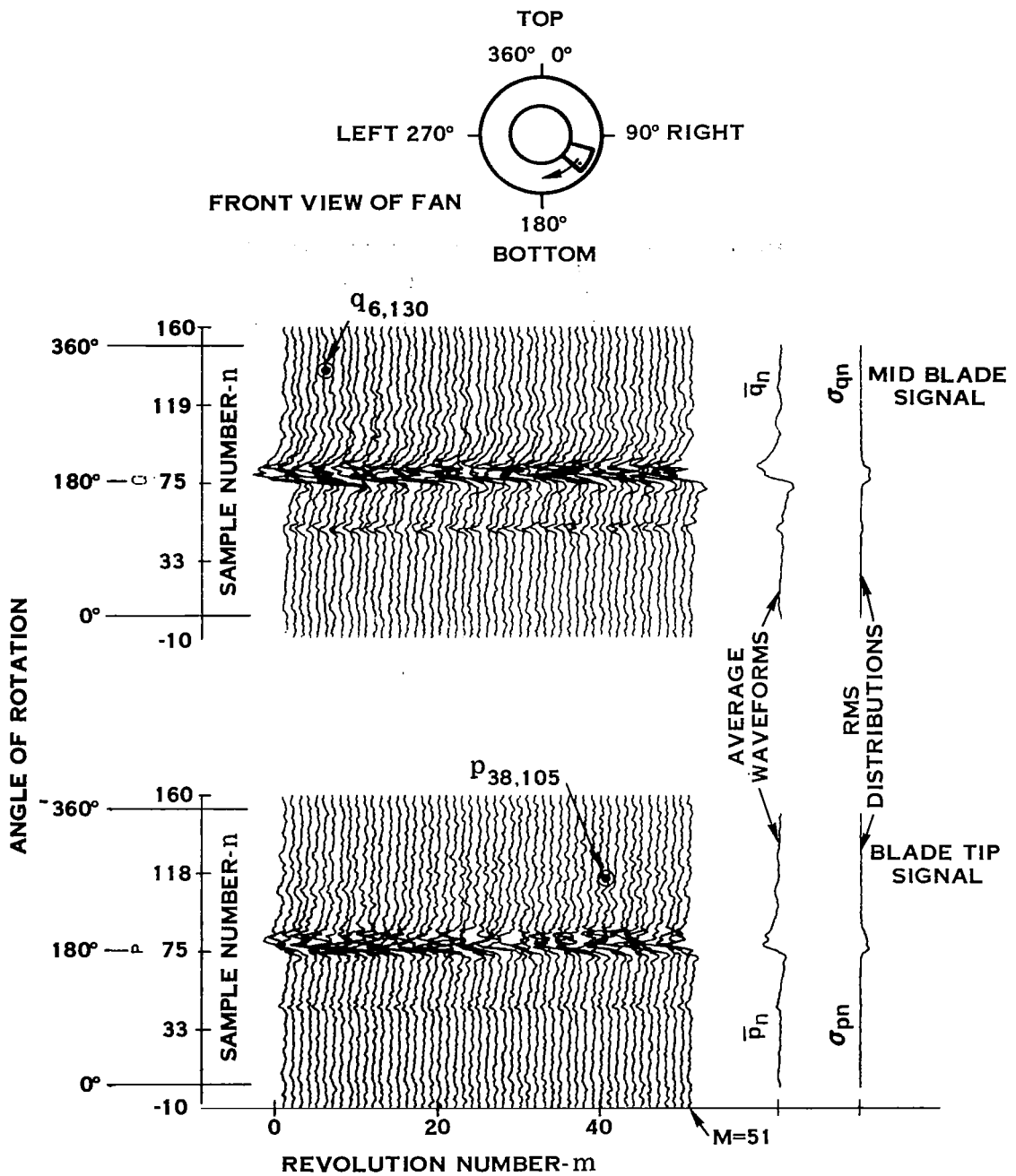
FIGURE 11. KEY TO BLADE PRESSURE WAVEFORM PLOTS
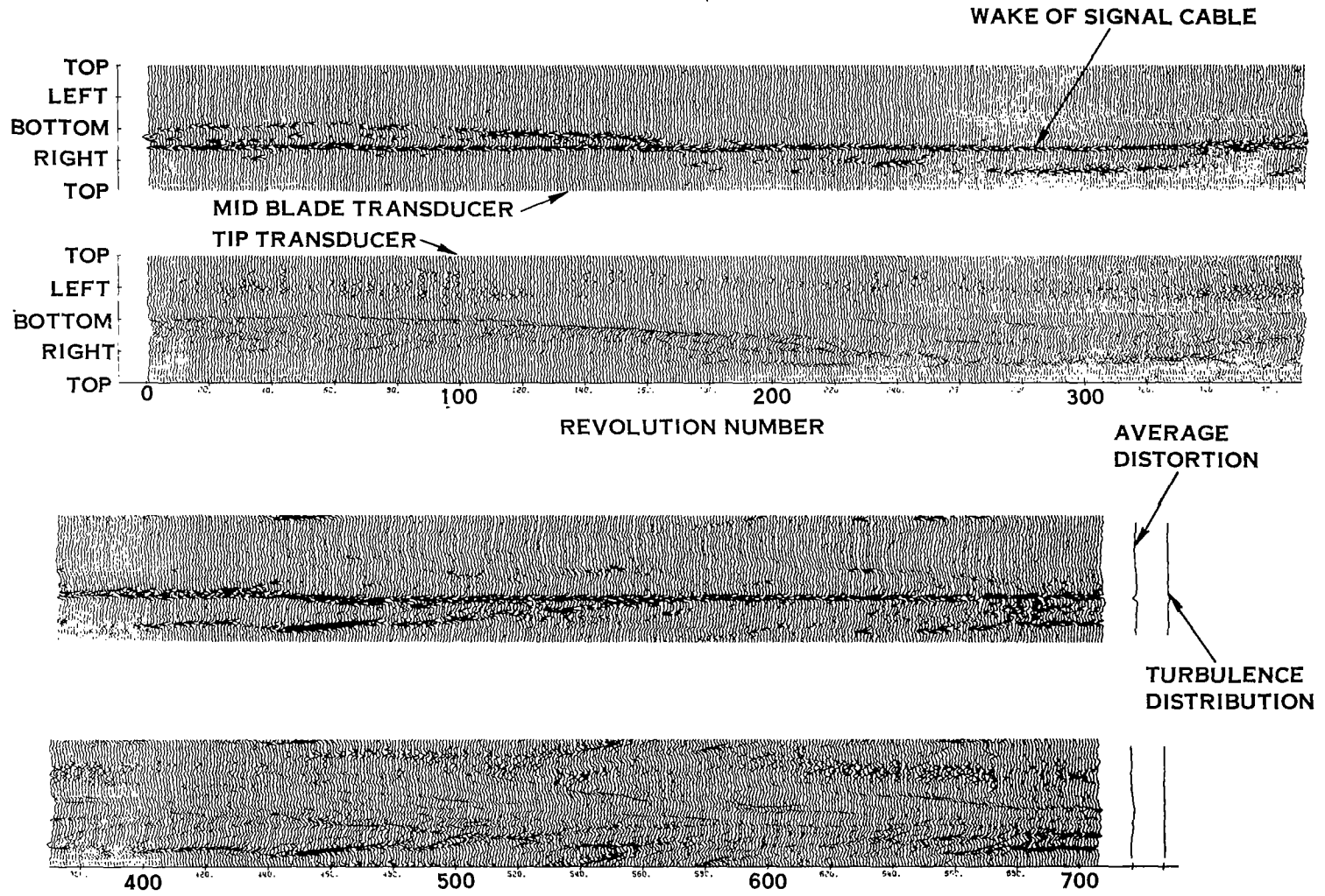
FIGURE 12. INLET DISTORTION SPACE - TIME HISTORY FOR RUN 0 - 4
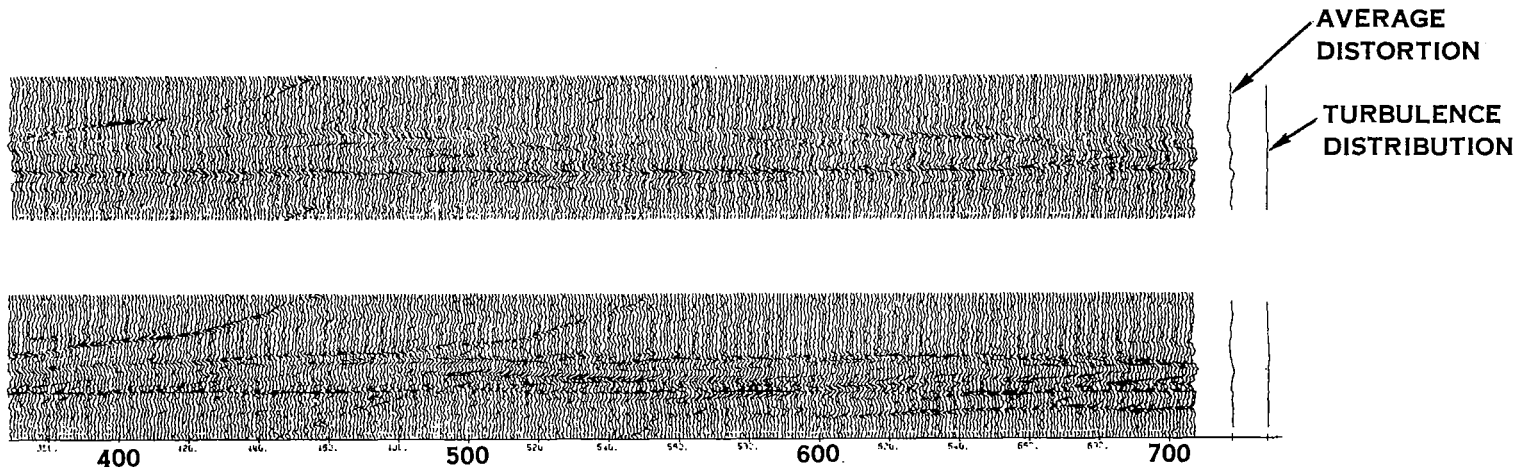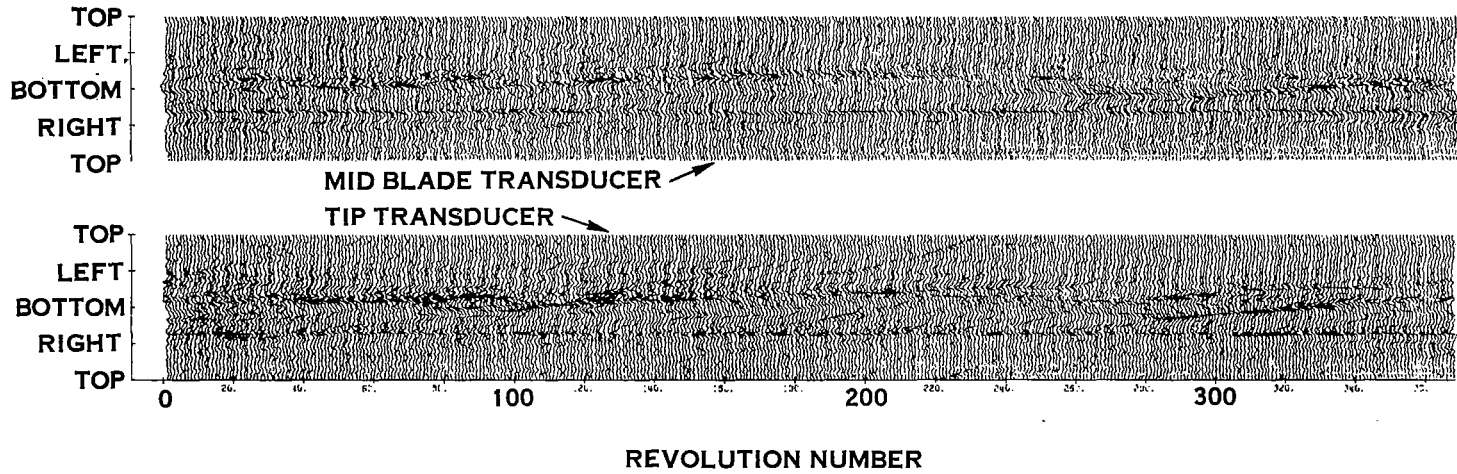
FIGURE 13. INLET DISTORTION SPACE - TIME HISTORY FOR RUN 0 -6

MID BLADE TRANSDUCER

TIP TRANSDUCER
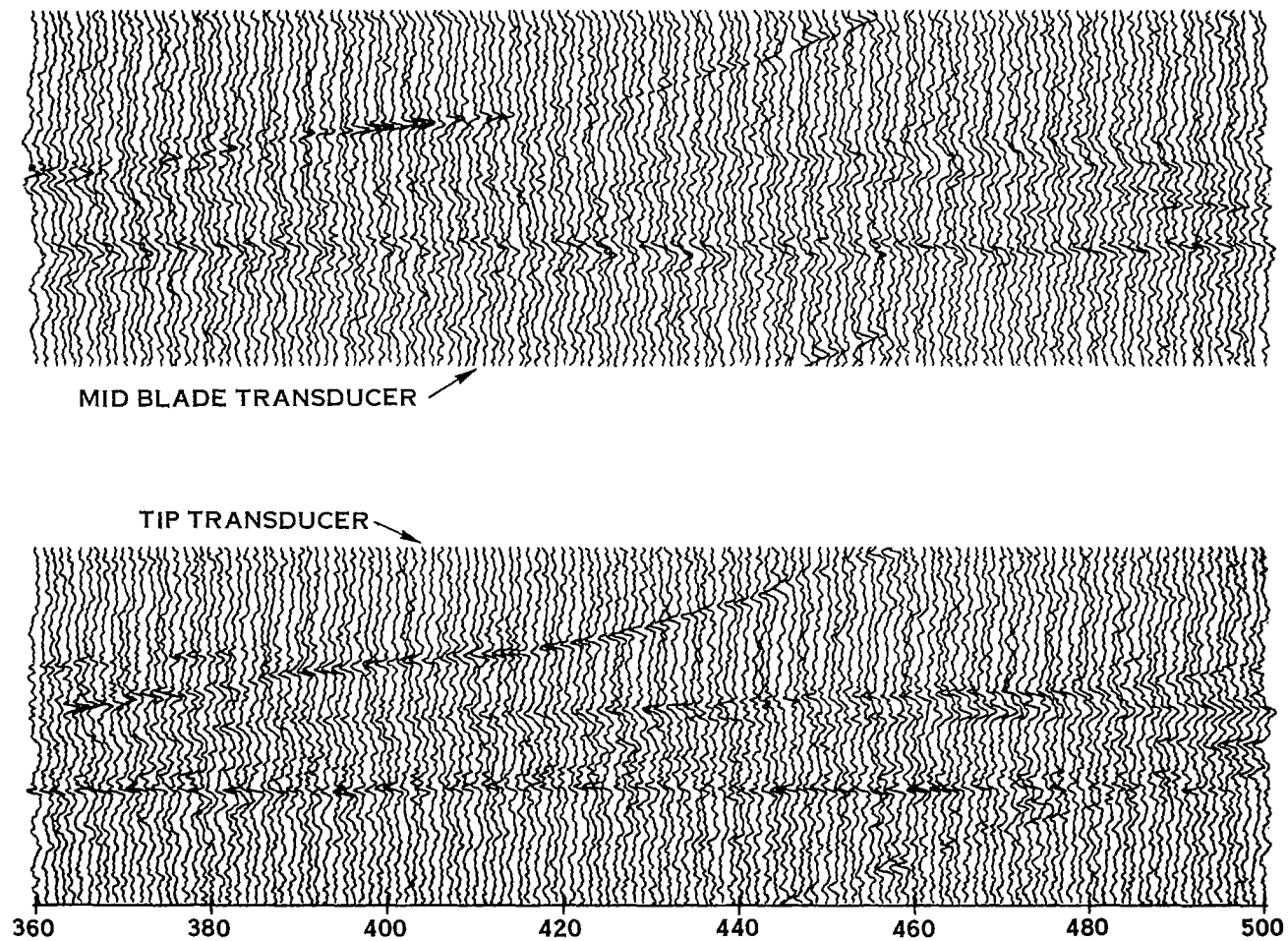
FIGURE 14. EXPANDED VIEW OF PREVIOUS FIGURE SHOWING
CIRCUMFERENTIAL TRACKING OF EDDY
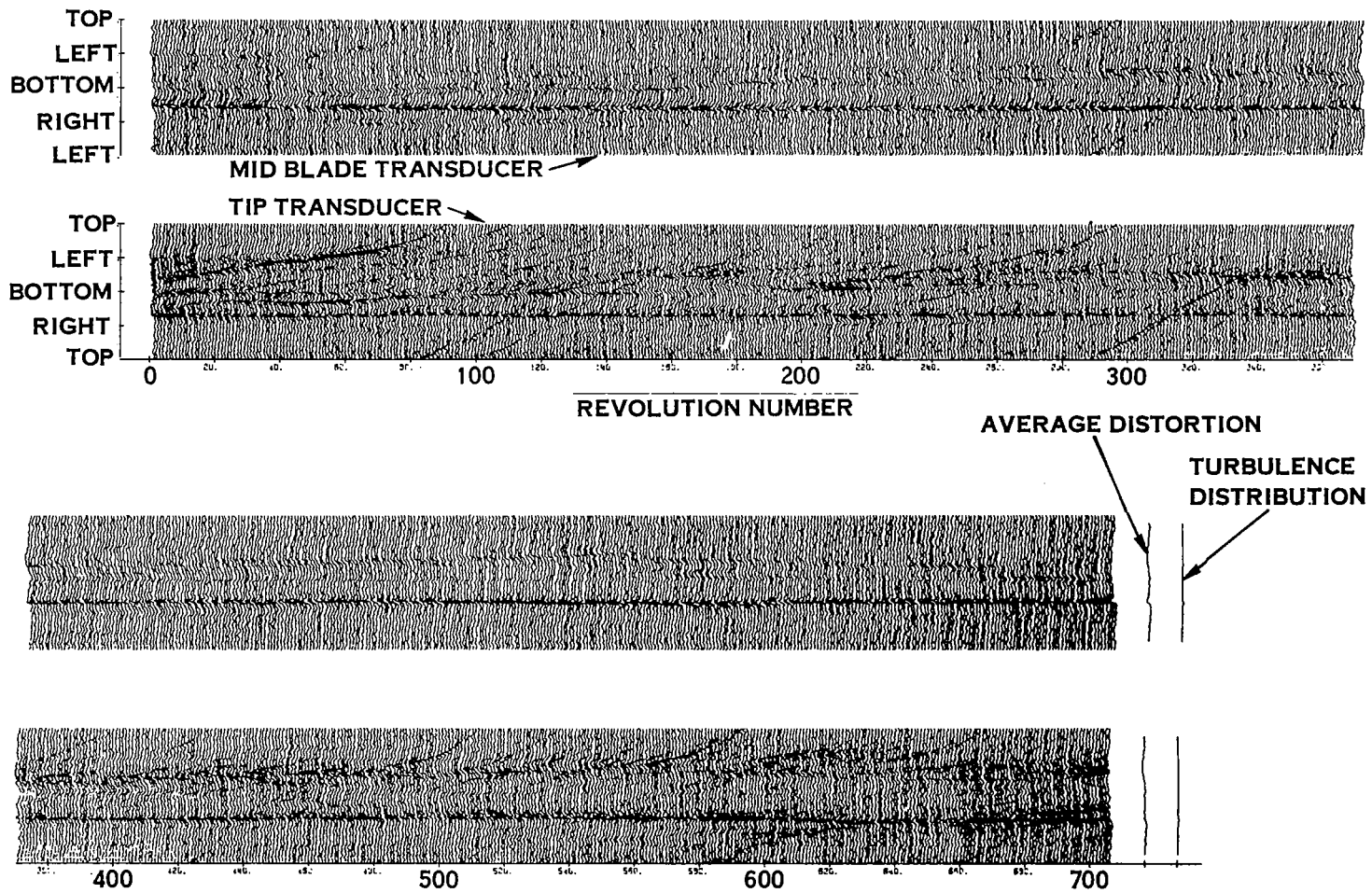
FIGURE 15. INLET DISTORTION SPACE - TIME HISTORY FOR RUN 0 - 5A
(WIND 1 - 3 KNOTS FROM RIGHT)

TOP
LEFT
BOTTOM
RIGHT
TOP

MID BLADE TRANSDUCER

TIP TRANSDUCER

TOP
LEFT
BOTTOM
RIGHT
TOP

0   20.   40.   60.   80.   100   120.   140.   160.   180.   200   220.   240.   260.   280.   300   320.   340.   360.   380.

REVOLUTION NUMBER

AVERAGE
DISTORTION

TURBULENCE
DISTRIBUTION

400   500   600   700
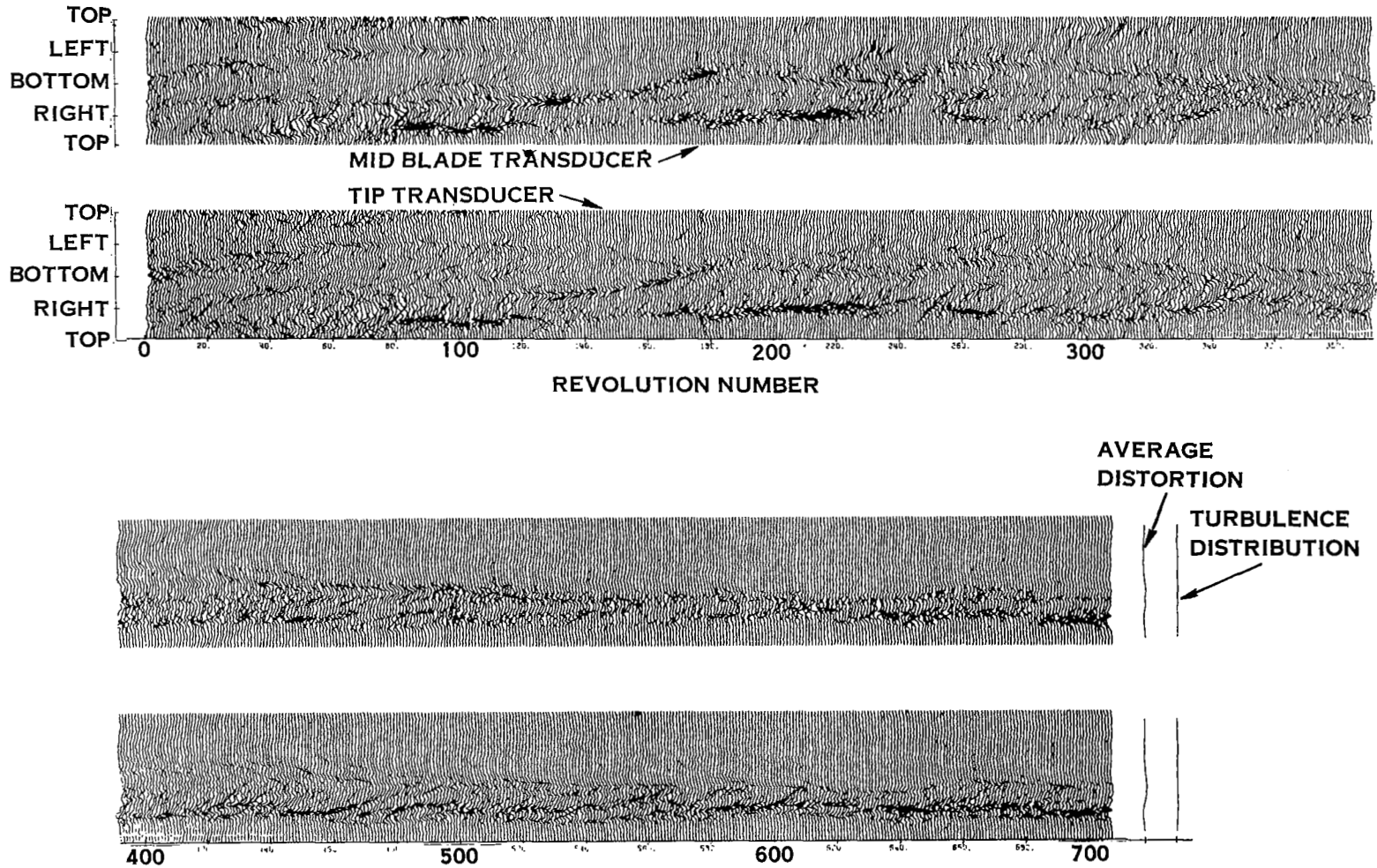
FIGURE 16.   INLET DISTORTION SPACE - TIME HISTORY FOR RUN 0 - 5B
(WIND 10 - 16 KNOTS FROM RIGHT)
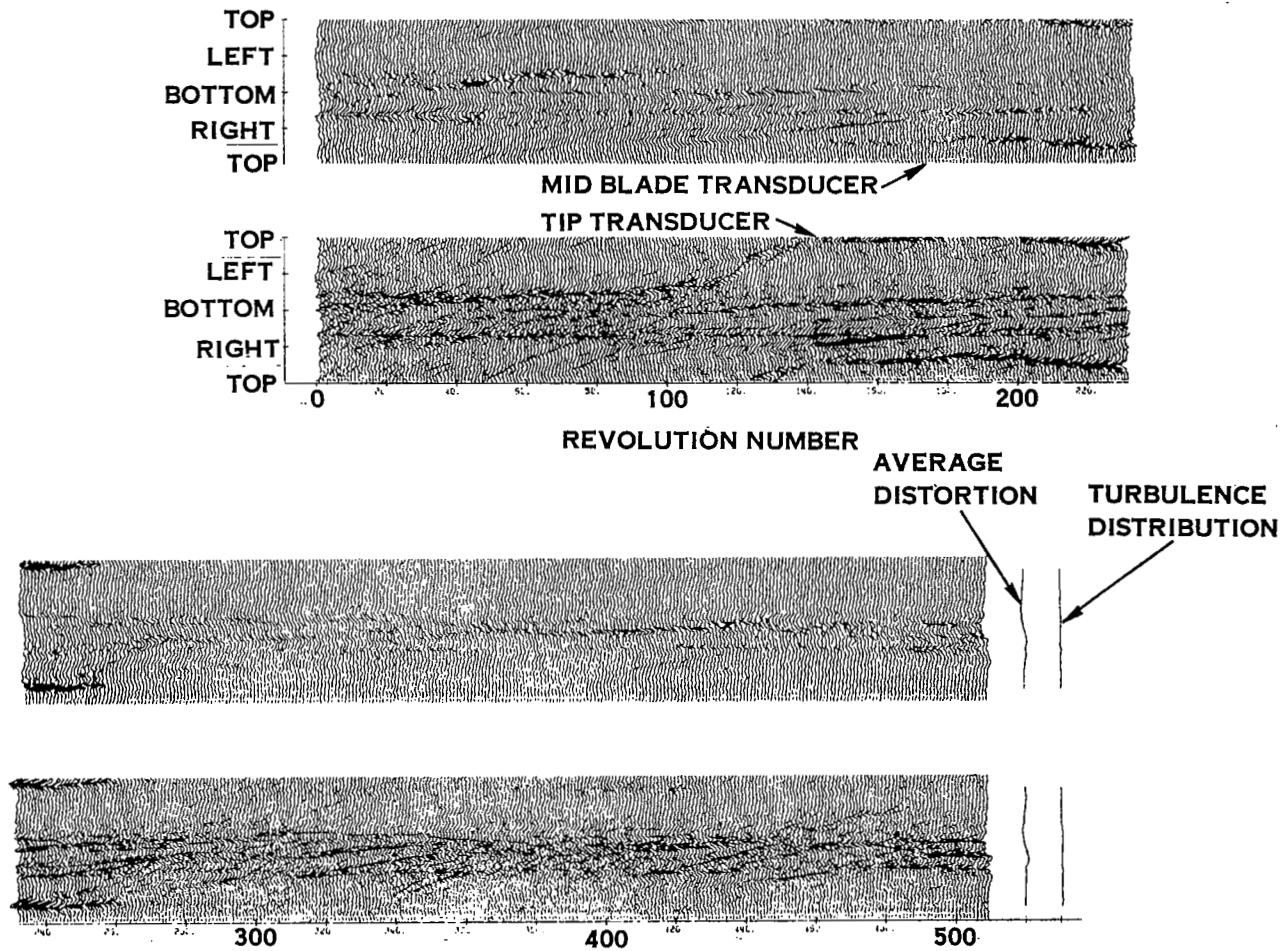
FIGURE 17. INLET DISTORTION SPACE - TIME HISTORY FOR RUN 0 - 1
(LOW WIND SPEED , LOW RPM CASE).

200.   220.   240.   260.
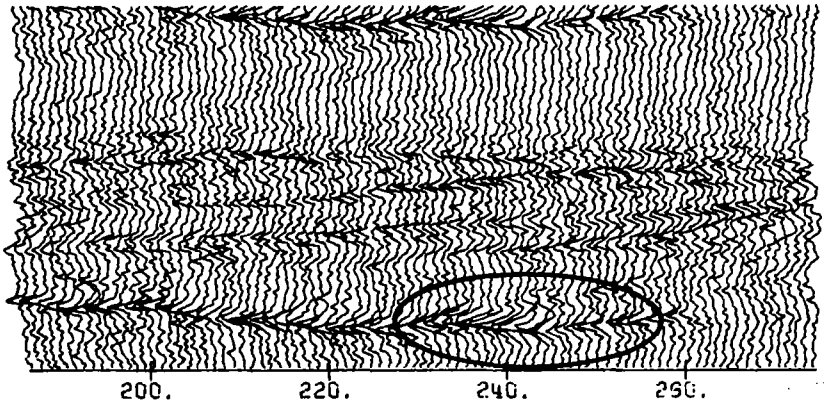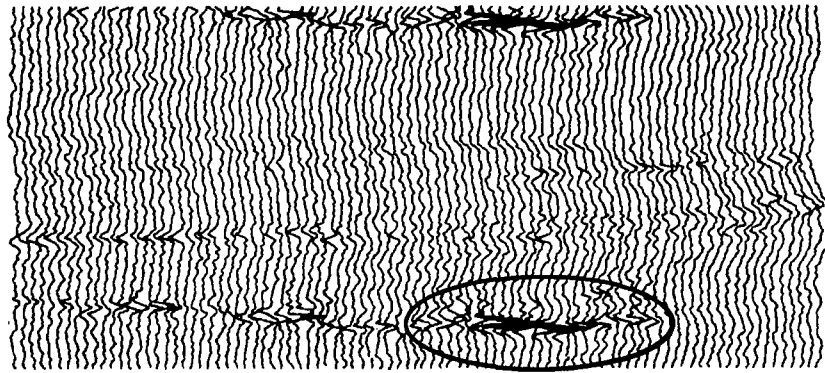
FIGURE 18. EXPANDED VIEW FROM PRECEEDING FIGURE SHOWING
BLADE RESPONSE WITH OPPOSITE SIGNS
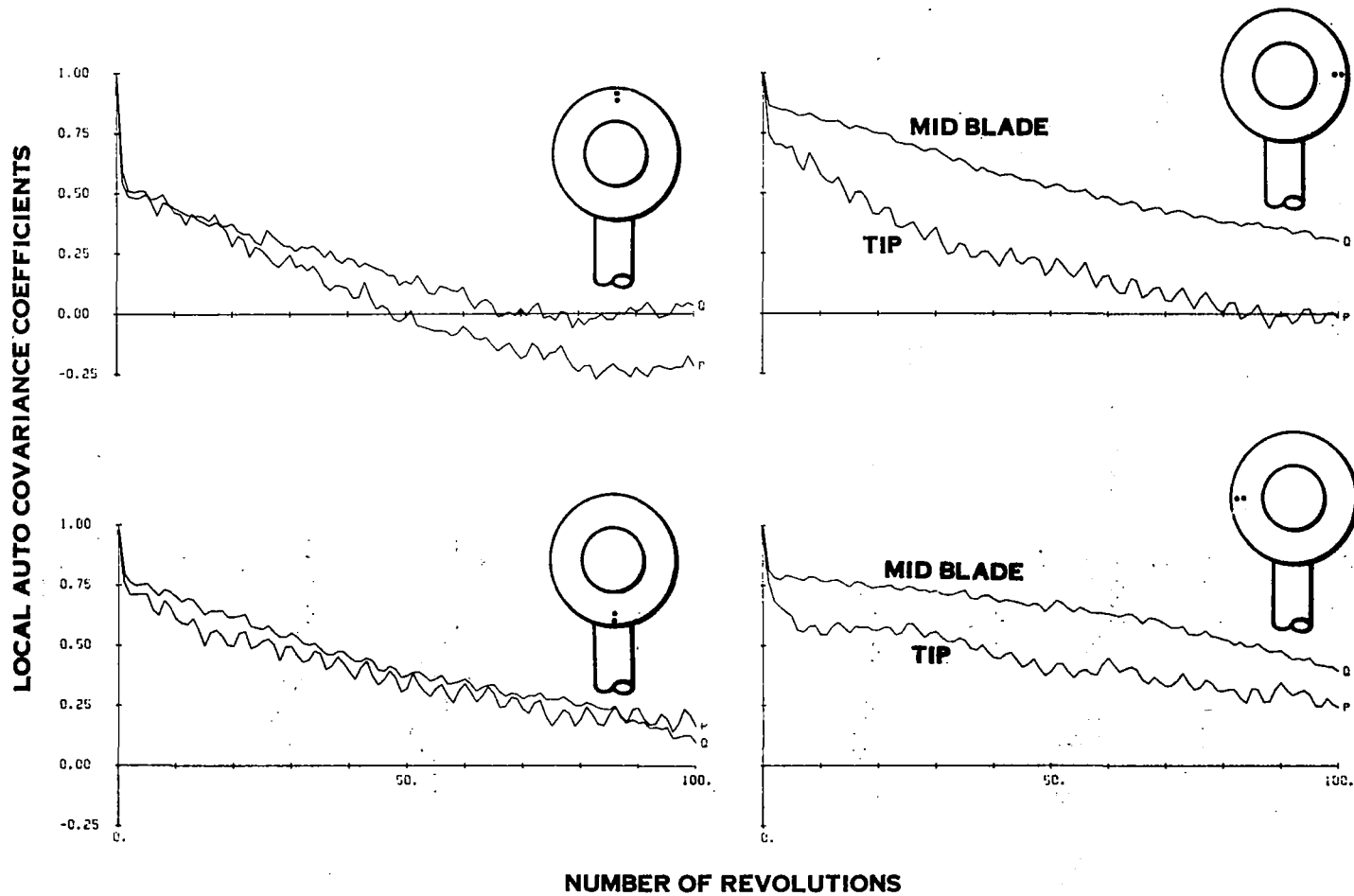
FIGURE 19. STREAMWISE CORRELATIONS MEASURED AT FOUR LOCATIONS IN
INLET FOR RUN 0 - 5A (1 - 3 KNOT WIND FROM RIGHT)
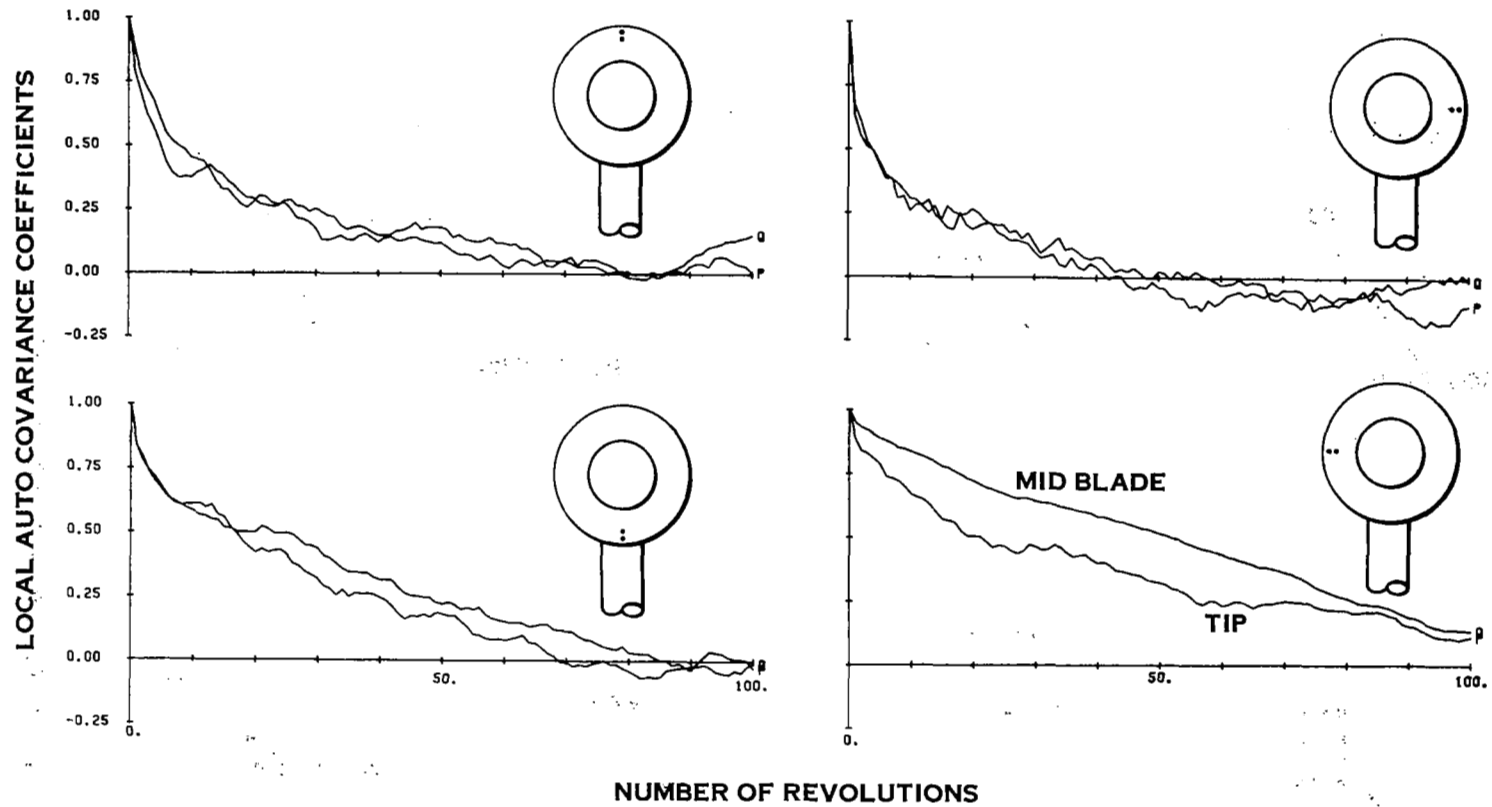
FIGURE 20. STREAM WISE CORRELATIONS MEASURED AT FOUR LOCATIONS IN
INLET FOR RUN 0 - 5B (10 - 16 KNOT WIND FROM RIGHT)
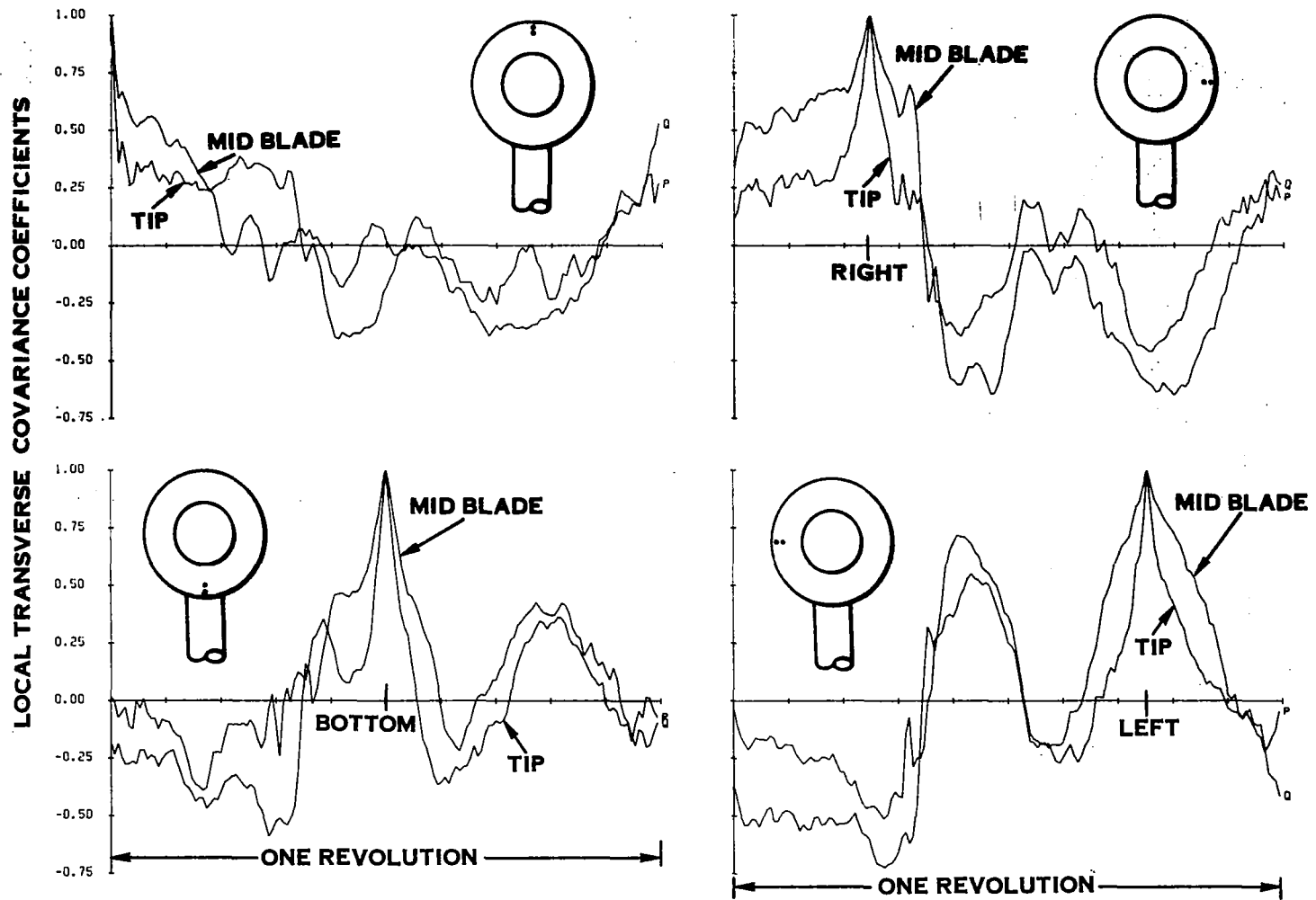
FIGURE 21 TRANSVERSE CORRELATIONS MEASURED AT FOUR LOCATIONS
IN INLET FOR RUN 0—5A (1—3 KNOT WIND FROM RIGHT)
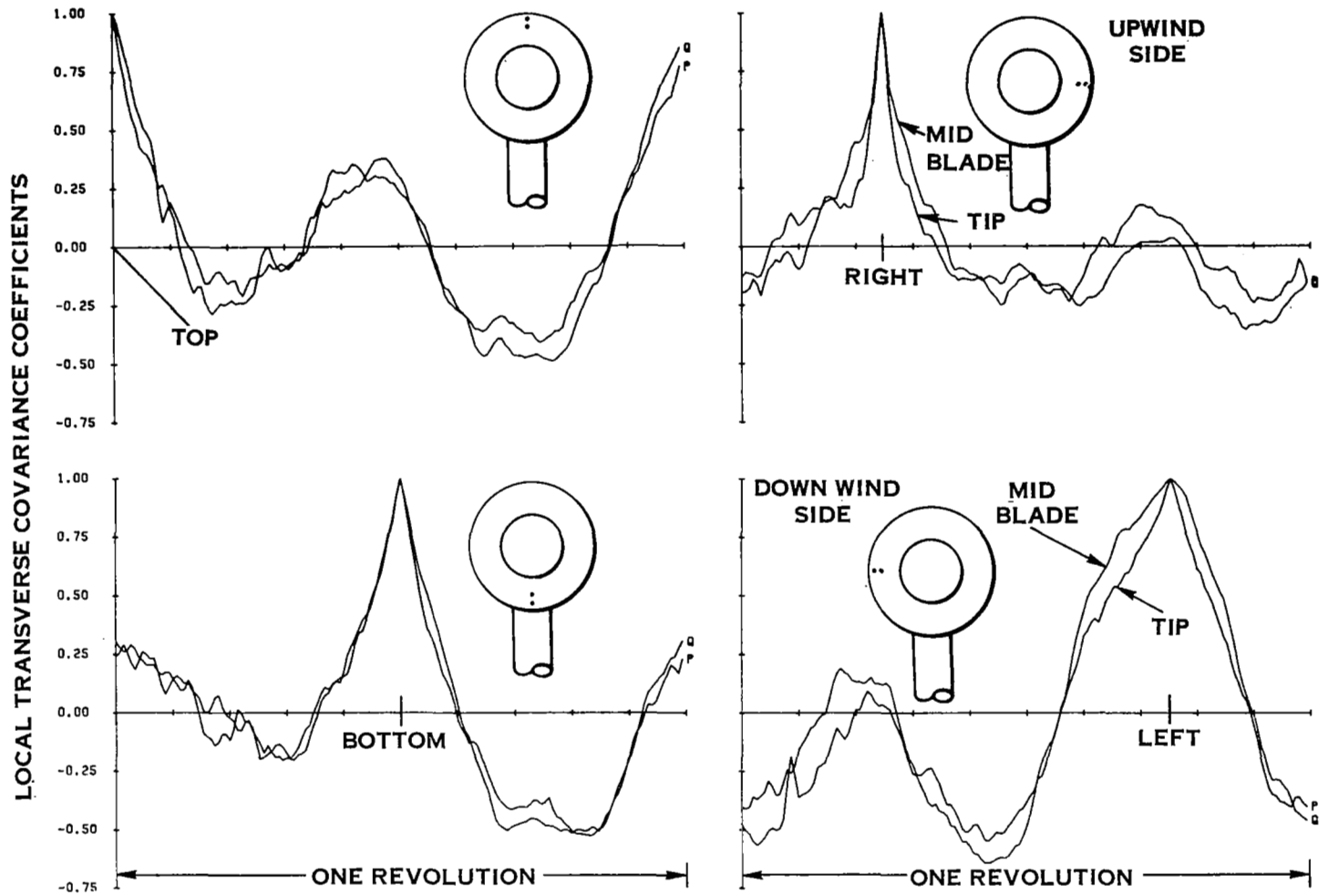
FIGURE 22. TRANSVERSE CORRELATIONS MEASURED AT FOUR LOCATIONS
IN INLET FOR RUN 0– 5B (10 – 16 KNOT WIND FROM RIGHT)
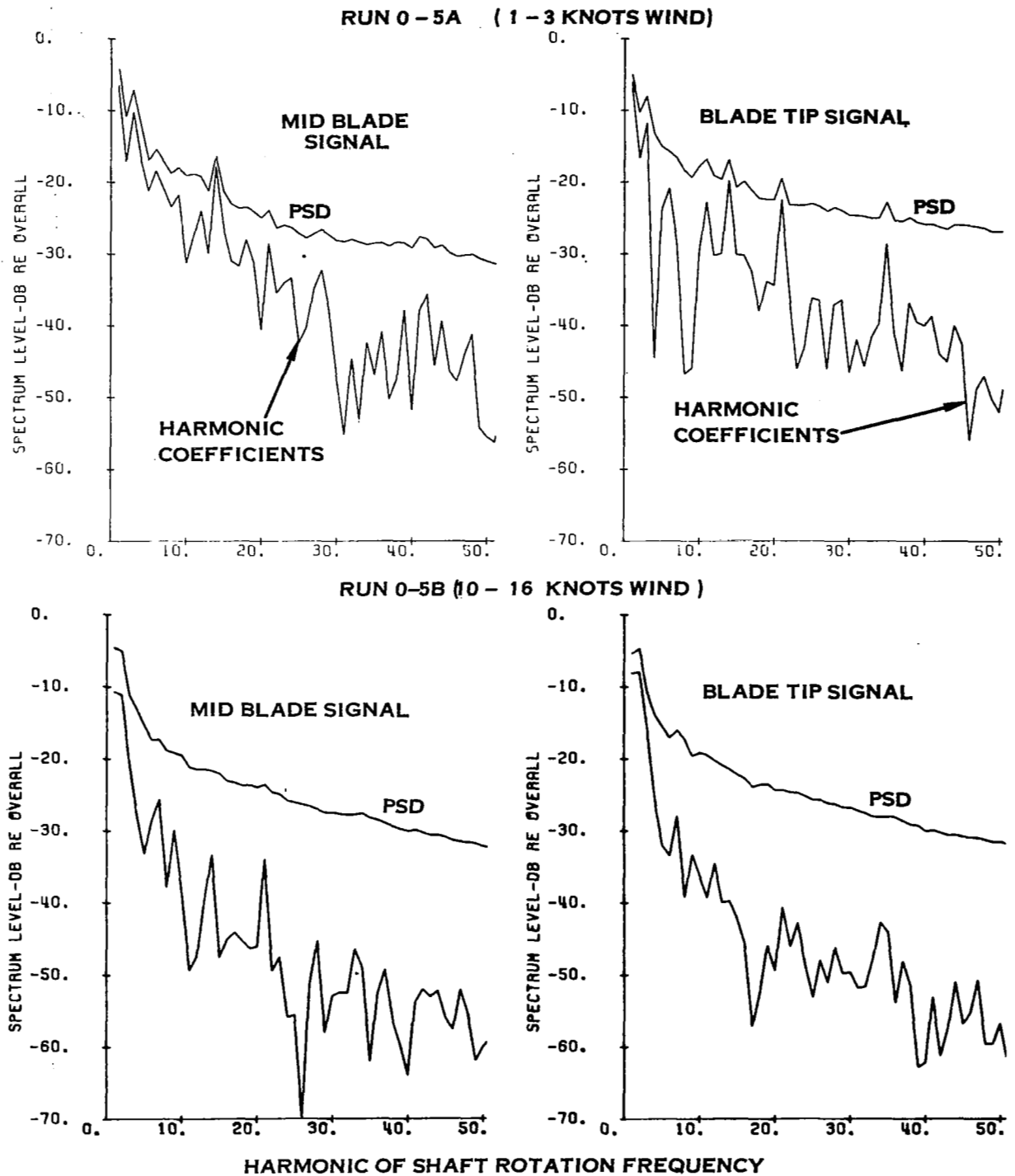
FIGURE 23. SPECTRA OF OVERALL POWER AND HARMONIC COMPONENT COMPARED FOR TIP AND MID BLADE FLOW AND FOR HIGH AND LOW WIND

85
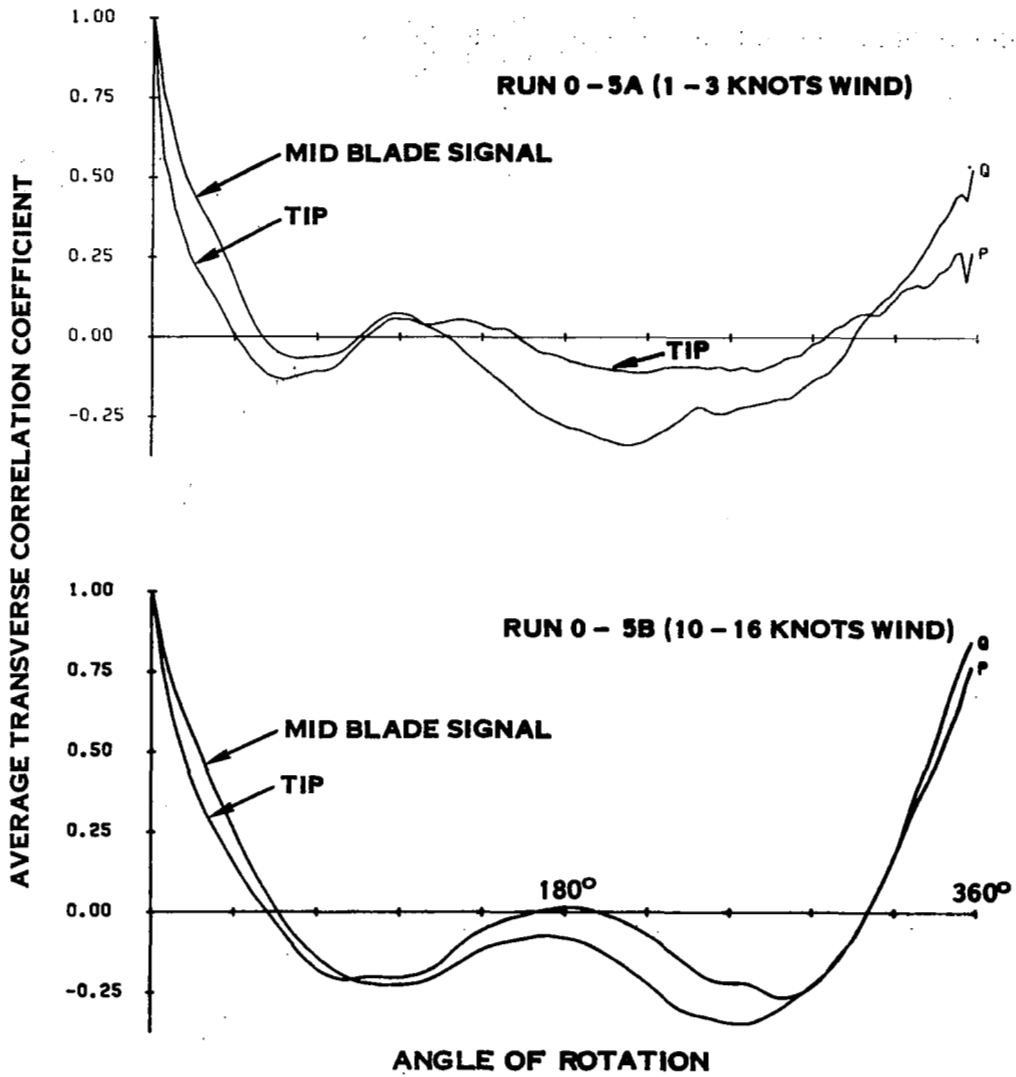
FIGURE 24. AVERAGE TRANSVERSE CORRELATION COEFFICIENTS COMPARED FOR TWO WIND CONDITIONS
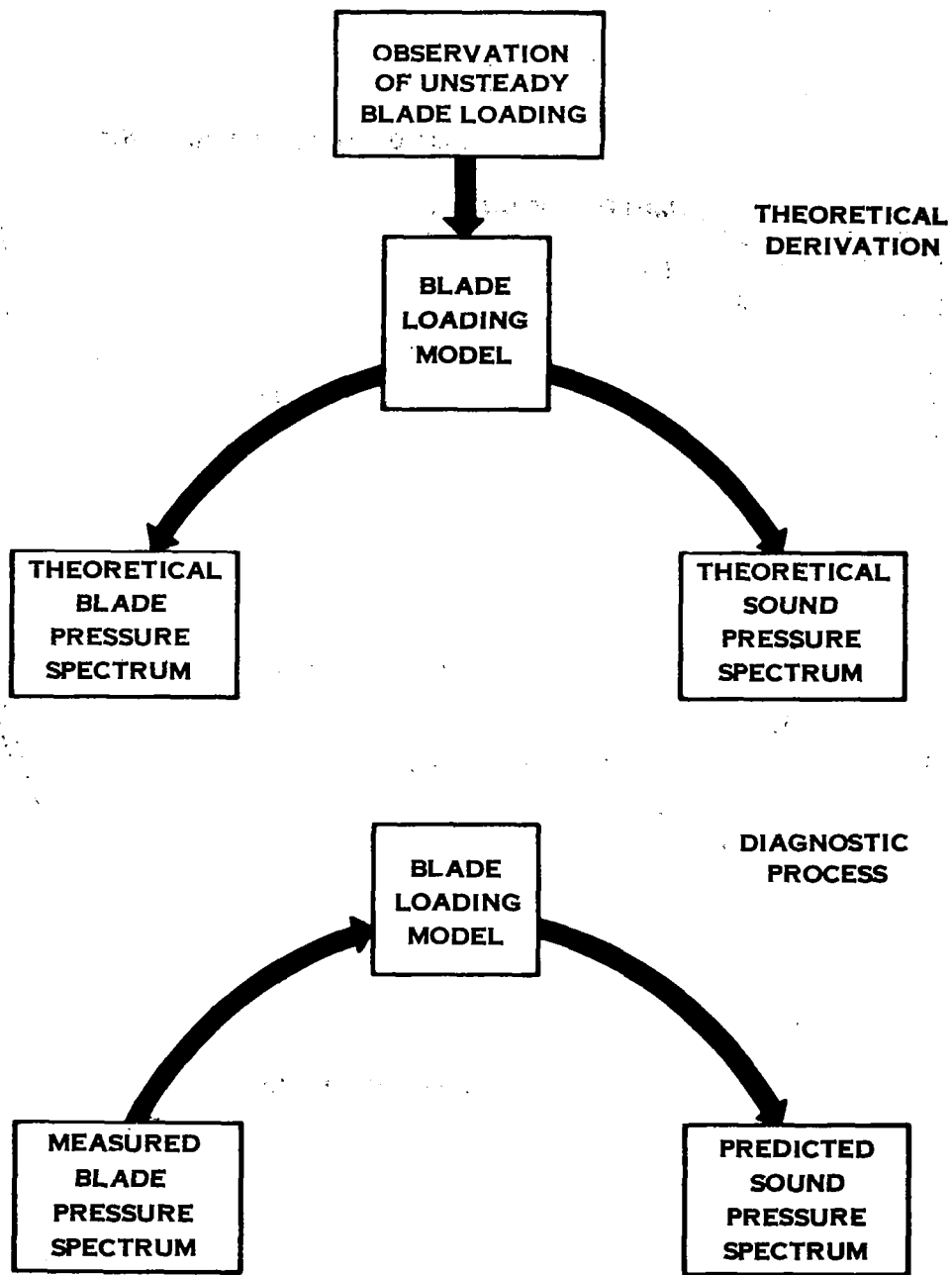
FIGURE 25. EVOLUTION OF ROTOR NOISE DIAGNOSTIC TOOL
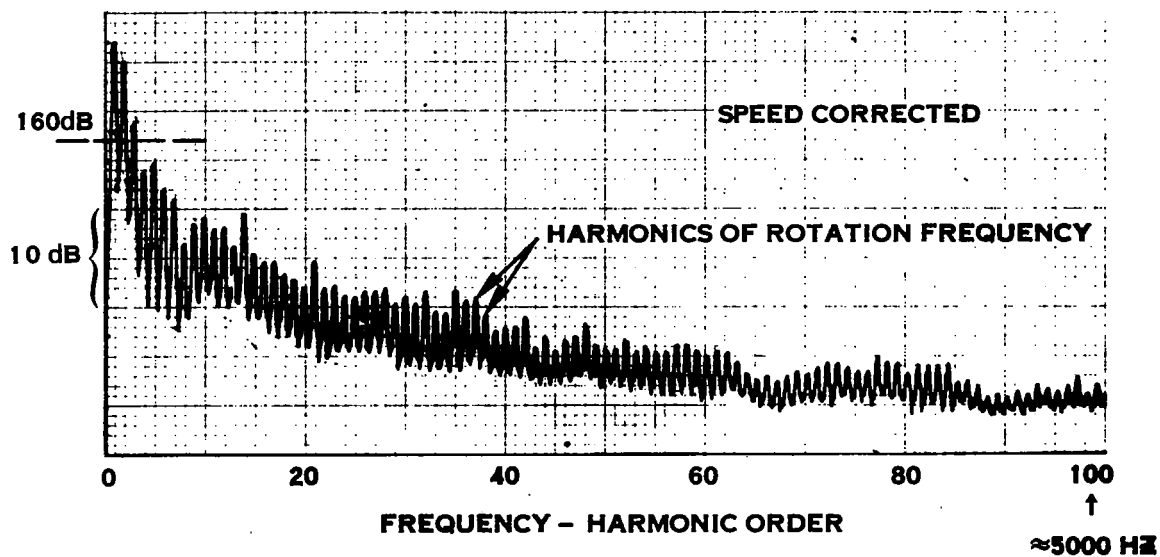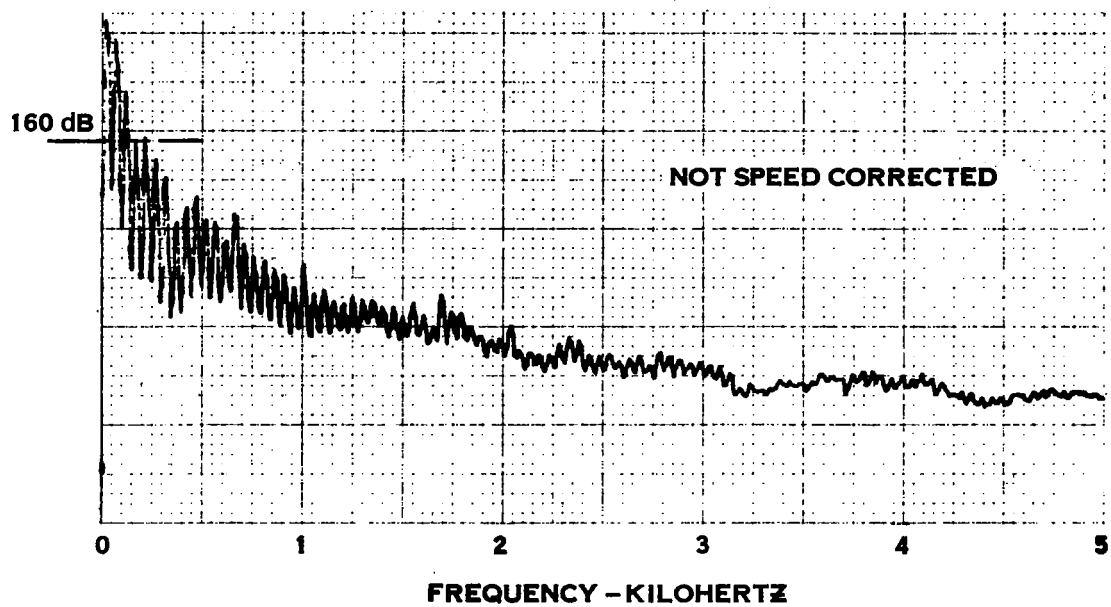
FIGURE 26. EFFECT OF DRIFTING RPM ON BLADE PRESSURE SPECTRUM

TIP LOCATION

BLADE PRESSURE SPECTRA

150

140 dB

140

130

8 HZ BANDWIDTH BPL — dB

120

MID BLADE LOCATION

150

140 dB

140

130

120

100

0

50

HARMONIC OF SHAFT ROTATION FREQUENCY

BLADE PASSING FREQUENCY

SOUND PRESSURE SPECTRUM

100 dB

100

90

MIC ON AXIS AT 7.62 M (25 FT.)

80

17 HZ BANDWIDTH SPL — dB

70

200

0

100

HARMONIC OF SHAFT ROTATION FREQUENCY
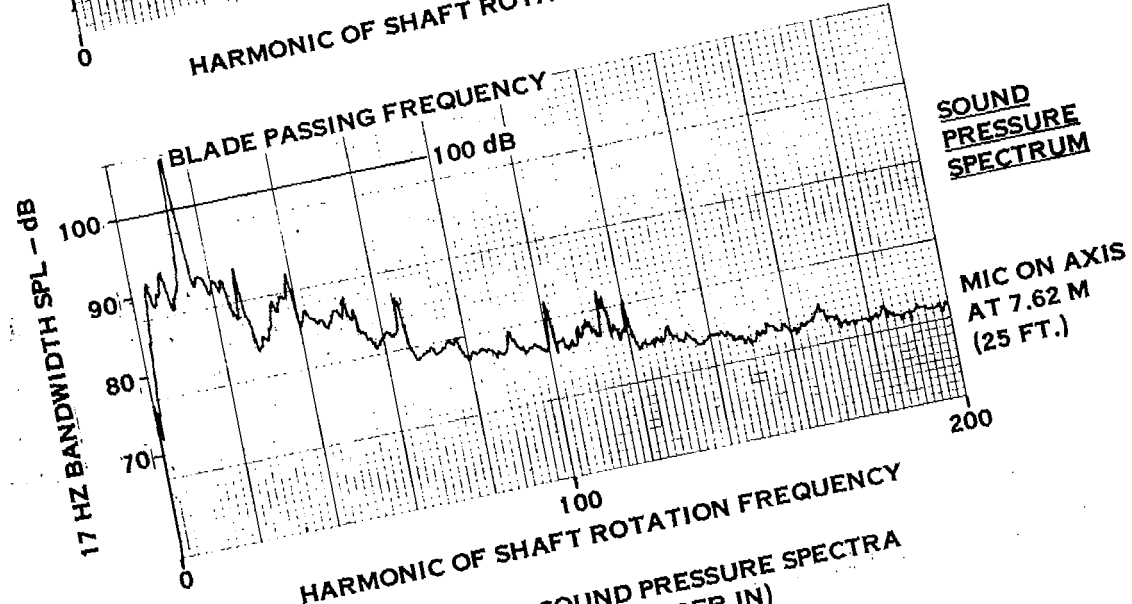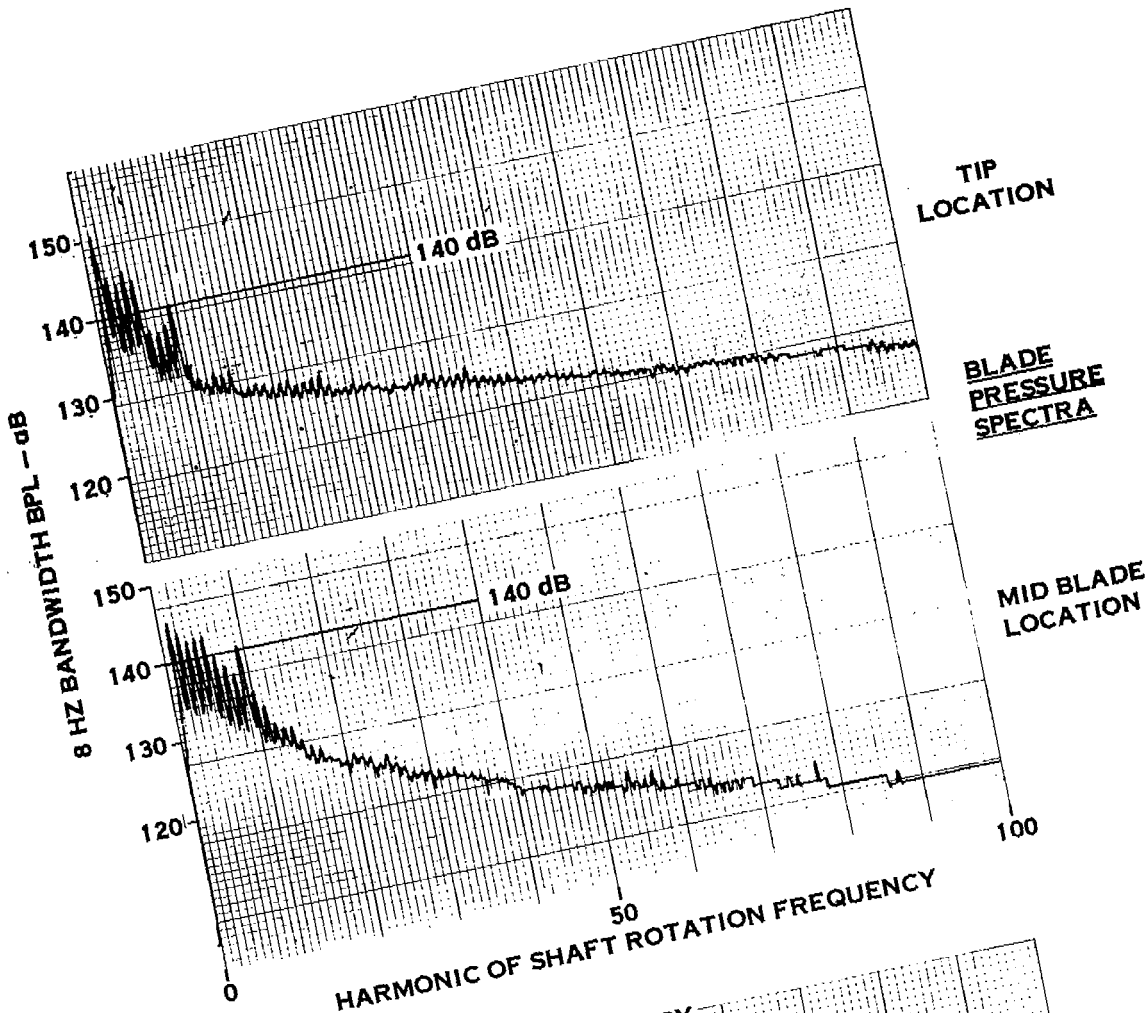
FIGURE 27 BLADE AND SOUND PRESSURE SPECTRA CONDITION I-1 (CYLINDER IN)
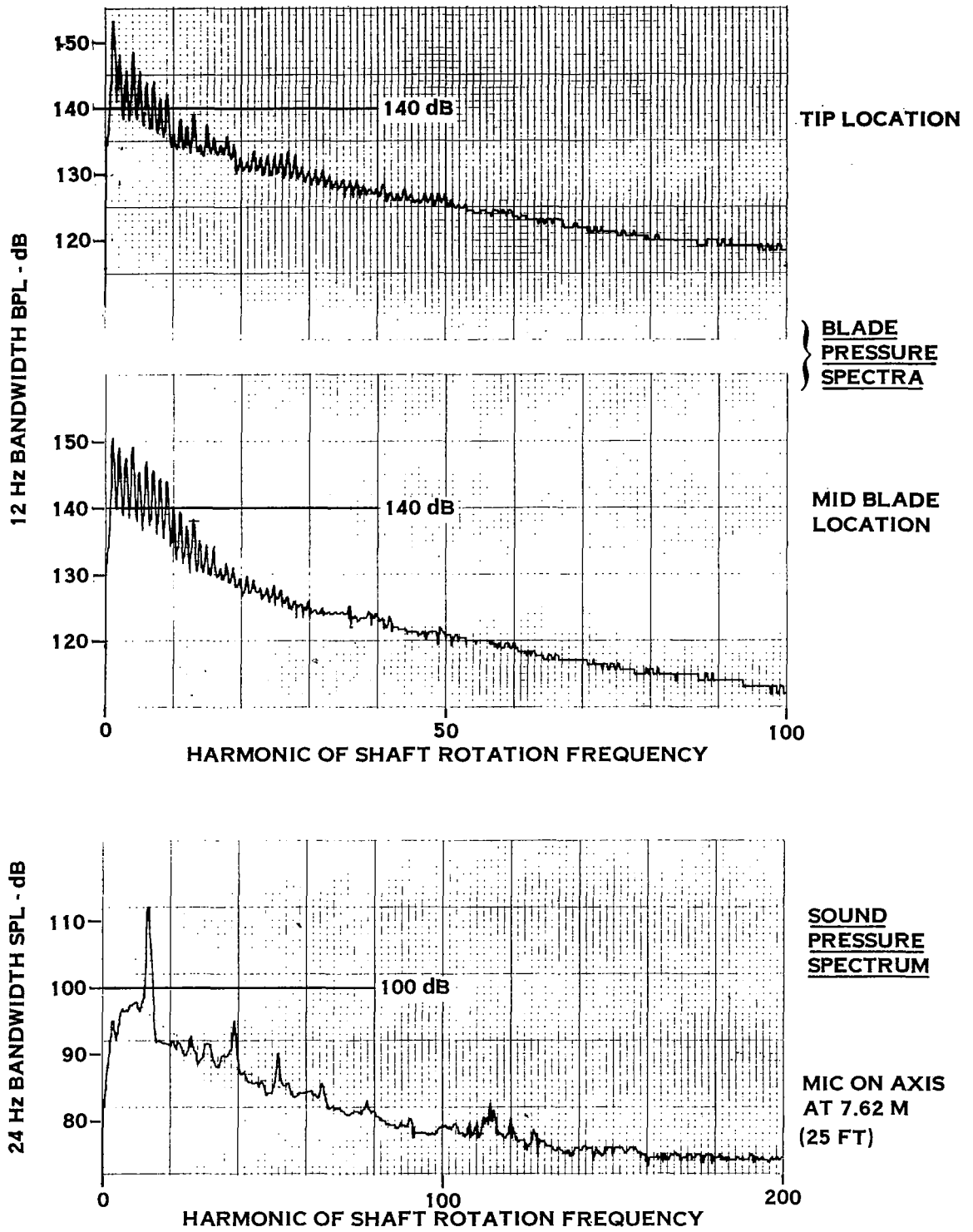
FIGURE 28   BLADE AND SOUND PRESSURE SPECTRA
CONDITON I—2 (CYLINDER IN)
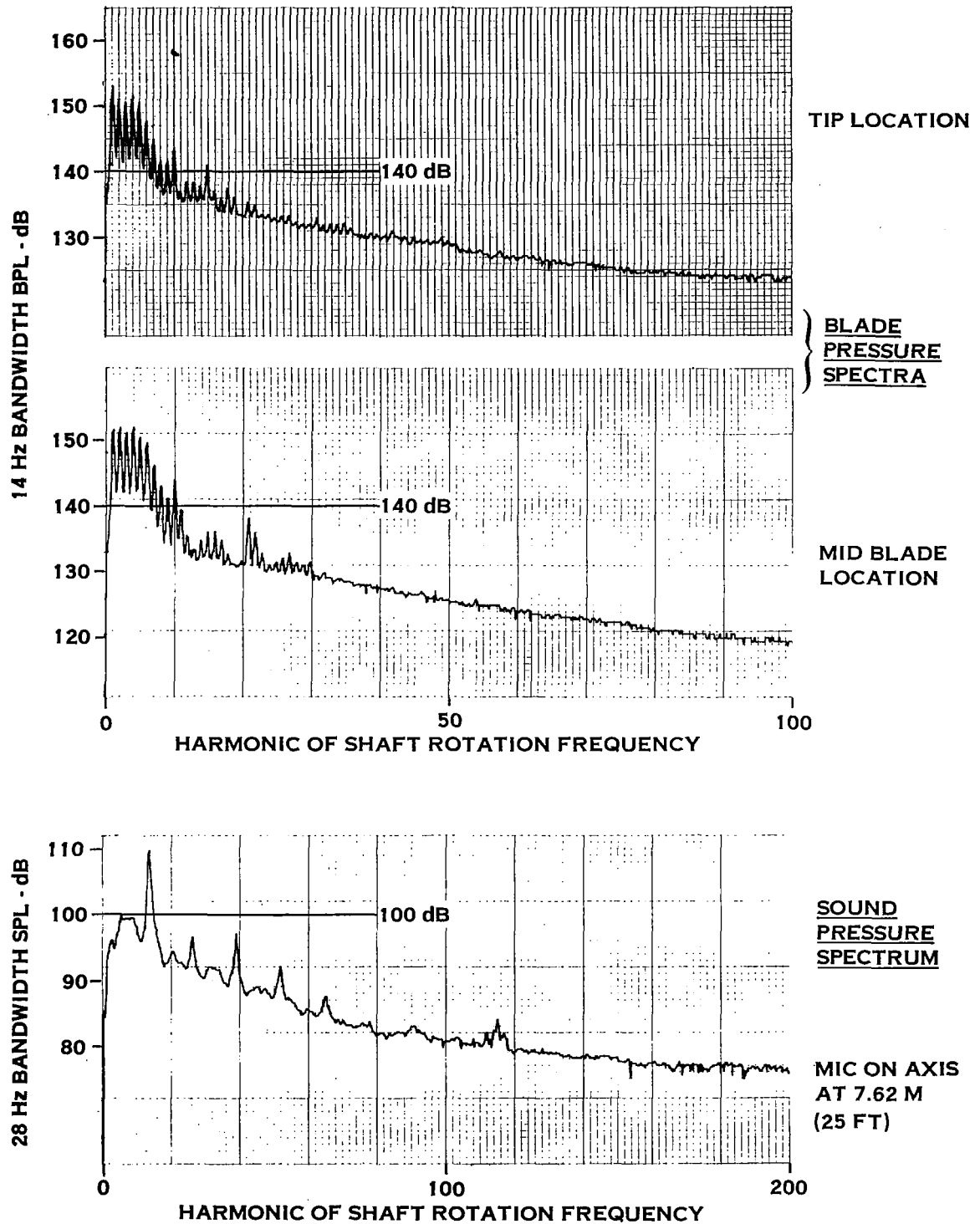
**FIGURE 29   BLADE AND SOUND PRESSURE SPECTRA
TEST CONDITION I-3 (CYLINDER IN)**
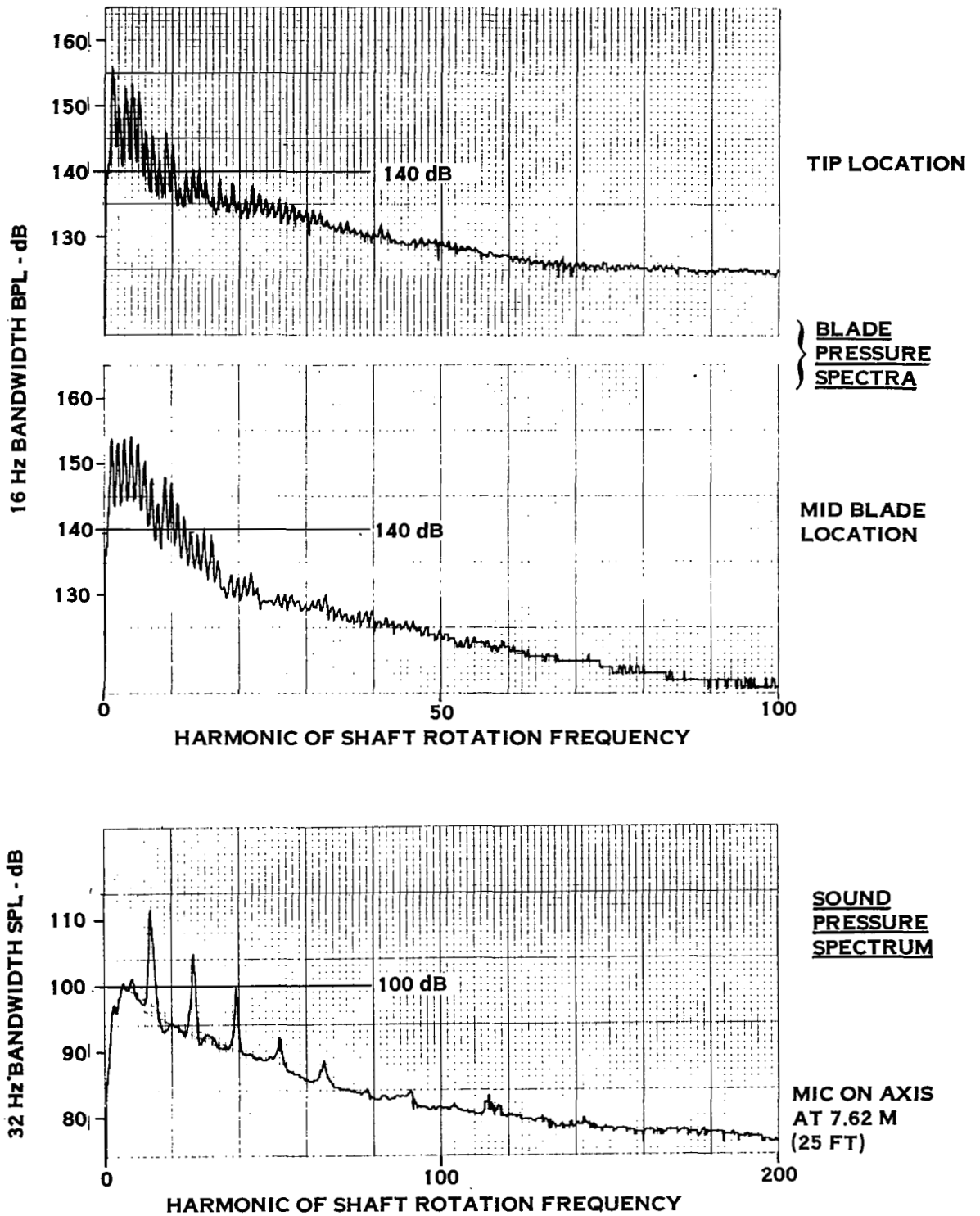
FIGURE 30. BLADE AND SOUND PRESSURE SPECTRA
CONDITION 1–4 (CYLINDER IN)
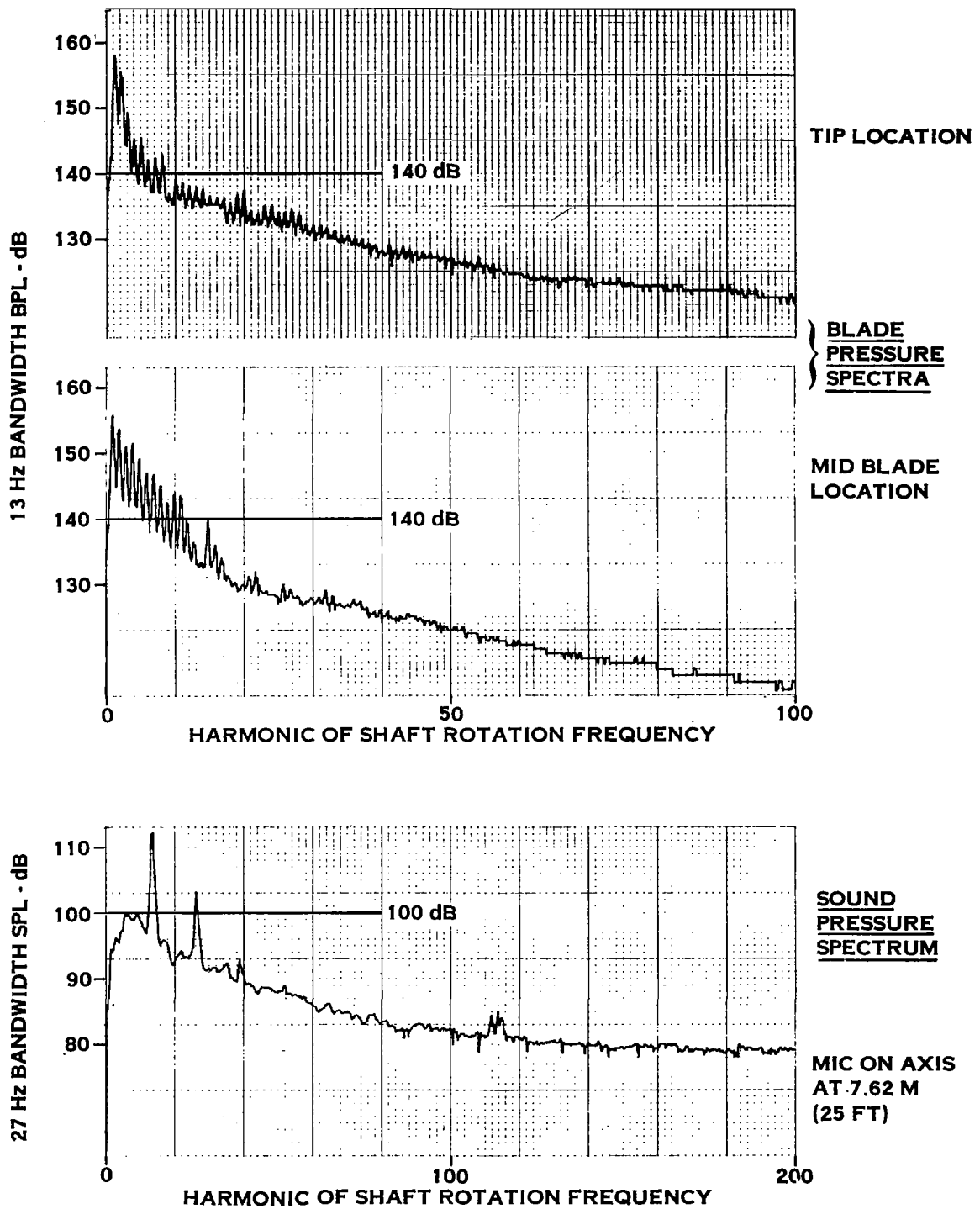
FIGURE 31   BLADE AND SOUND PRESSURE SPECTRA
CONDITION I—5 (CYLINDER IN)
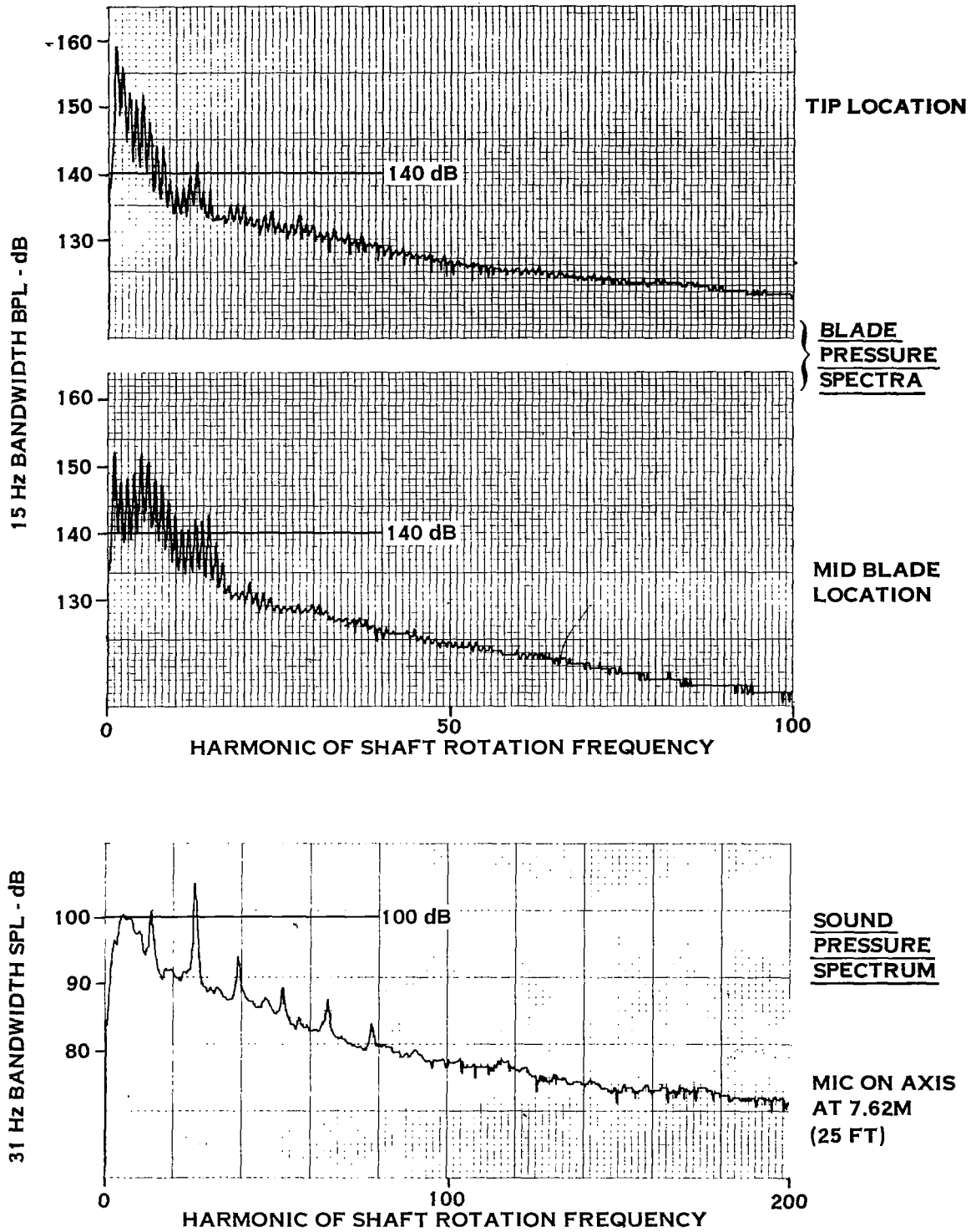
FIGURE 32. BLADE AND SOUND PRESSURE SPECTRA
CONDITION I—6 (CYLINDER IN)

94
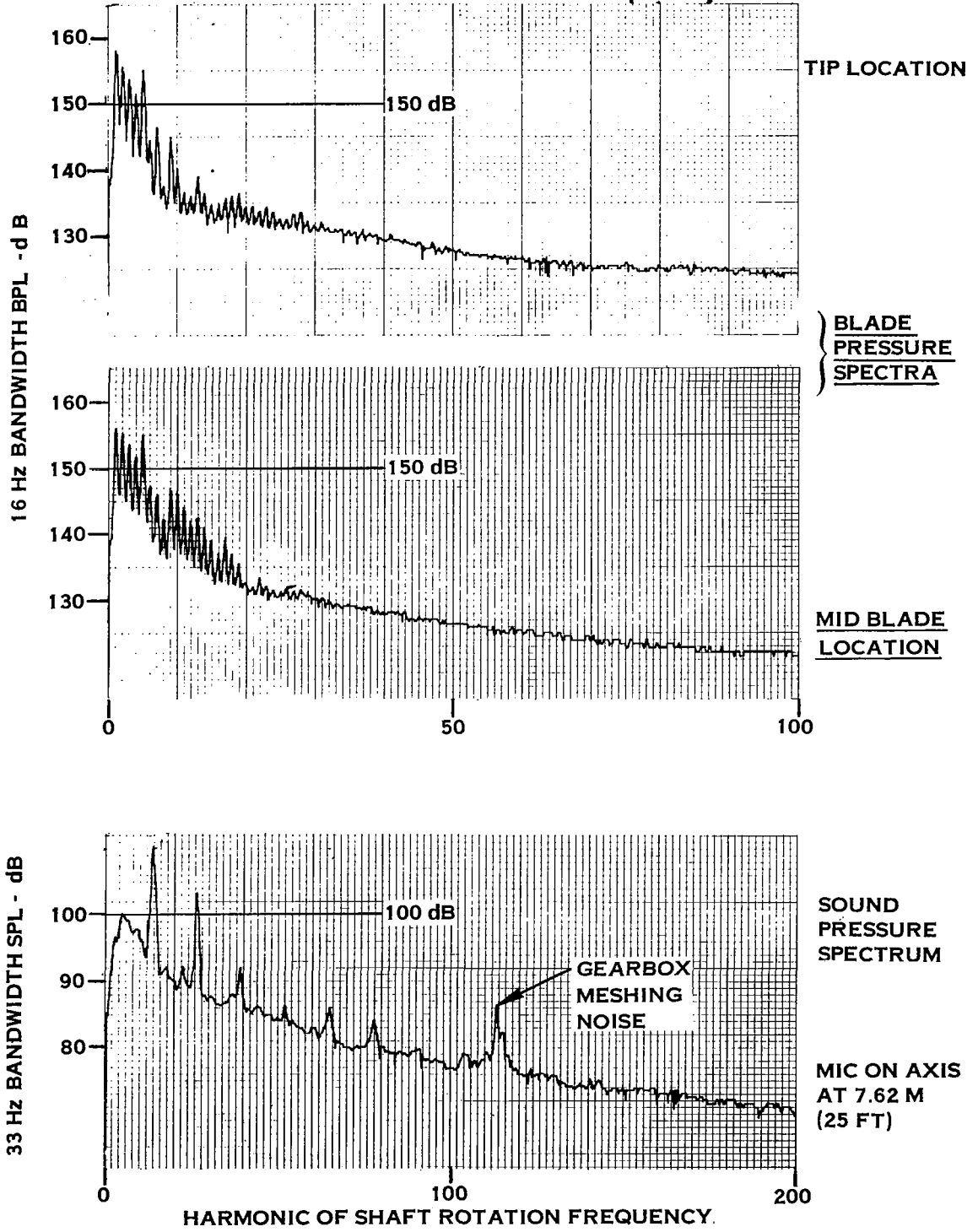
FIGURE 33   BLADE AND SOUND PRESSURE SPECTRA
CONDITION I—7 (CYLINDER IN)

95
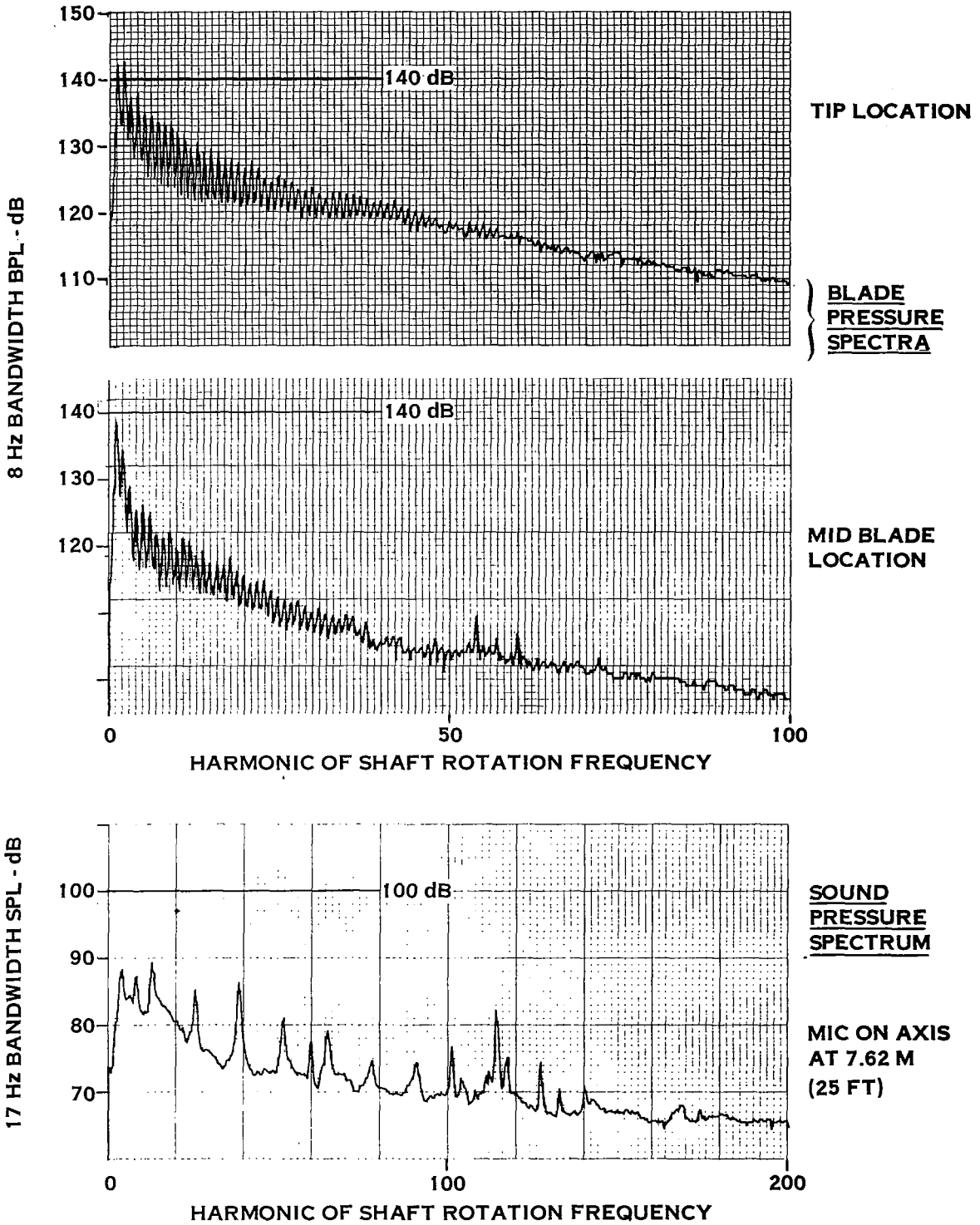
FIGURE 34. BLADE AND SOUND PRESSURE SPECTRA
CONDITION O—1 (CYLINDER OUT)

96
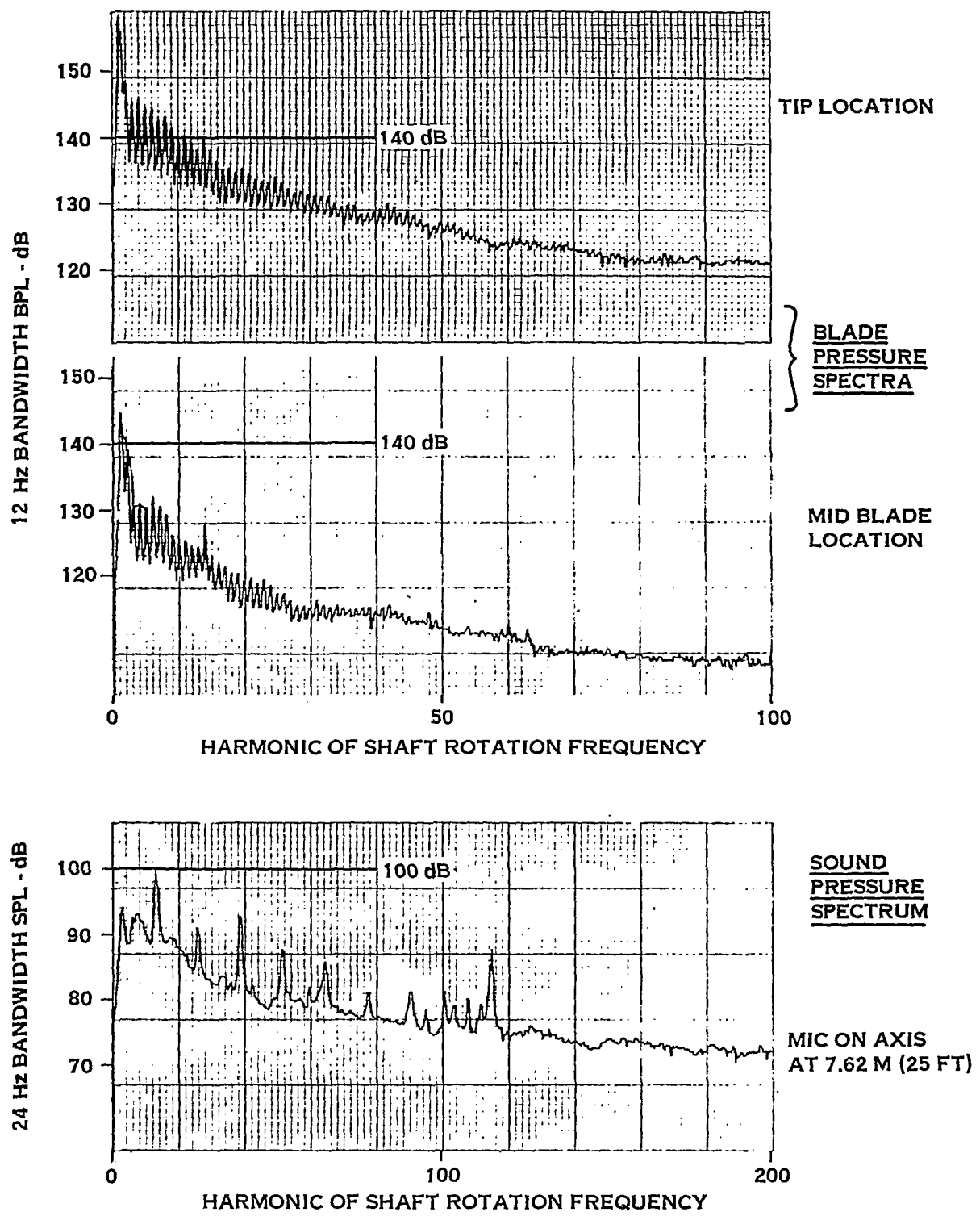
FIGURE 35. BLADE AND SOUND PRESSURE SPECTRA
CONDITION O–2 (CYLINDER OUT)

97
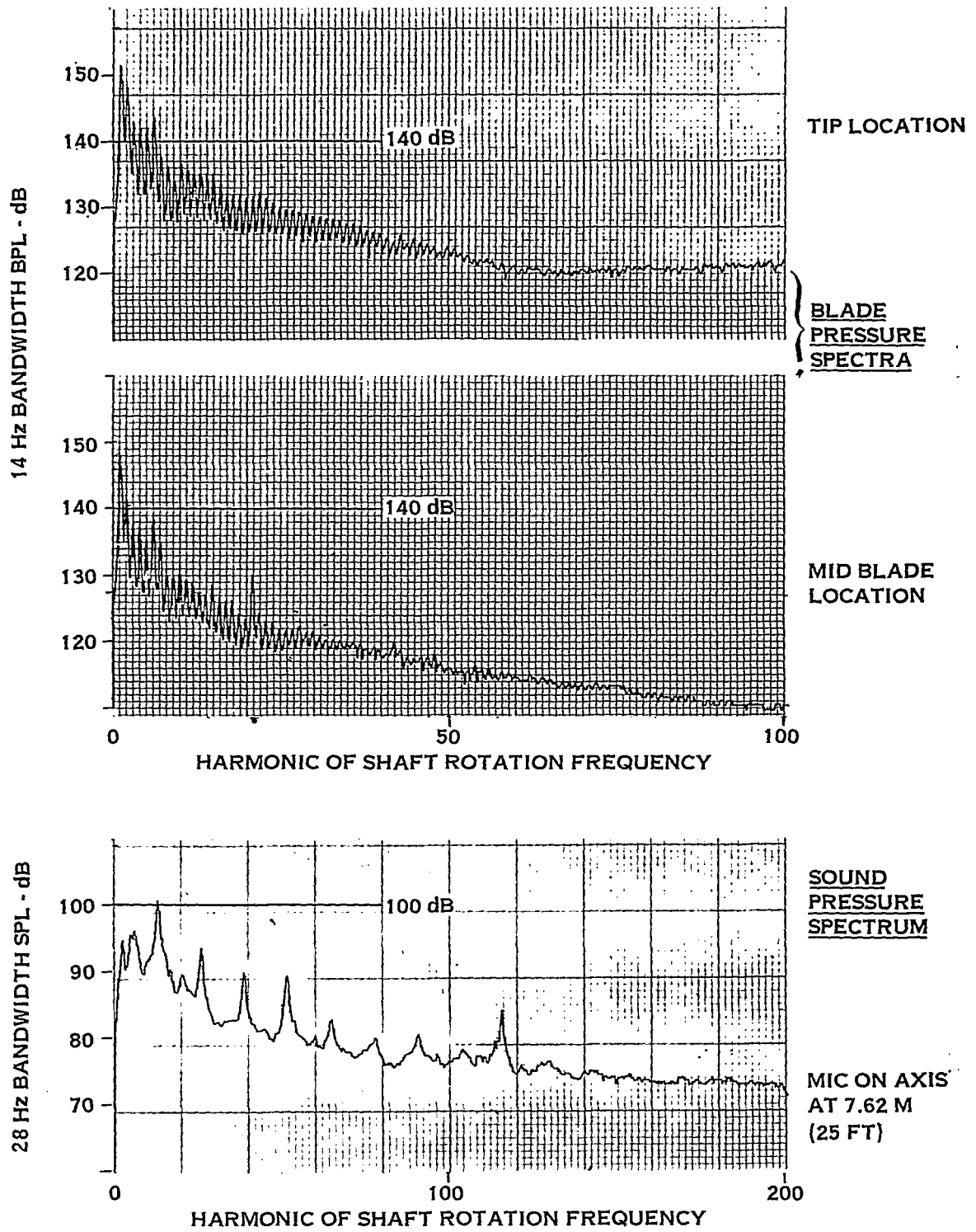
FIGURE 36.   BLADE AND SOUND PRESSURE SPECTRA
CONDITION O—3A (CYLINDER OUT)
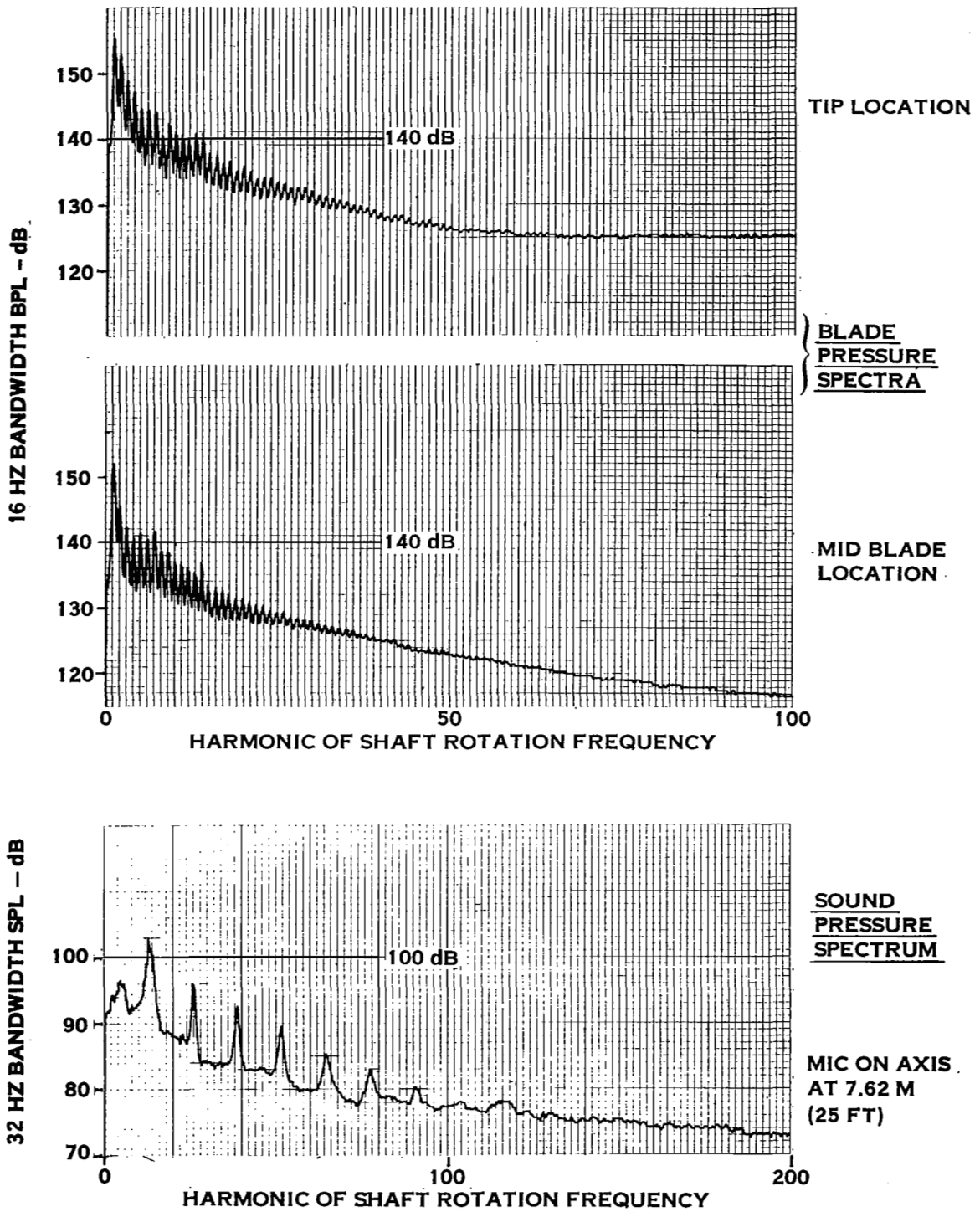
FIGURE 37. BLADE AND SOUND PRESSURE SPECTRA
CONDITION 0-4 (CYLINDER OUT)
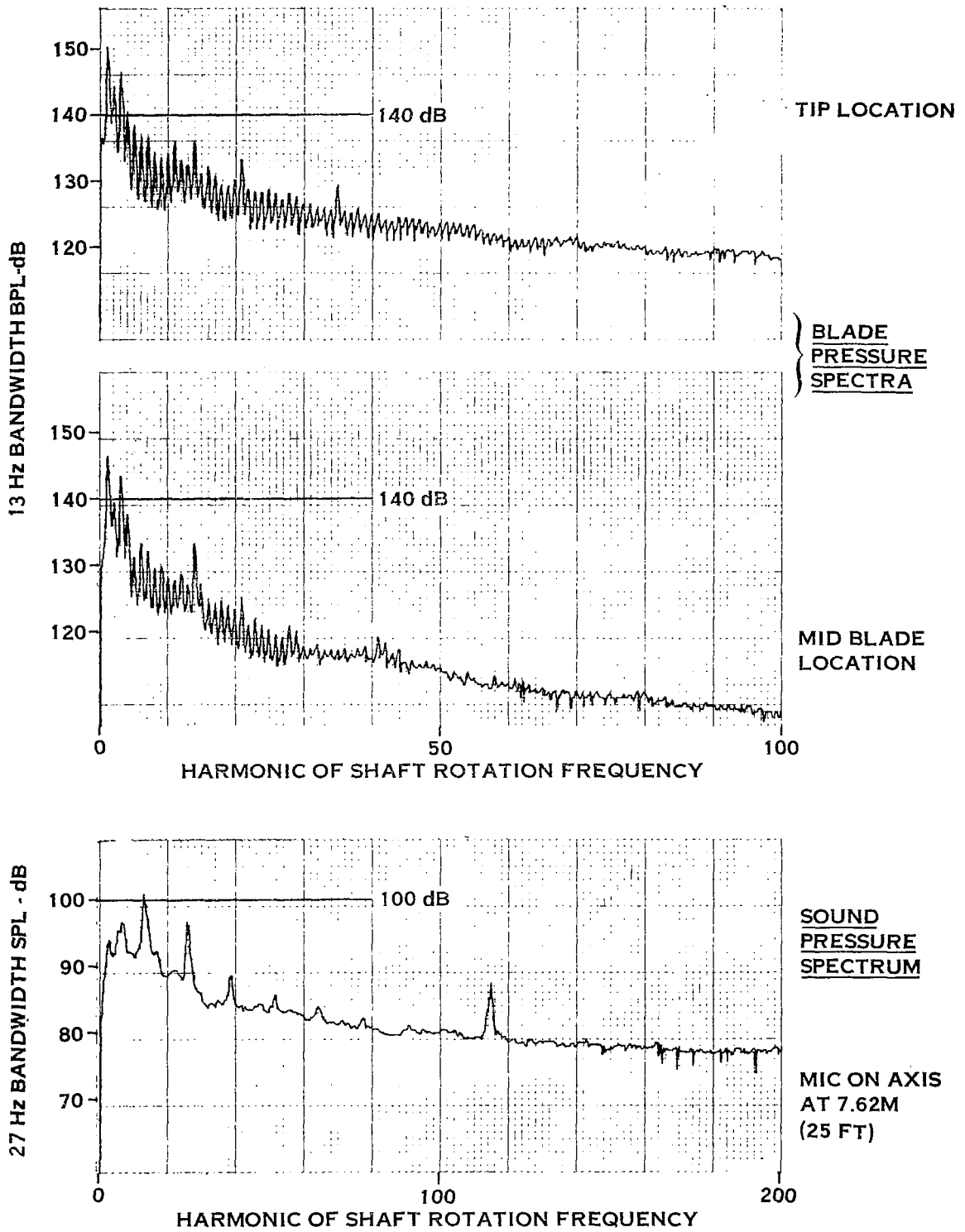
FIGURE 38.   BLADE AND SOUND PRESSURE SPECTRA
CONDITION O—5A (CYLINDER OUT)
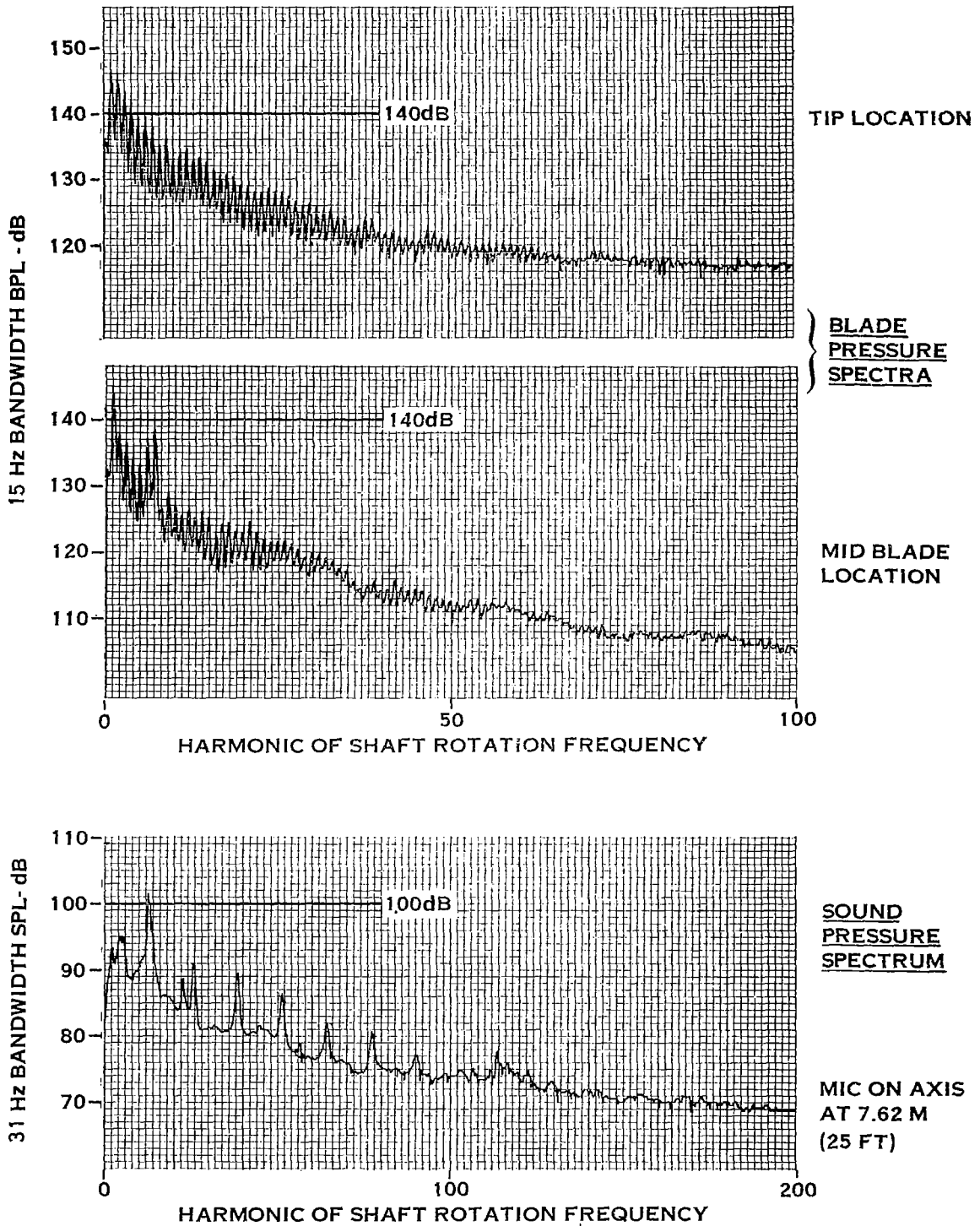
FIGURE 39 BLADE SOUND PRESSURE SPECTRA
CONDITION Q-6 (CYLINDER OUT)

101
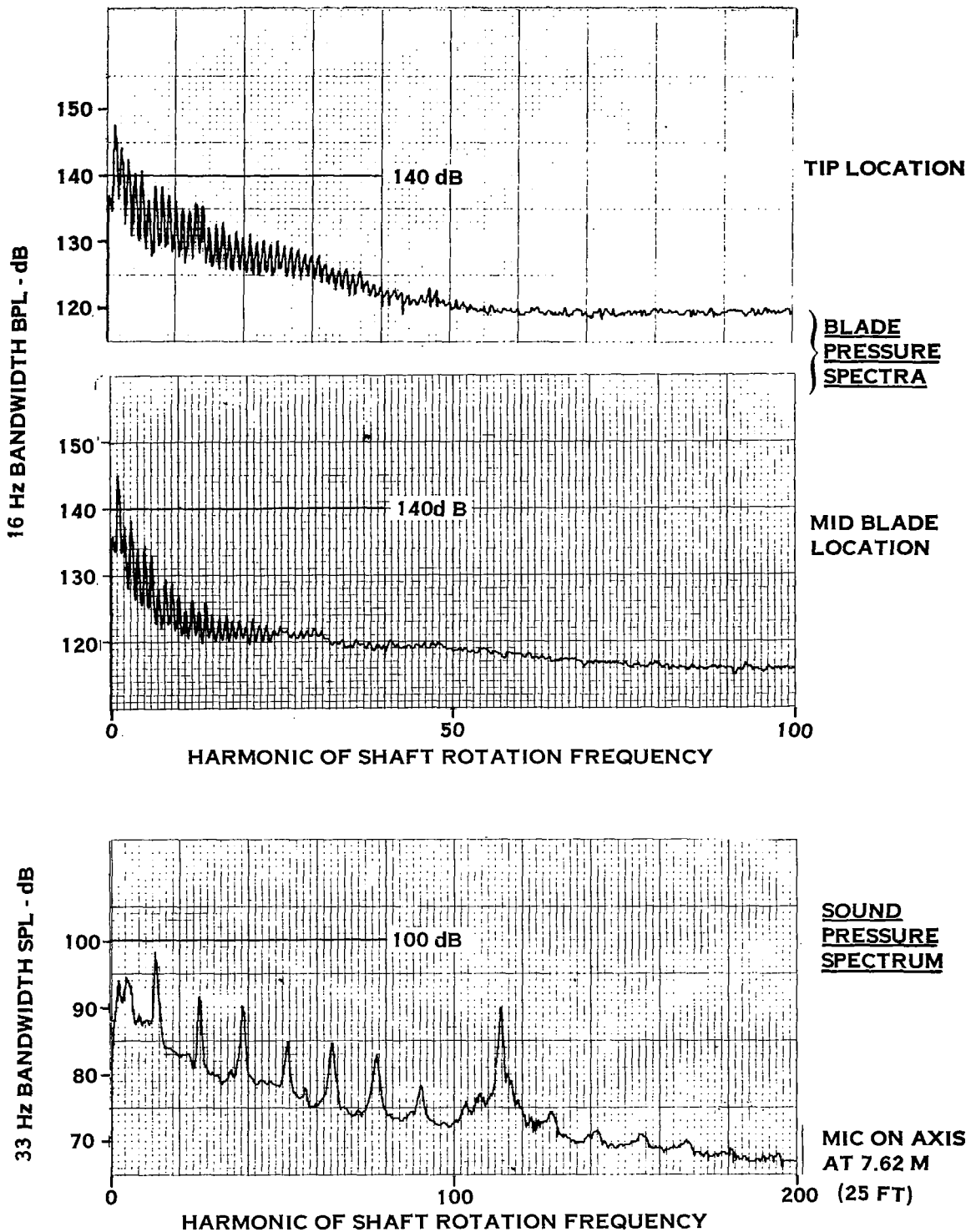
FIGURE 40. BLADE AND SOUND PRESSURE SPECTRA
CONDITION O—7A (CYLINDER OUT)
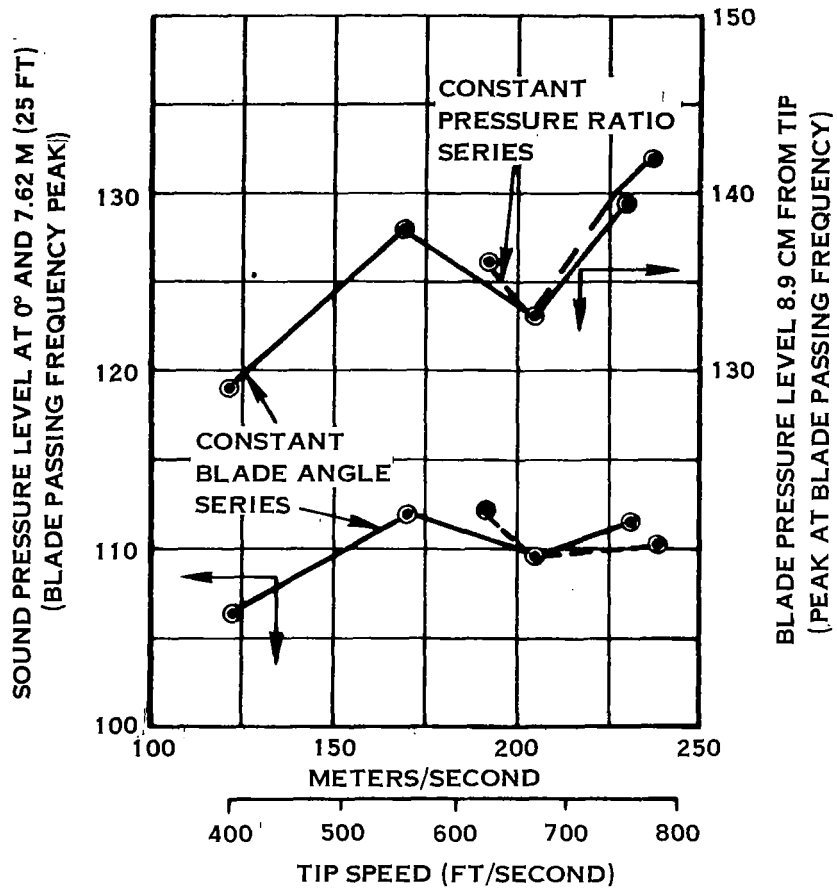
FIGURE 41. NOISE AND BLADE PRESSURE SPECTRUM PEAKS AT
BLADE PASSING FREQUENCY PLOTTED VERSUS TIP SPEED
WITH DISTORTION CYLINDER IN.

103
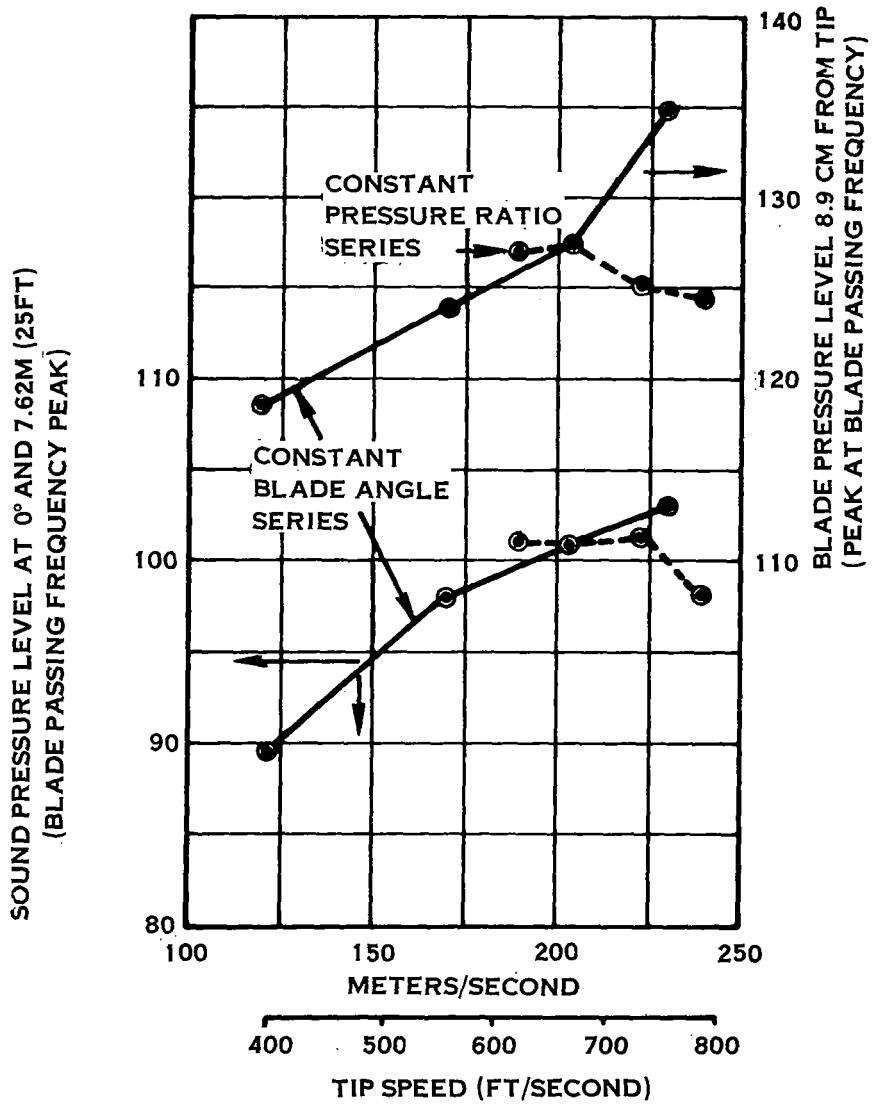
FIGURE 42   NOISE AND BLADE PRESSURE SPECTRUM PEAKS AT
BLADE PASSING FREQUENCY PLOTTED VERSUS TIP
SPEED WITH DISTORTION CYLINDER OUT
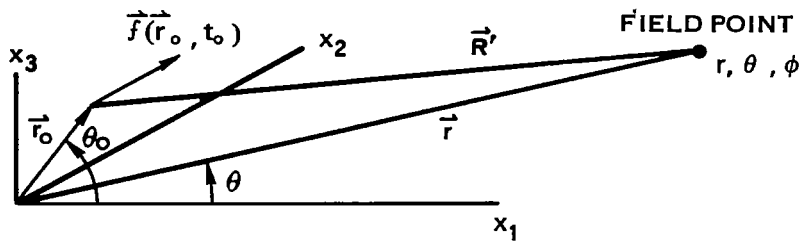
FIGURE 43. SOURCE AND OBSERVER COORDINATES. (ϕ AND ϕ_o MEASURED FROM x_2 IN $x_1 = 0$ PLANE)
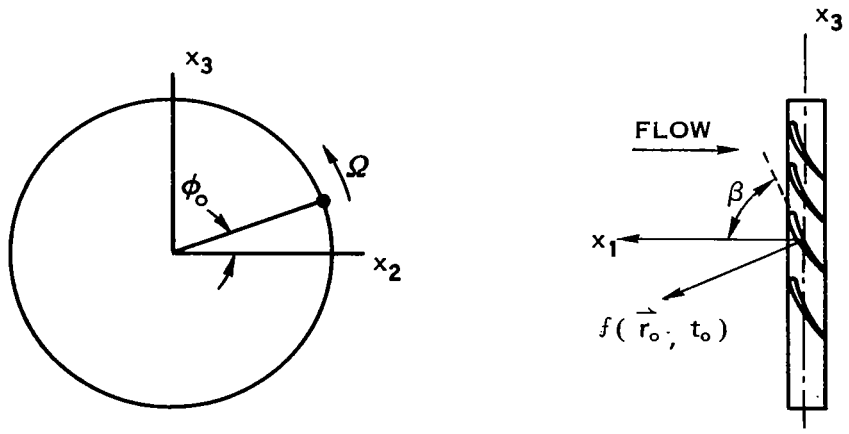
FIGURE 44. ROTOR GEOMETRY (RIGHT HAND COORDINATE SYSTEM)

105

3-DIMENSIONAL VIEW OF PRESSURE DISTRIBUTION ON BLADE

PRESSURE
TRANSDUCER
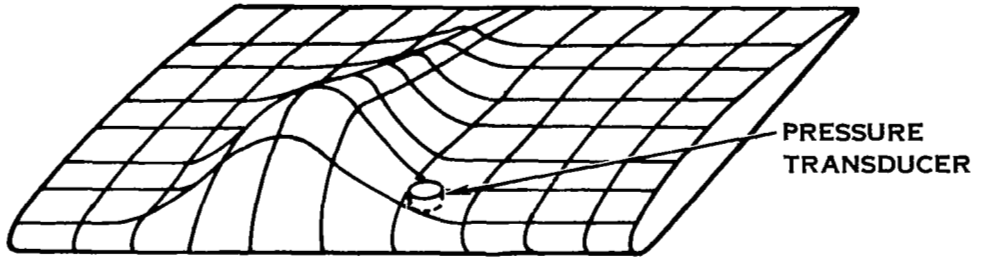
VIEW OF BLADE FROM LEADING EDGE

$f_r(r_0)$

1.0

PRESSURE
TRANSDUCER

r_0

0

R_H R_V R_X R_T

END VIEW

$f_\phi(\phi_0)$

$r_0\phi_0$

TIME WAVEFORMS

$$p_{vum}(t_0') = A_{vum} p_s \left(\frac{t_0 \cdot t_{vum}}{w_{vum}} \right)$$

$p_s(t_0')$

p_0

STANDARD PULSE

0   t_0

GENERAL PULSE

t_{vum} t_0
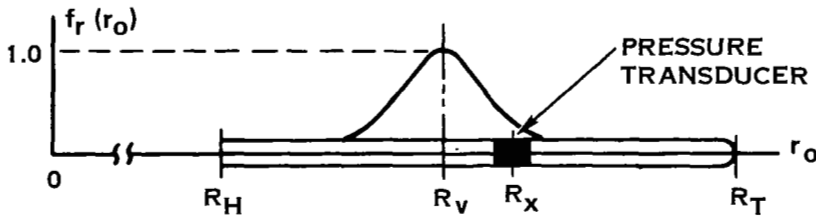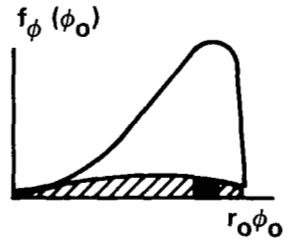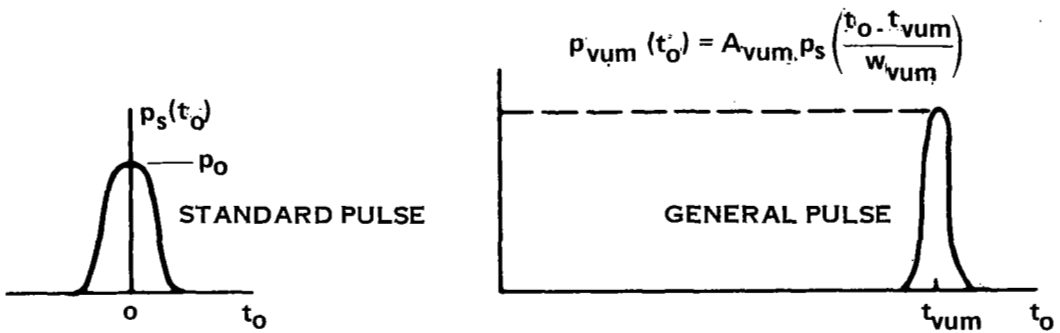
FIGURE 45. GENERAL FORM FOR SOURCE PULSE
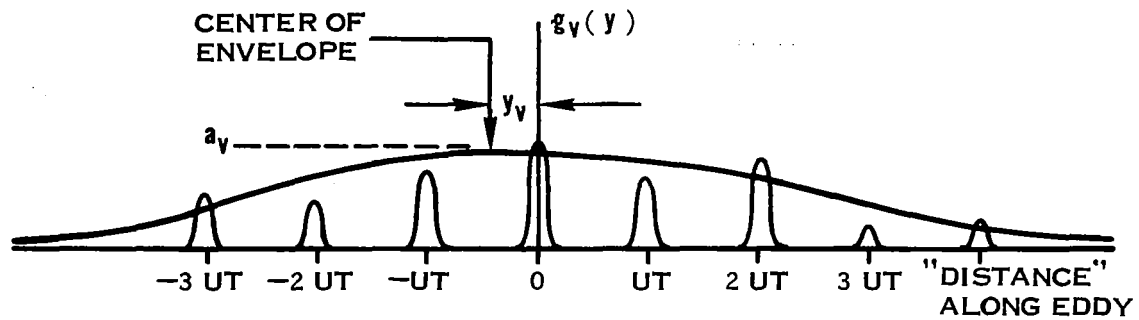
FIGURE 46. TYPICAL PULSE ENVELOPE
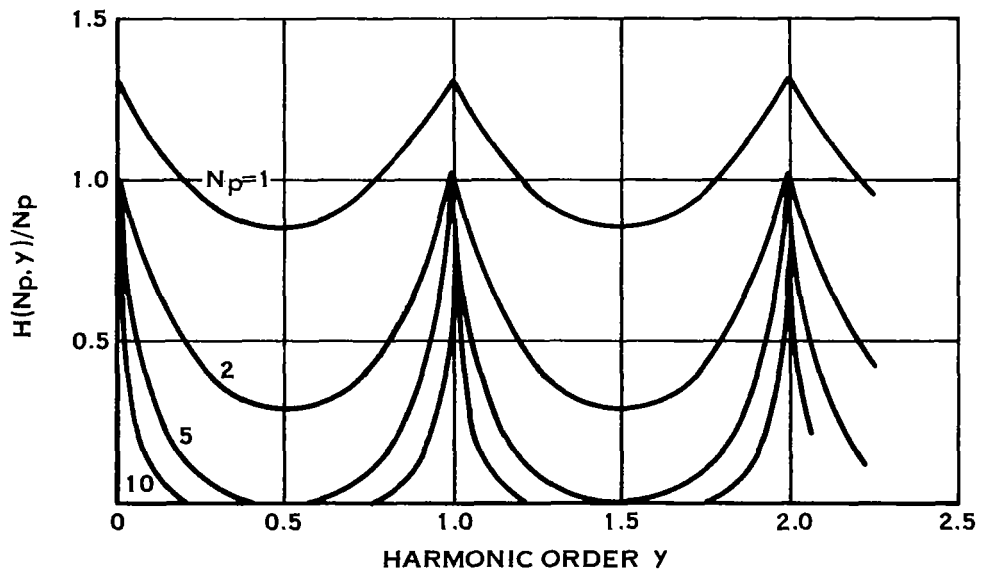
FIGURE 47. PEAK FUNCTION NORMALIZED TO NUMBER OF PULSES IN EDDY N_p

$G_{\beta 0}(f)$

FILTER RESPONSE

-10 dB

-20 dB

-30 dB

REAL FILTER

SYNTHESIZED FILTER

-40 dB

-50 dB

-4β -3β -2β $-\beta$ 0 β 2β 3β 4β
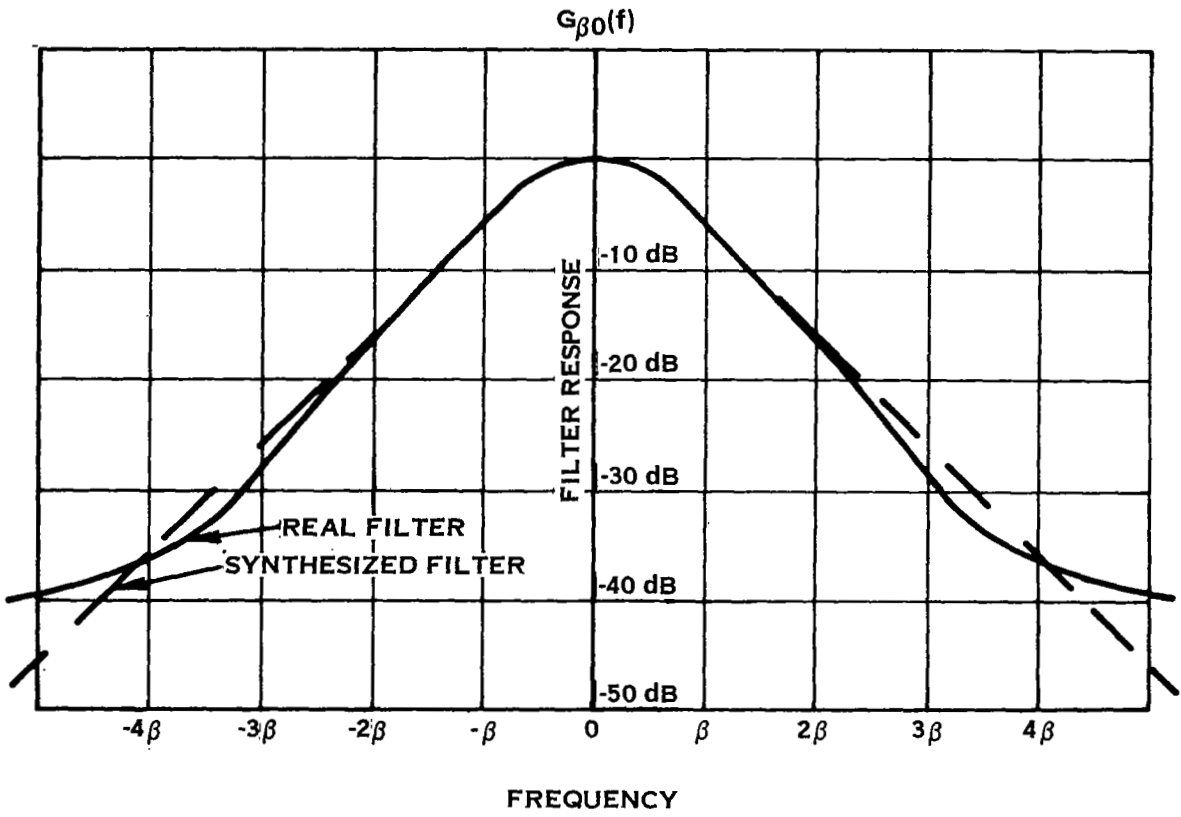
FREQUENCY

FIGURE 48.   SHAPES OF REAL AND SYNTHESIZED FILTER
PASSBANDS (β = FREQUENCY SPACING OF FILTERS)

THEORETICAL FILTERED SPECTRA FOR SAME PSD   **EXPERIMENTAL FILTERED SPECTRA FOR SAME SIGNAL**
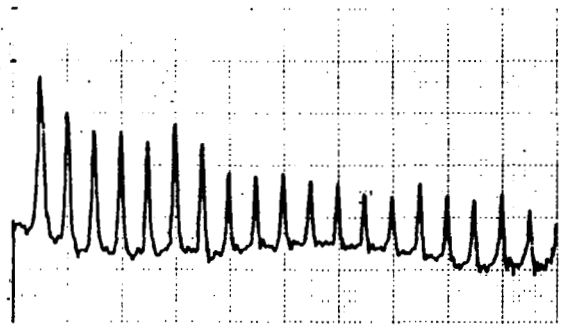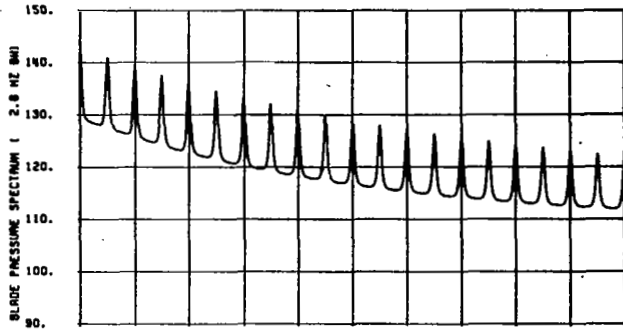
FULL SCALE FREQUENCY = 920 HZ
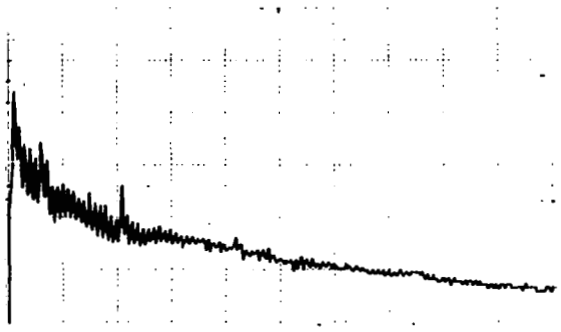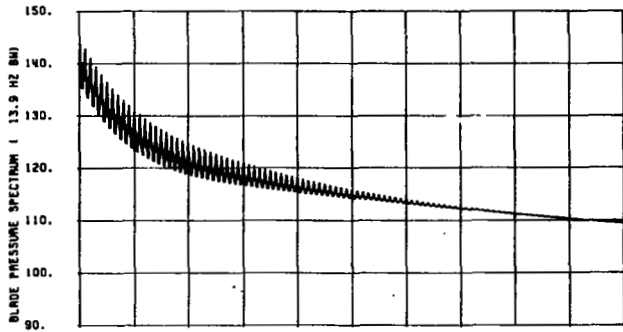
FULL SCALE FREQUENCY = 4620 HZ
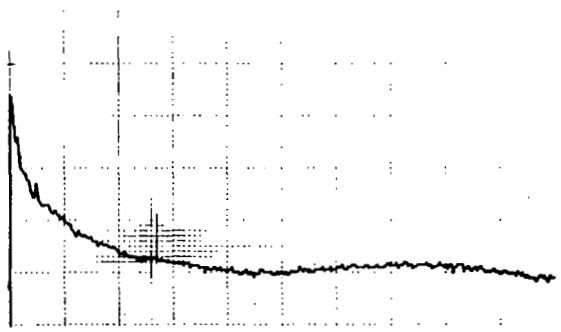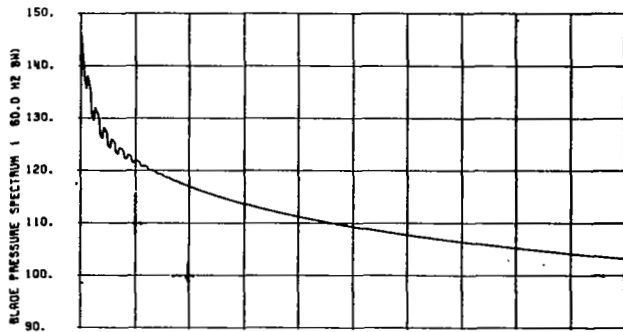
FULL SCALE FREQUENCY = 20,000 HZ

FIGURE 49. COMPARISON OF THEORETICAL AND EXPERIMENTAL FILTER BEHAVIOR
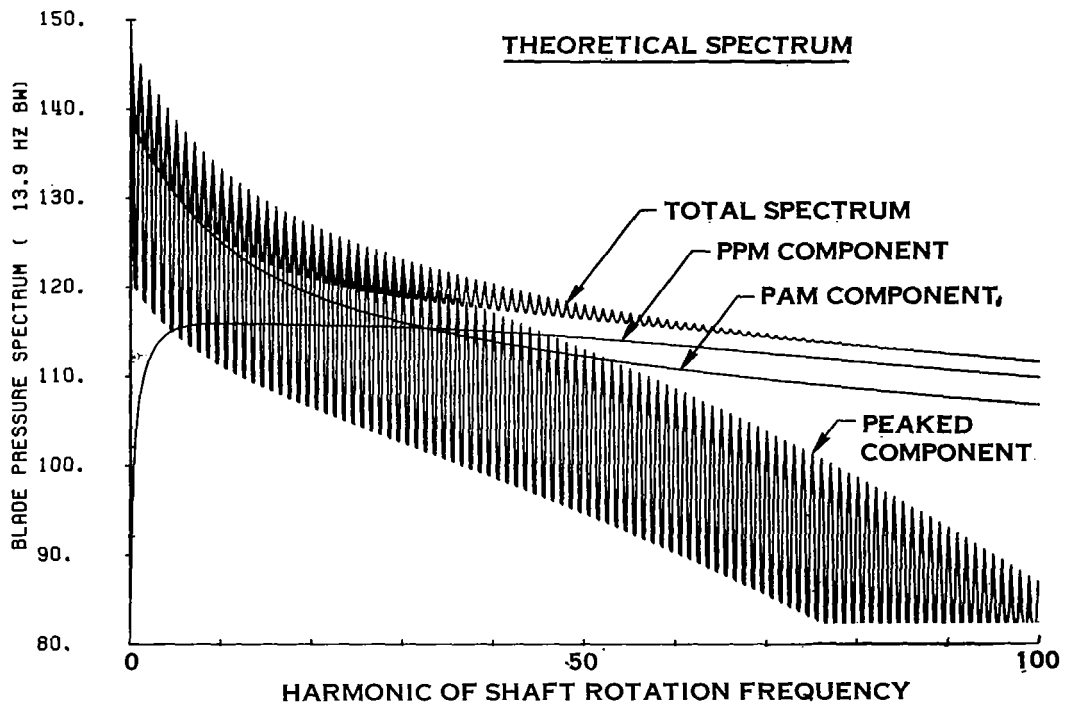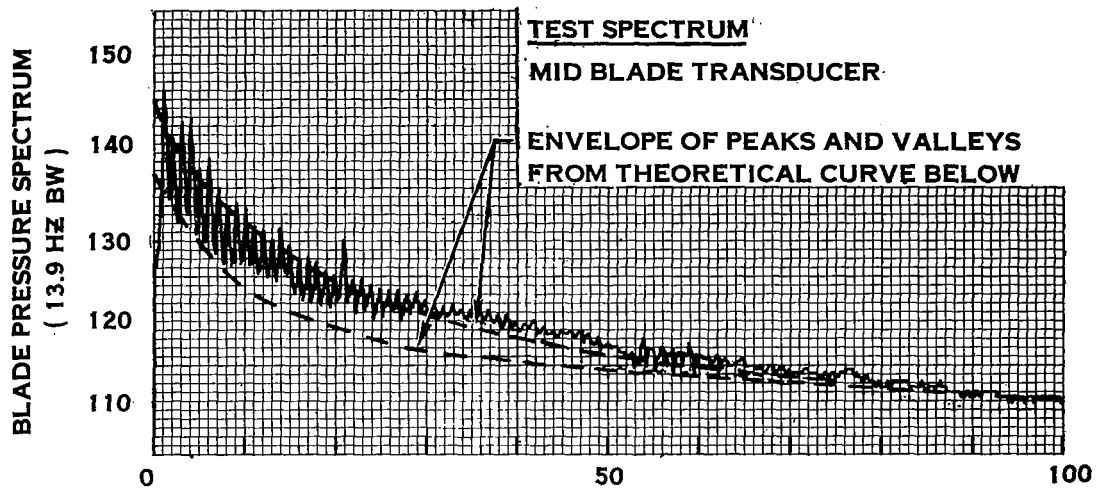
FIGURE 50. COMPARISON OF EXPERIMENTAL AND THEORETICAL BLADE PRESSURE
SPECTRUM (TEST CONDITION 0 – 3 B)
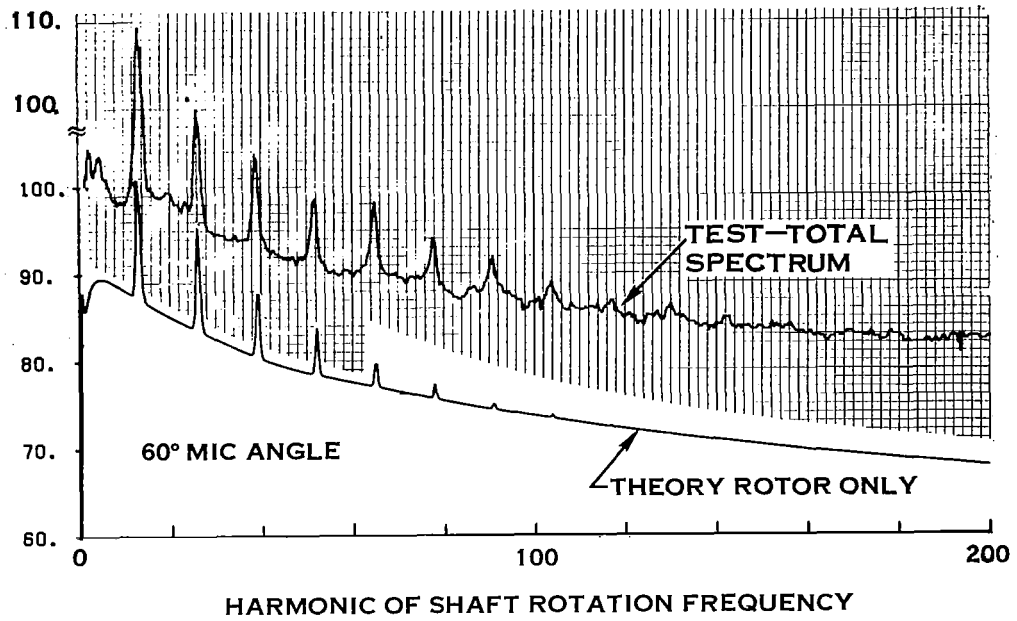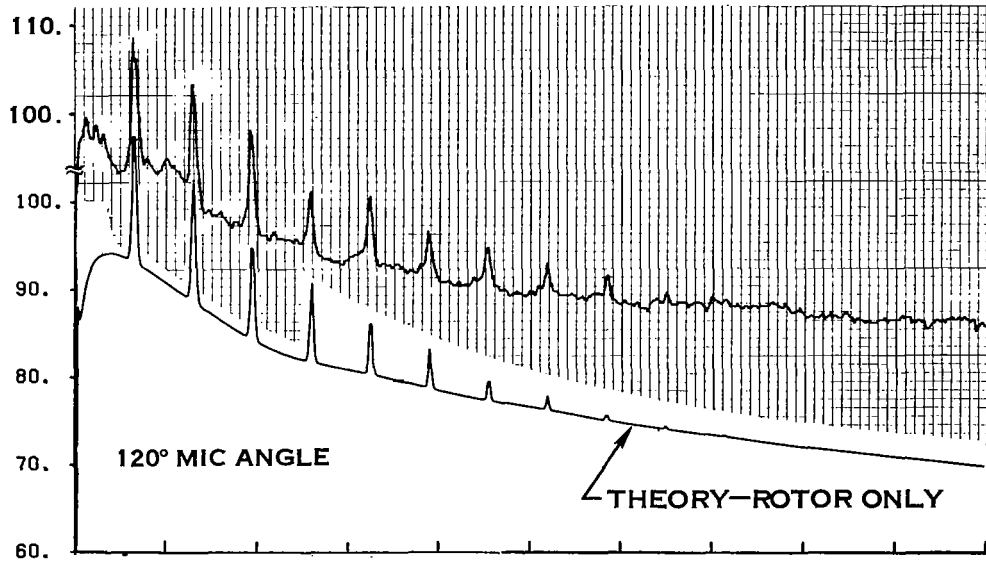
FIGURE 51. COMPARISON OF EXPERIMENTAL AND THEORETICAL
SOUND PRESSURE SPECTRA. TEST CONDITION 0 - 3 B

111

FIGURE 52. COMPARISON OF EXPERIMENTAL AND THEORETICAL
DIRECTIVITY PATTERNS – TEST CONDITION 0-3B
(CYLINDER OUT)

112
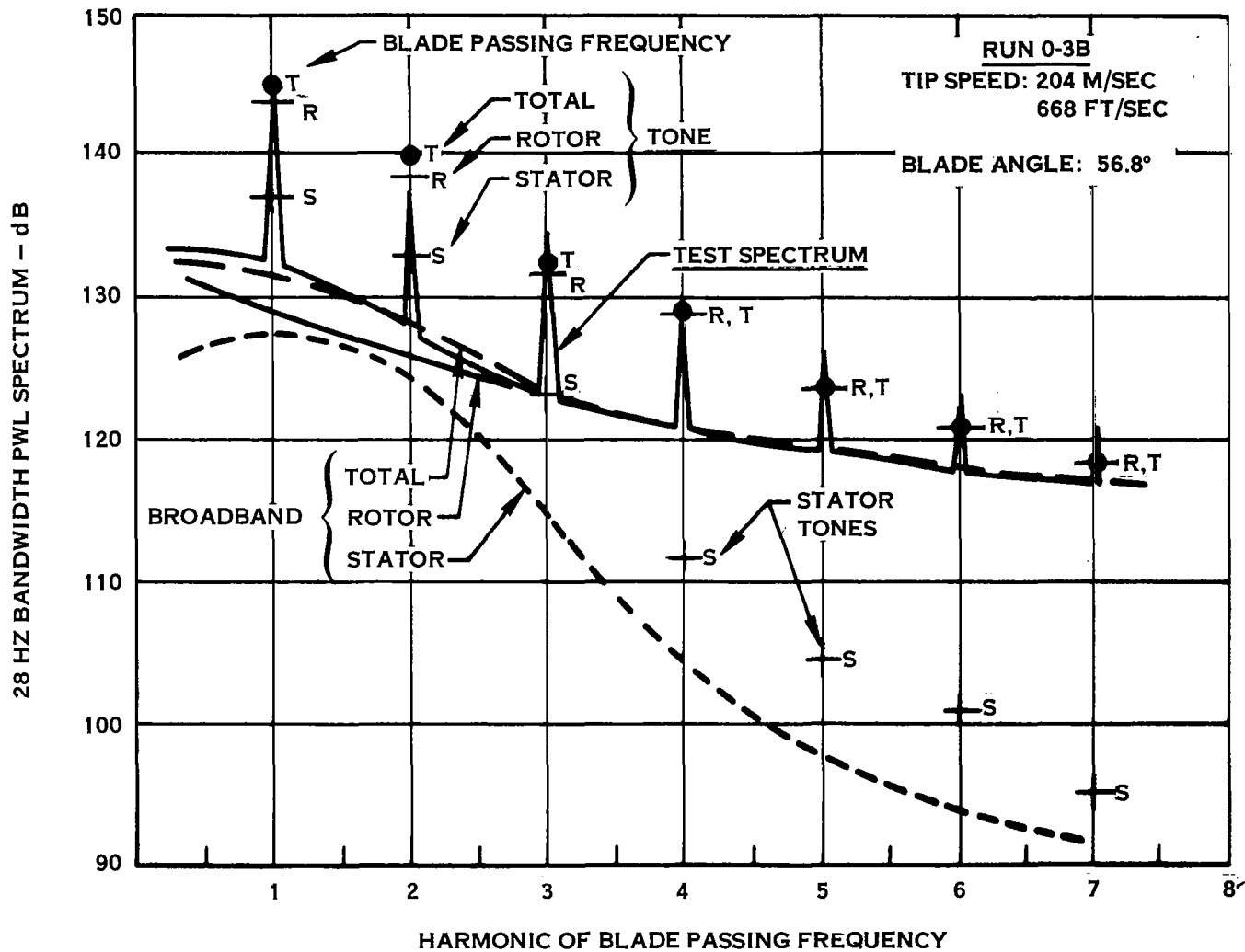
FIGURE 53. COMPARISON OF THEORETICAL AND EXPERIMENTAL
SOUND POWER SPECTRA (TEST CONDITION 0-3B)
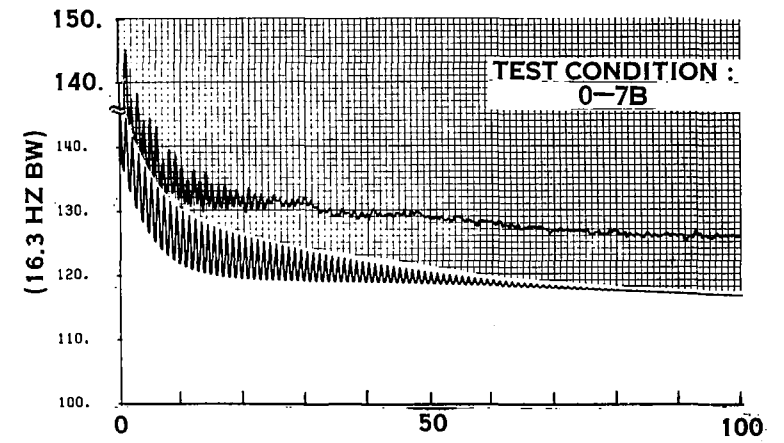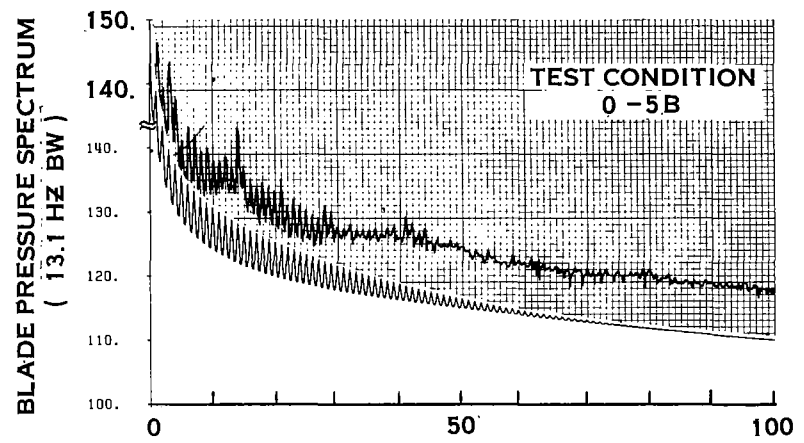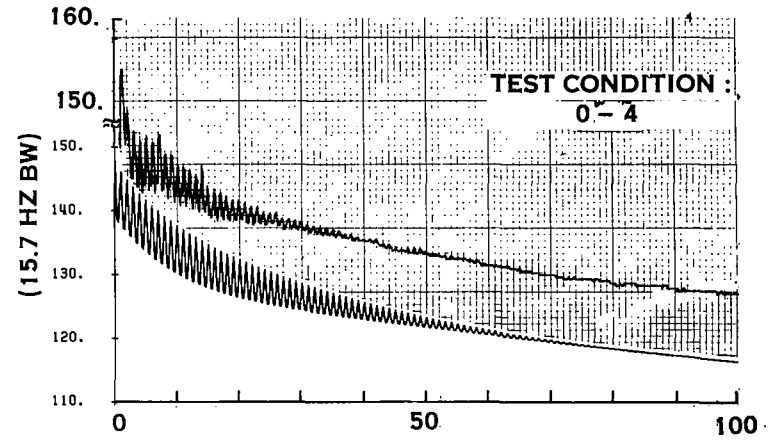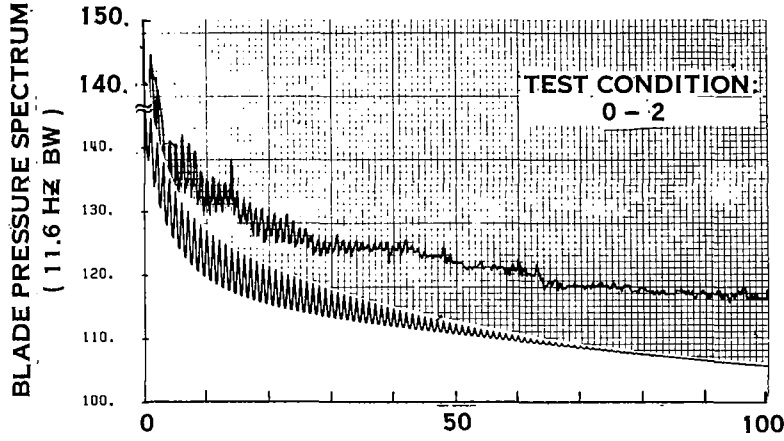
FIGURE 54. FIT OF THEORETICAL BLADE PRESSURE SPECTRA TO SPECTRA MEASURED BY
MID BLADE TRANSDUCER (CLEAN INLET)
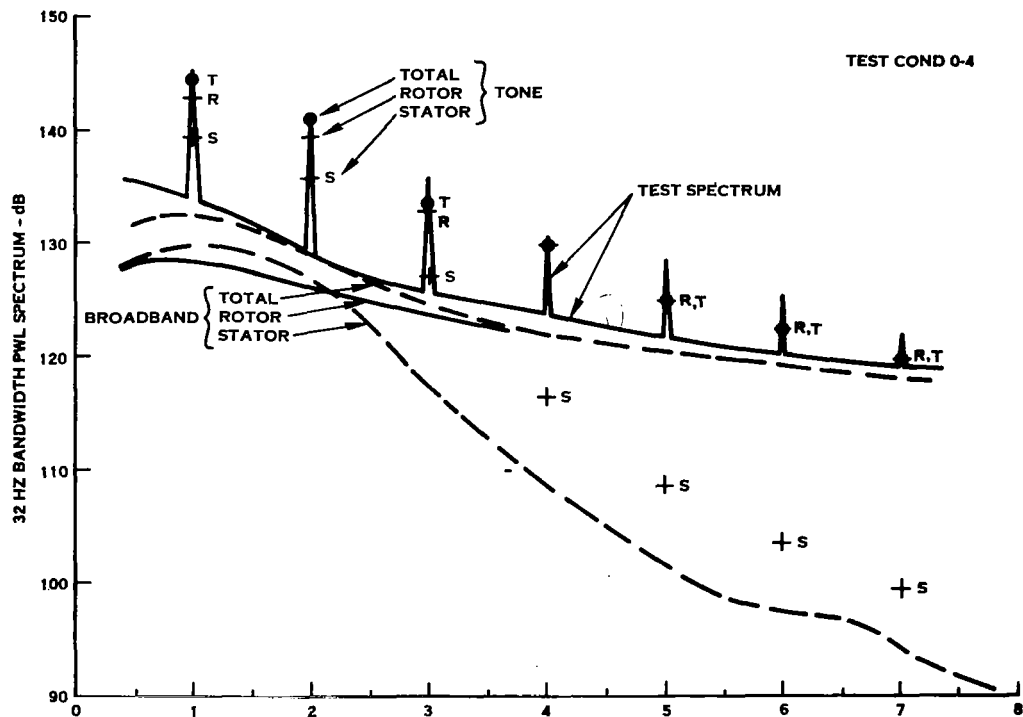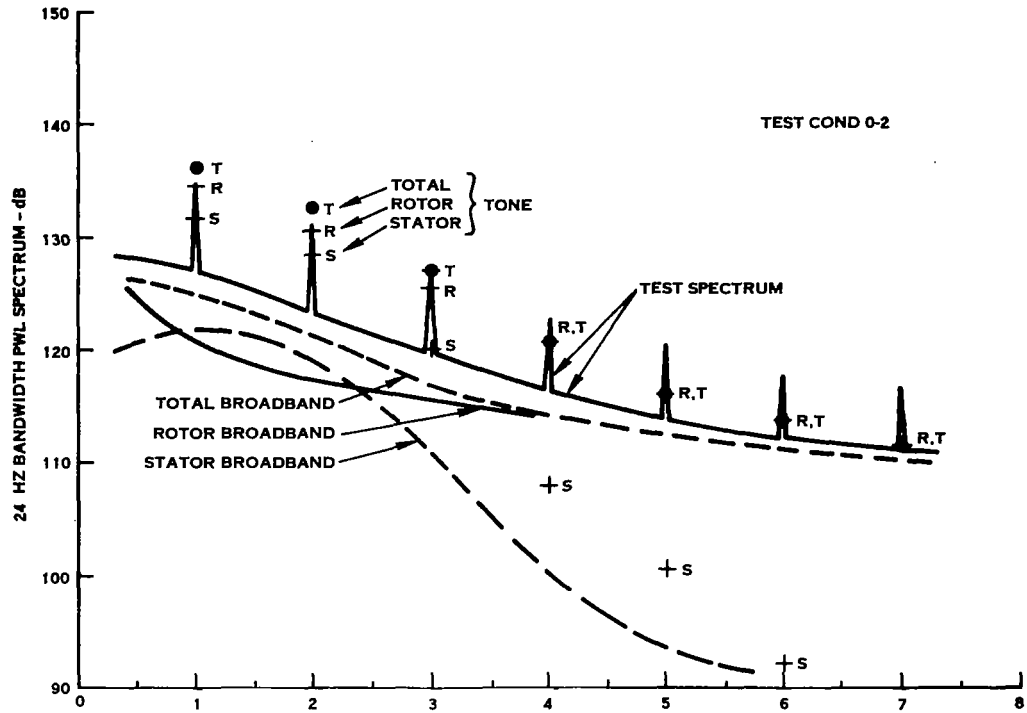
FIGURE 55. COMPARISON OF THEORETICAL AND EXPERIMENTAL
SOUND POWER SPECTRA FOR CONDITIONS 0-2 AND 0-4

115
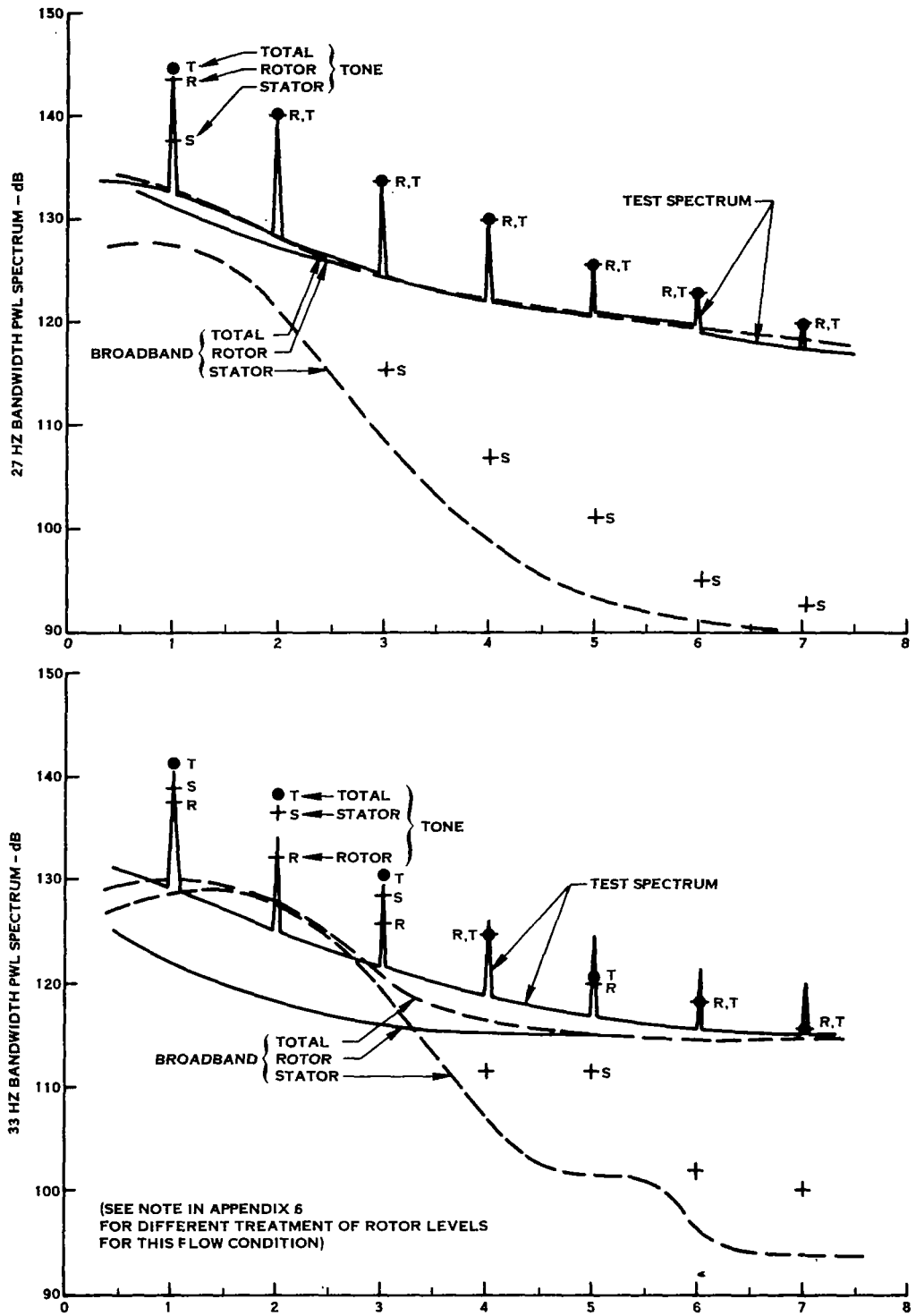
FIGURE 56.   COMPARISON OF THEORETICAL AND EXPERIMENTAL
SOUND POWER SPECTRA FOR CONDITIONS 0-5B AND 0-7B

116
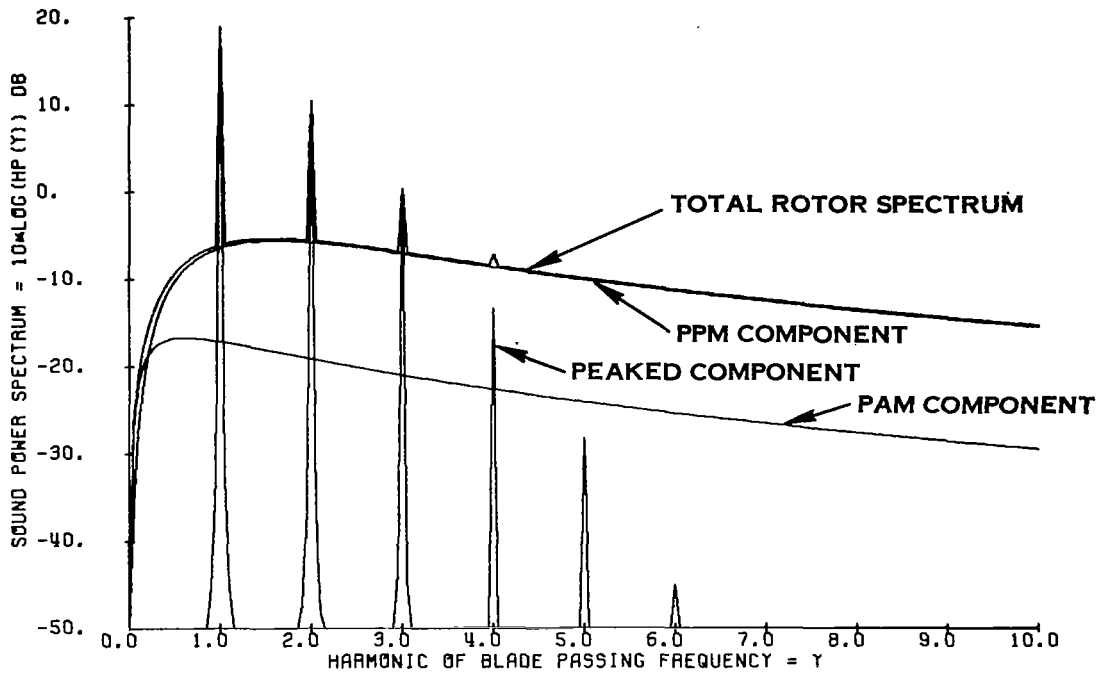
FIGURE 57 BASE CASE FOR ACOUSTIC PARAMETER STUDY
REPRESENTING Q - FAN DEMONSTRATOR
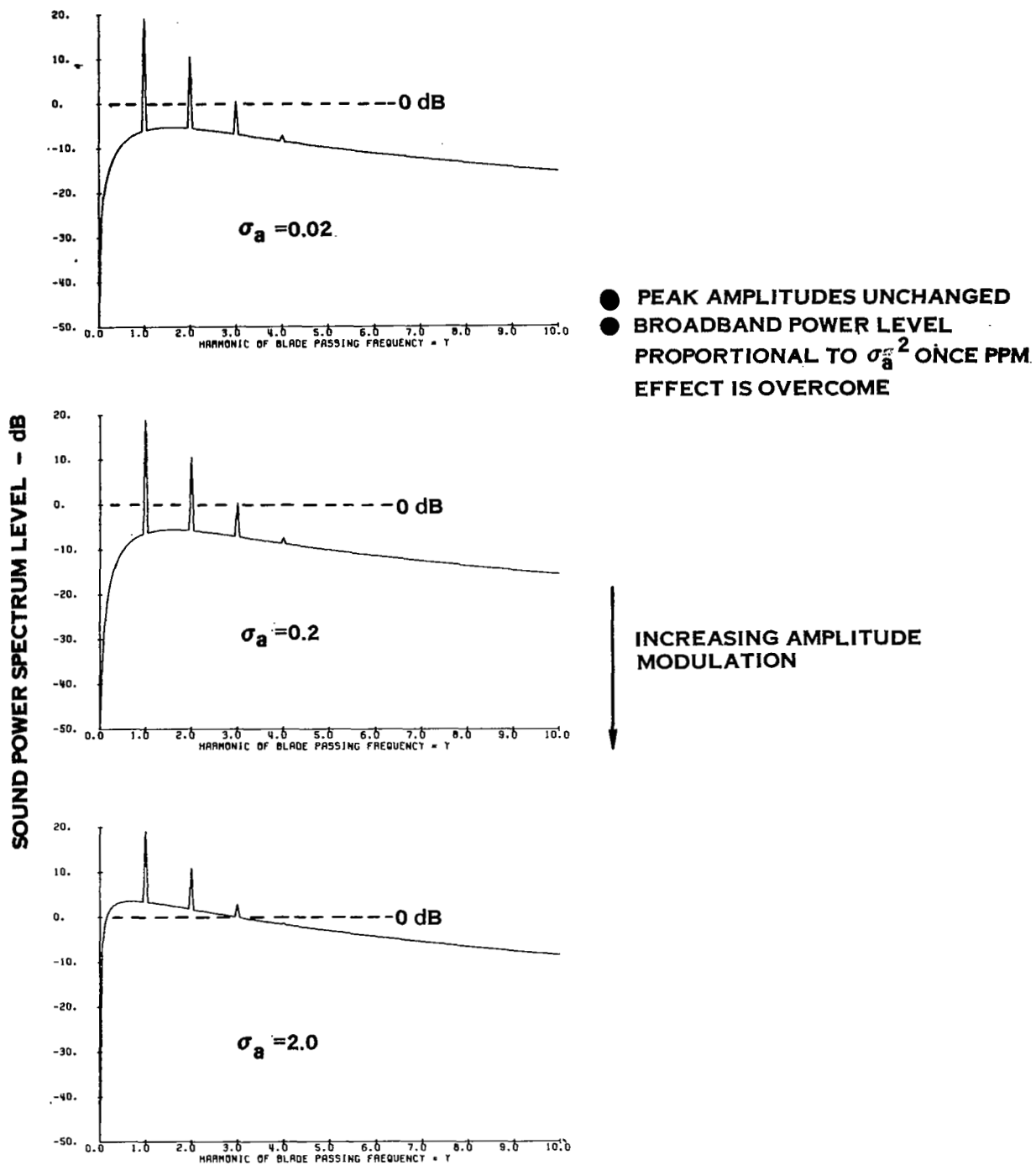
FIGURE 58 EFFECT OF AMPLITUDE MODULATION ON POWER SPECTRUM

HARMONIC PEAK
AT BLADE PASSING FREQUENCY

10 dB

ANY σ_a

0°

90°

180°

● PAM DOES NOT
INFLUENCE DIRECTIVITY

0°

$\sigma_a = 2.0$

$\sigma_a = 0.2$

$\sigma_a = 0.02$

BROADBAND
AT 1-1/2 TIMES BLADE
PASSING FREQUENCY
(PAM COMPONENT ONLY)

90°

180°
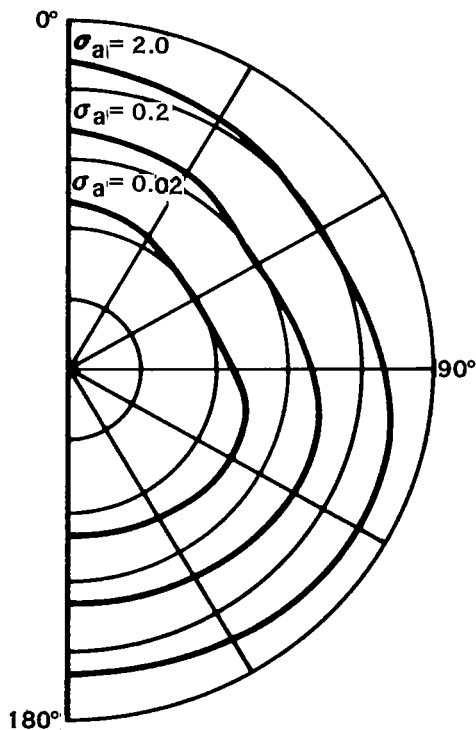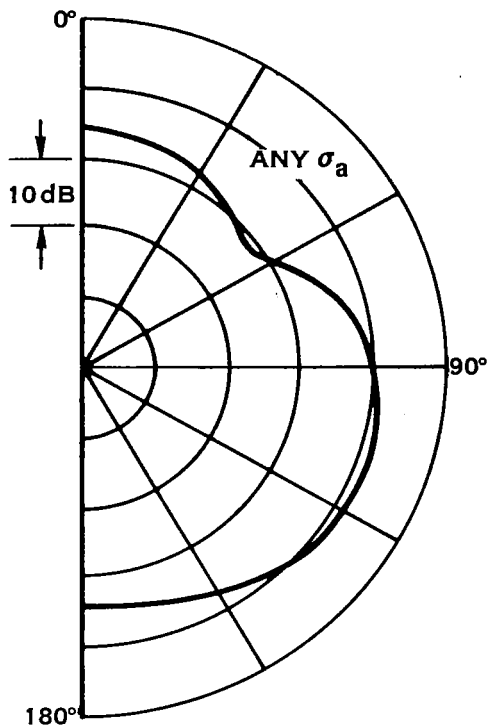
FIGURE 59 EFFECT OF AMPLITUDE MODULATION ON DIRECTIVITY

119
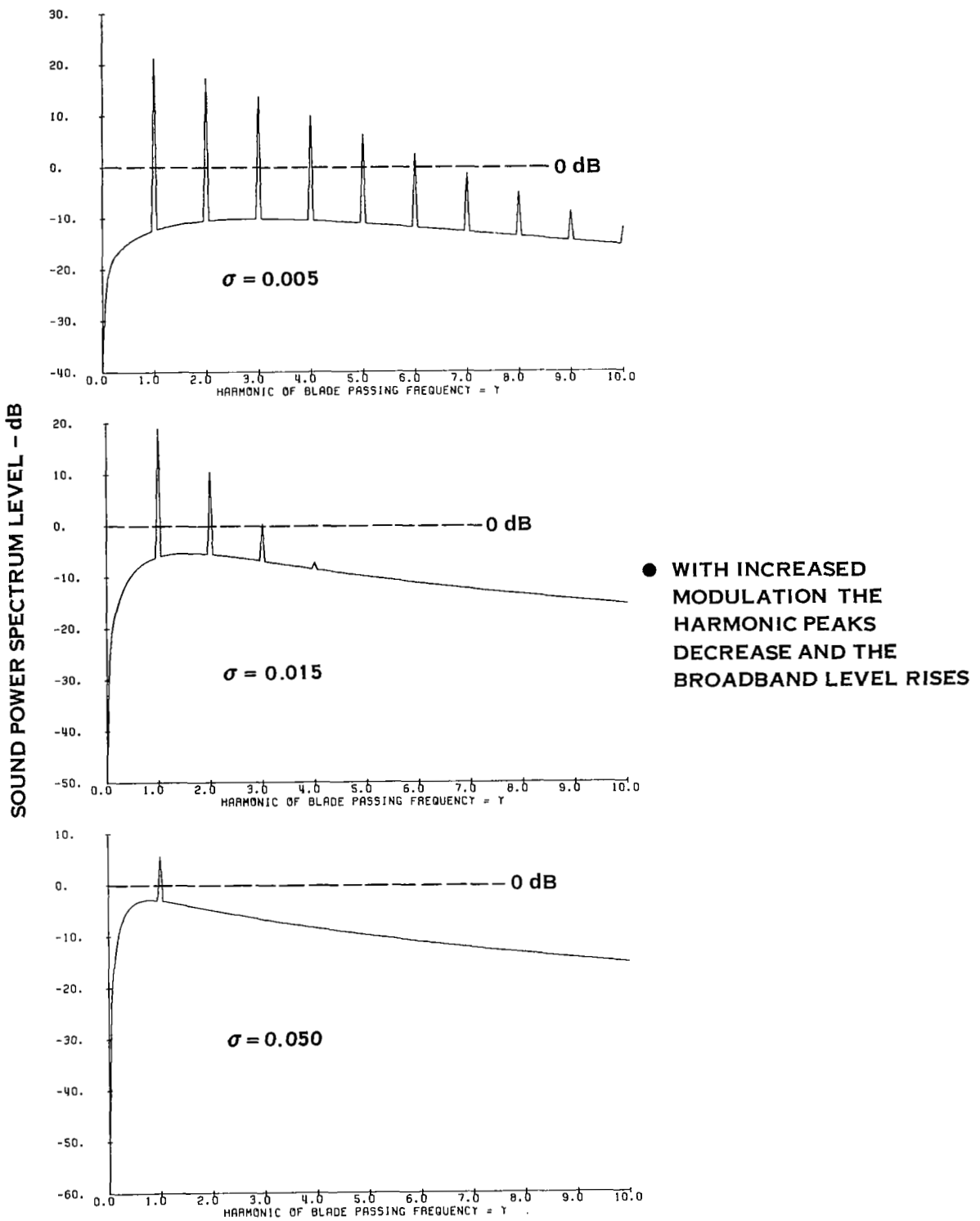
FIGURE 60 EFFECT OF POSITION MODULATION ON SPECTRUM LEVEL

0° FORWARD

$\sigma_i = 0.005$

$\sigma_i = 0.015$

$\sigma_i = 0.05$

HARMONIC PEAK
BPF FUNDAMENTAL

90°

180°

- POSITION MODULATION CHANGES
  DIRECTIVITY PATTERNS BY CHANGING
  RELATIVE LEVELS OF SPINNING MODES

0°

$\sigma_i = 0.05$

.015

$\sigma = 0.005$

10 dB

BROAD BAND
1-1/2 X BPF

90°

180°
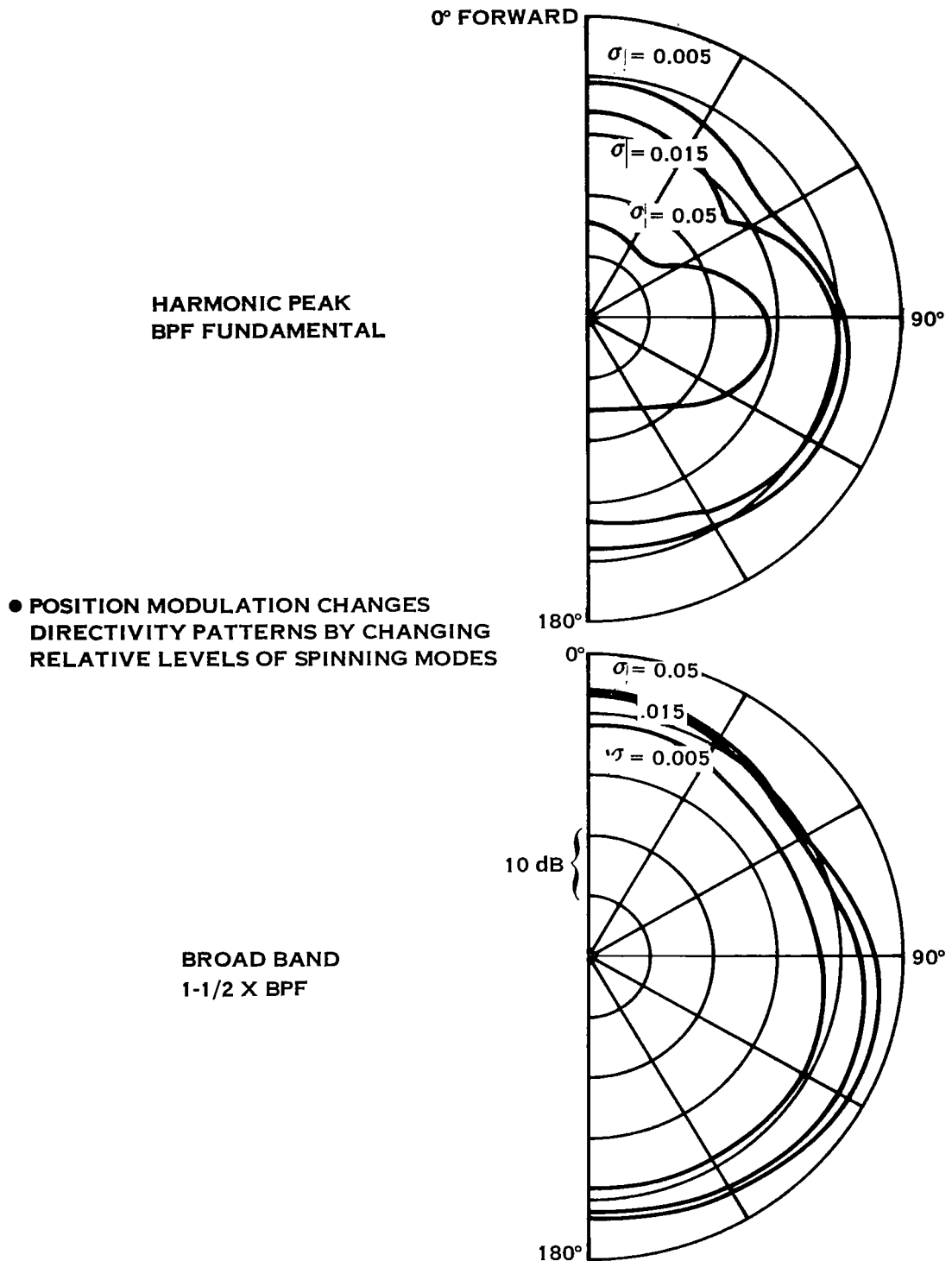
FIGURE 61. EFFECT OF POSITION MODULATION ON DIRECTIVITY

121
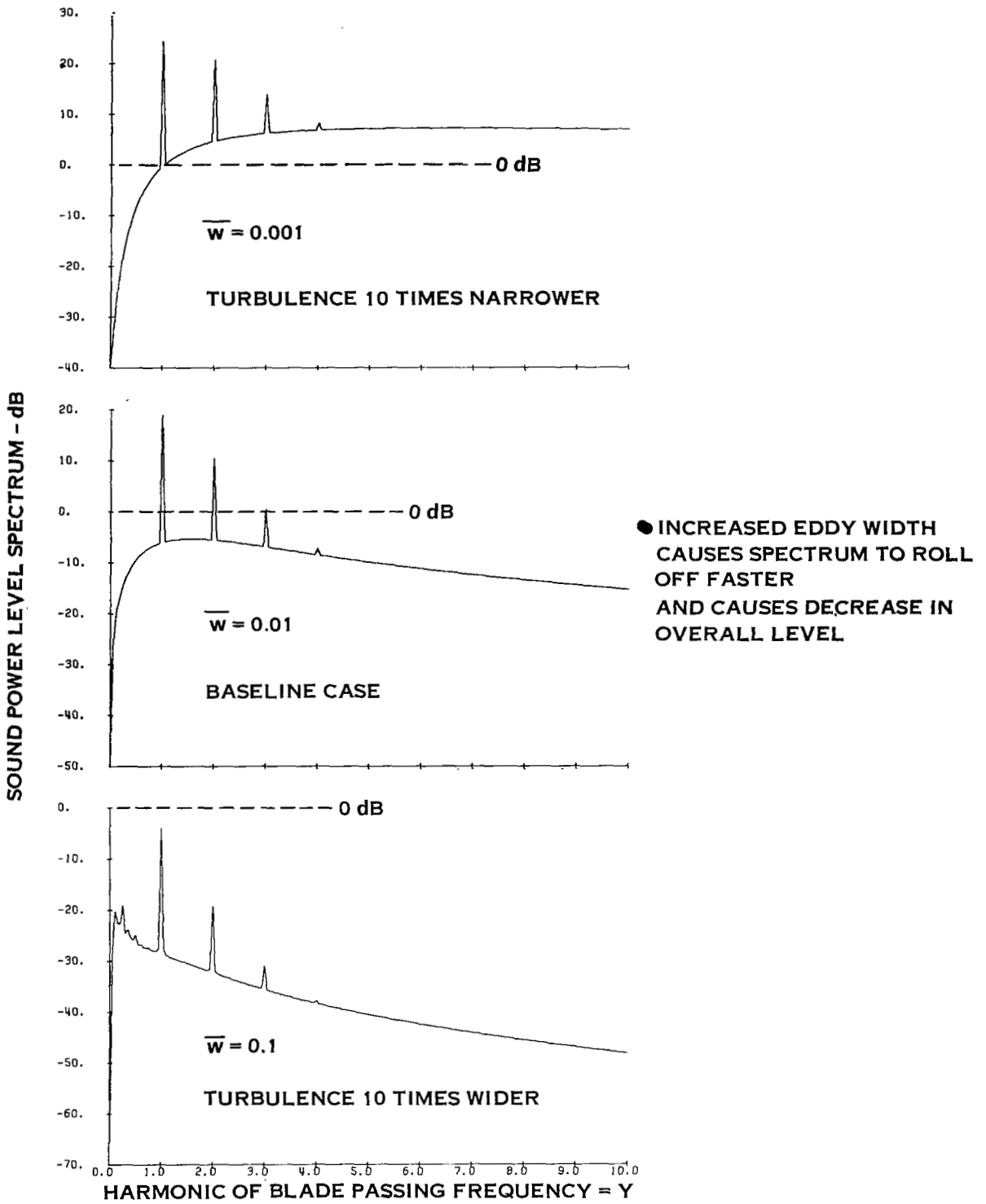
FIGURE 62 EFFECT OF TRANSVERSE SCALE OF TURBULENCE
ON POWER SPECTRUM

122

HARMONIC PEAK
BPF

● GREATER SELF-INTERFERENCE
WITH WIDE EDDIES CAUSES
MORE PRONOUNCED DIRECTIVITY
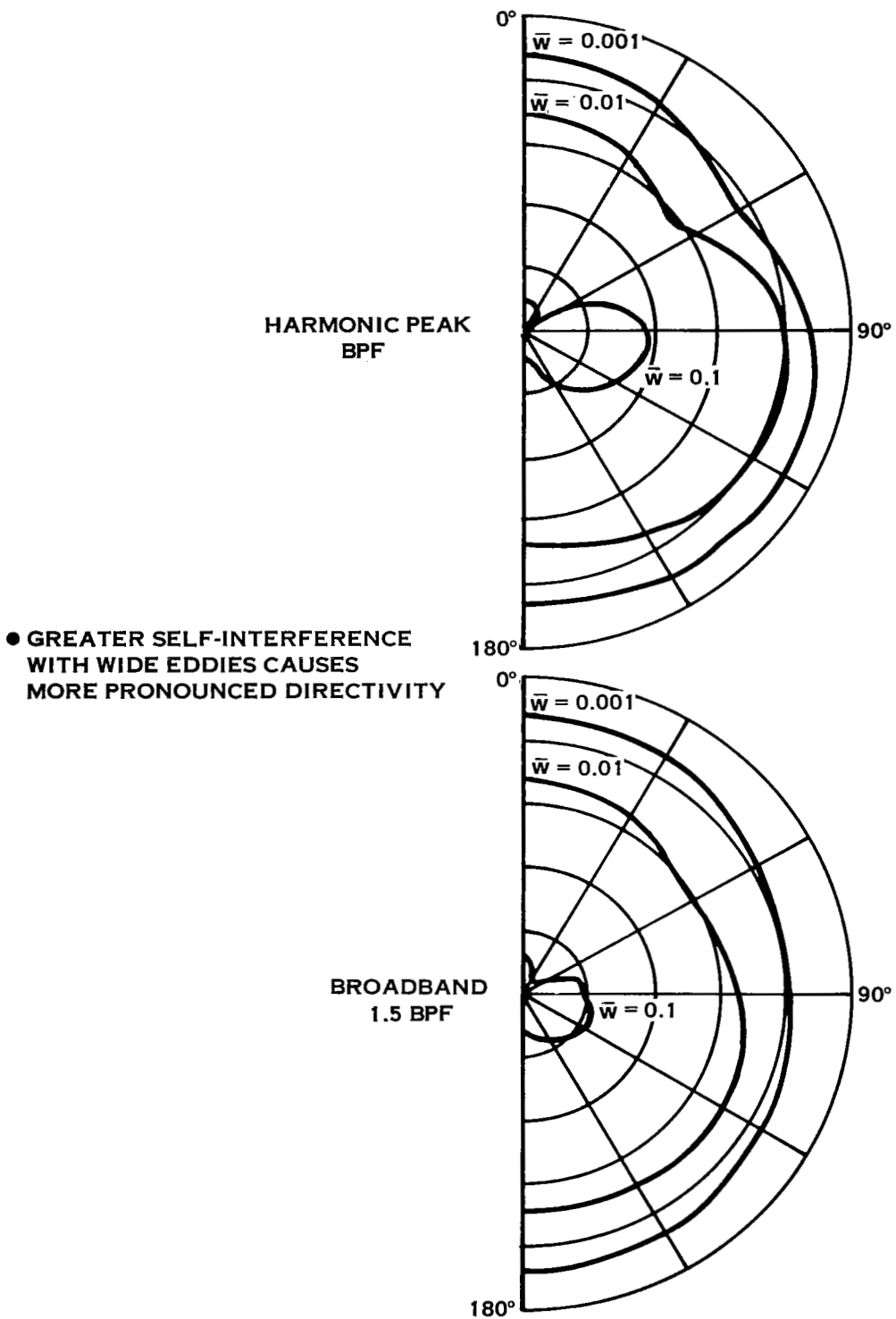
BROADBAND
1.5 BPF

FIGURE 63. EFFECT OF TRANSVERSE SCALE OF TURBULENCE ON DIRECTIVITY
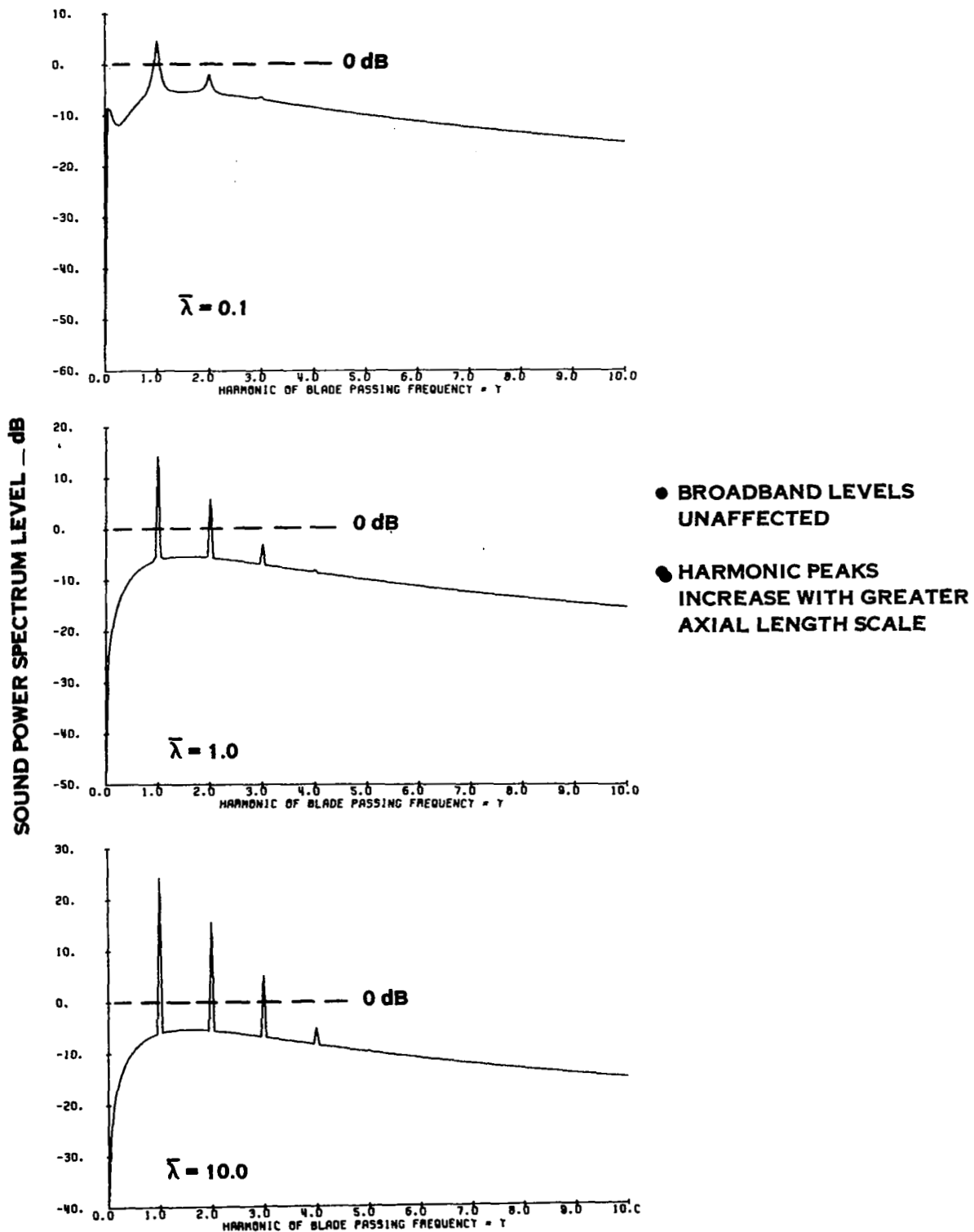
FIGURE 64   EFFECT OF AXIAL LENGTH SCALE OF TURBULENCE ON SPECTRUM LEVEL

HARMONIC PEAK
(BLADE PASSING
FREQUENCY)
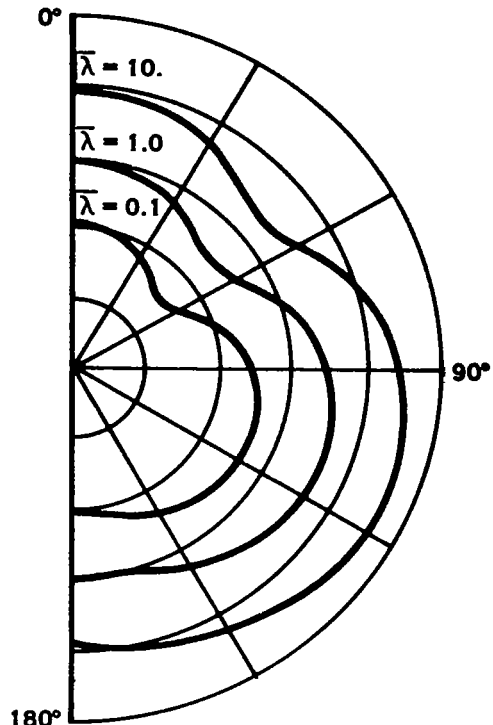
● NO EFFECT ON DIRECTIVITY

BROADBAND
(NO EFFECT)
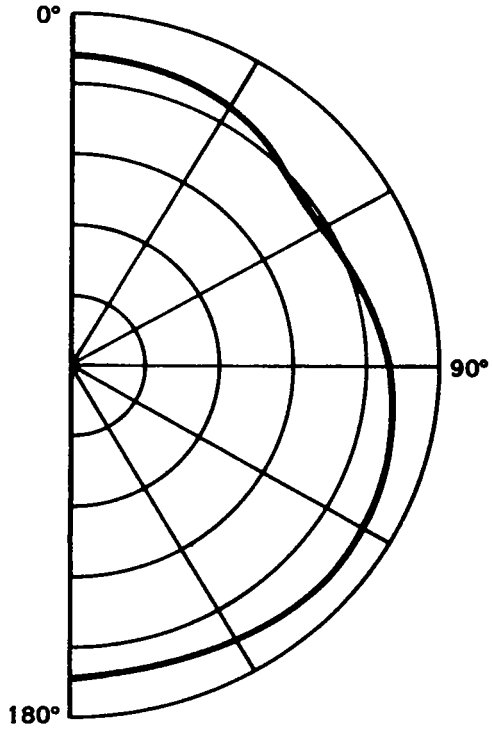
FIGURE 65 EFFECT OF AXIAL LENGTH SCALE OF TURBULENCE ON DIRECTIVITY
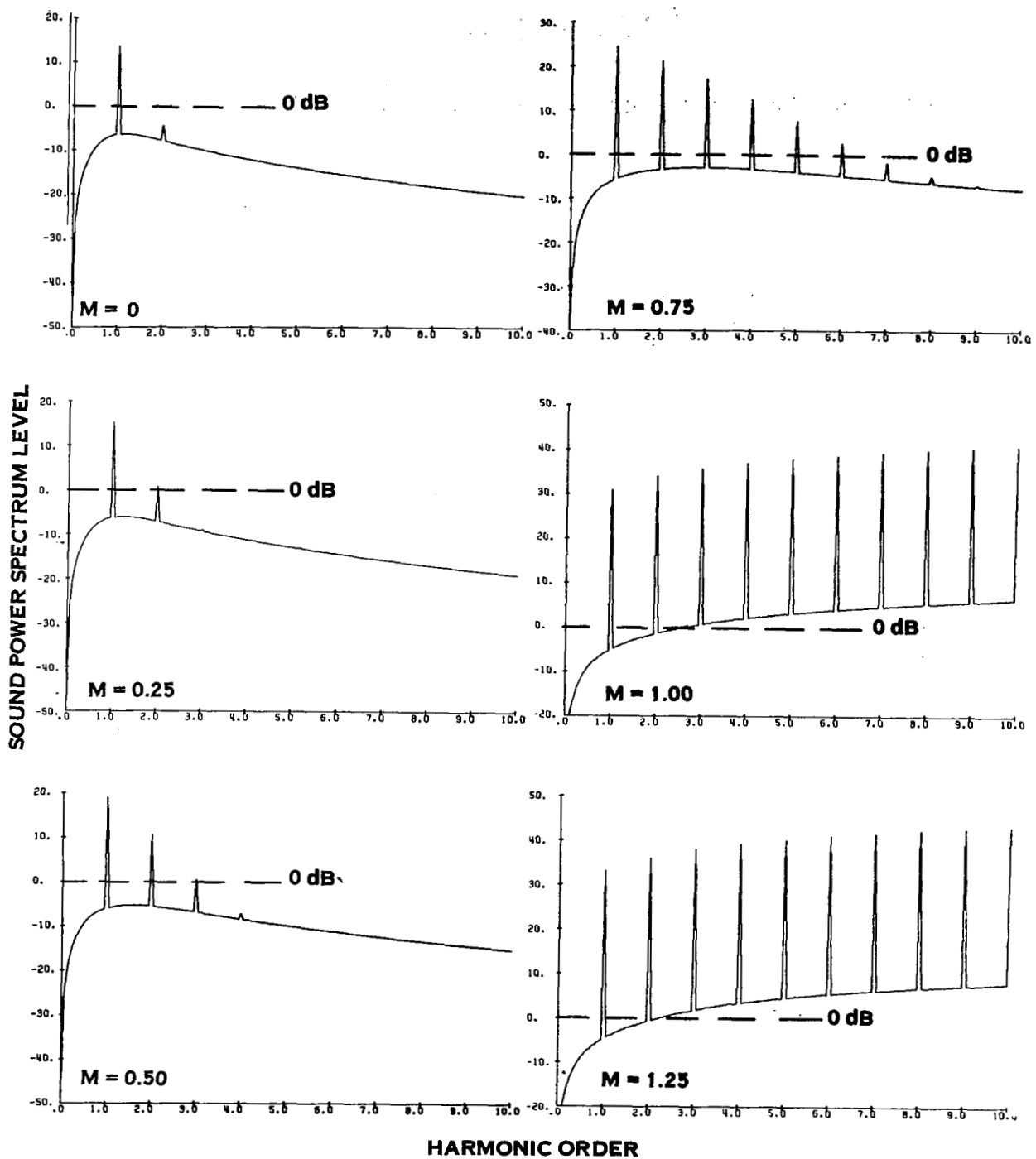
FIGURE 66   EFFECT OF ROTATIONAL MACH NUMBER ON POWER SPECTRUM

126
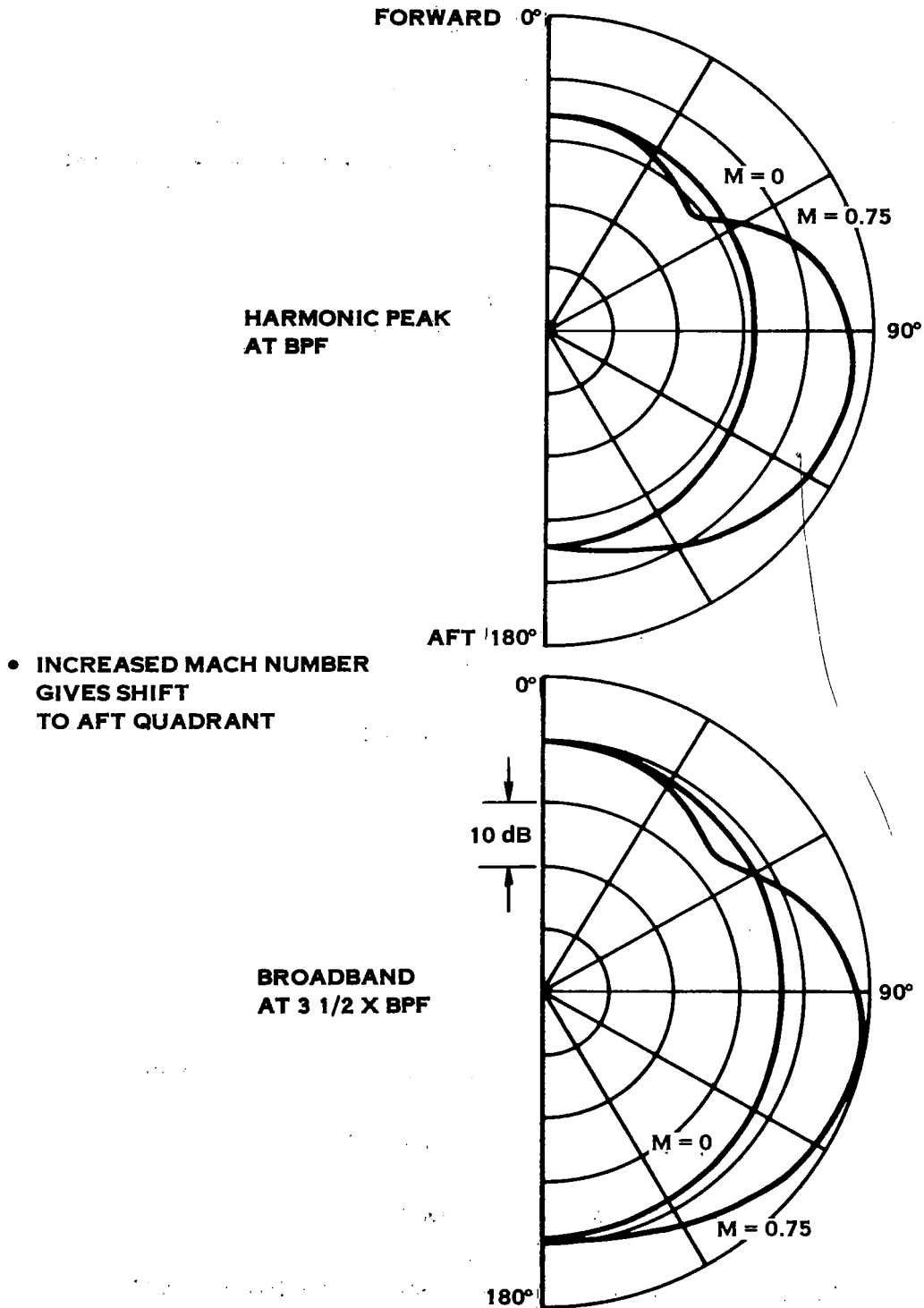
FIGURE 67 EFFECT OF ROTATIONAL MACH NUMBER ON DIRECTIVITY
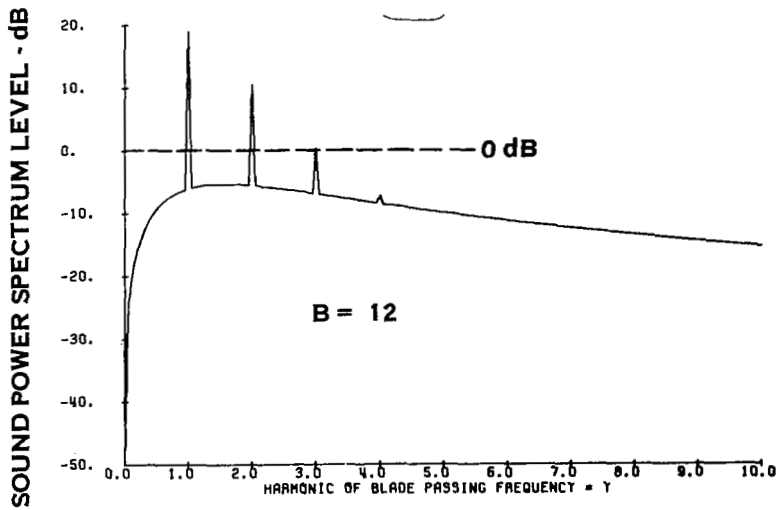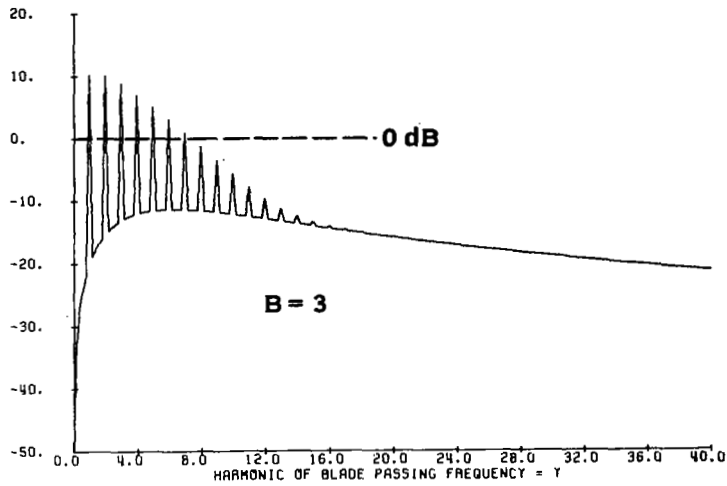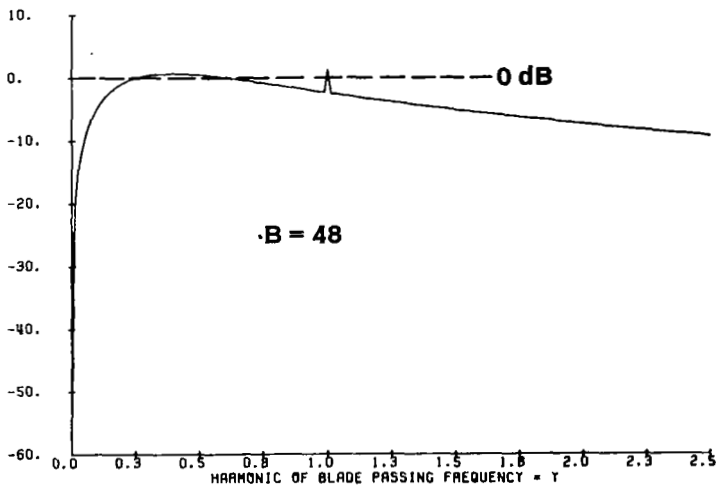
FIGURE 68.   EFFECT OF NUMBER OF BLADES ON POWER SPECTRUM

128

HARMONIC PEAKS
(BPF)

B = 48

B = 3

B = 12

B = 12

B = 48

B = 3
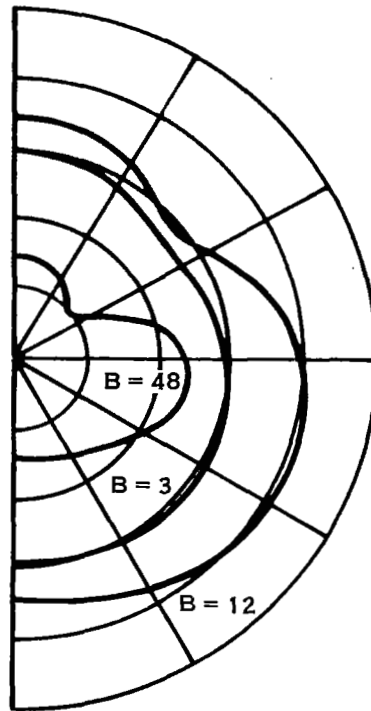
BROADBAND
AT = 1.5 X BPF
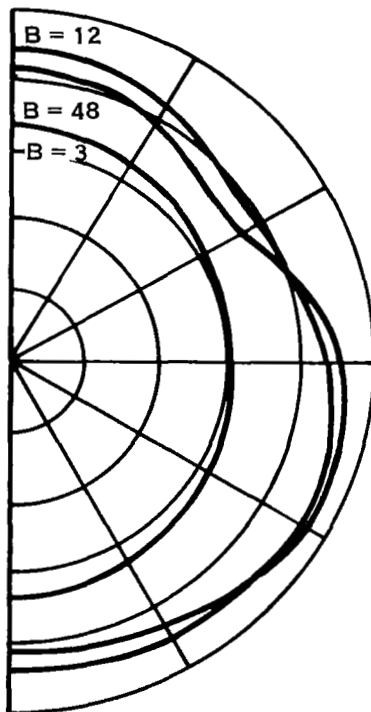
FIGURE 69. EFFECT OF NUMBER OF BLADES ON DIRECTIVITY
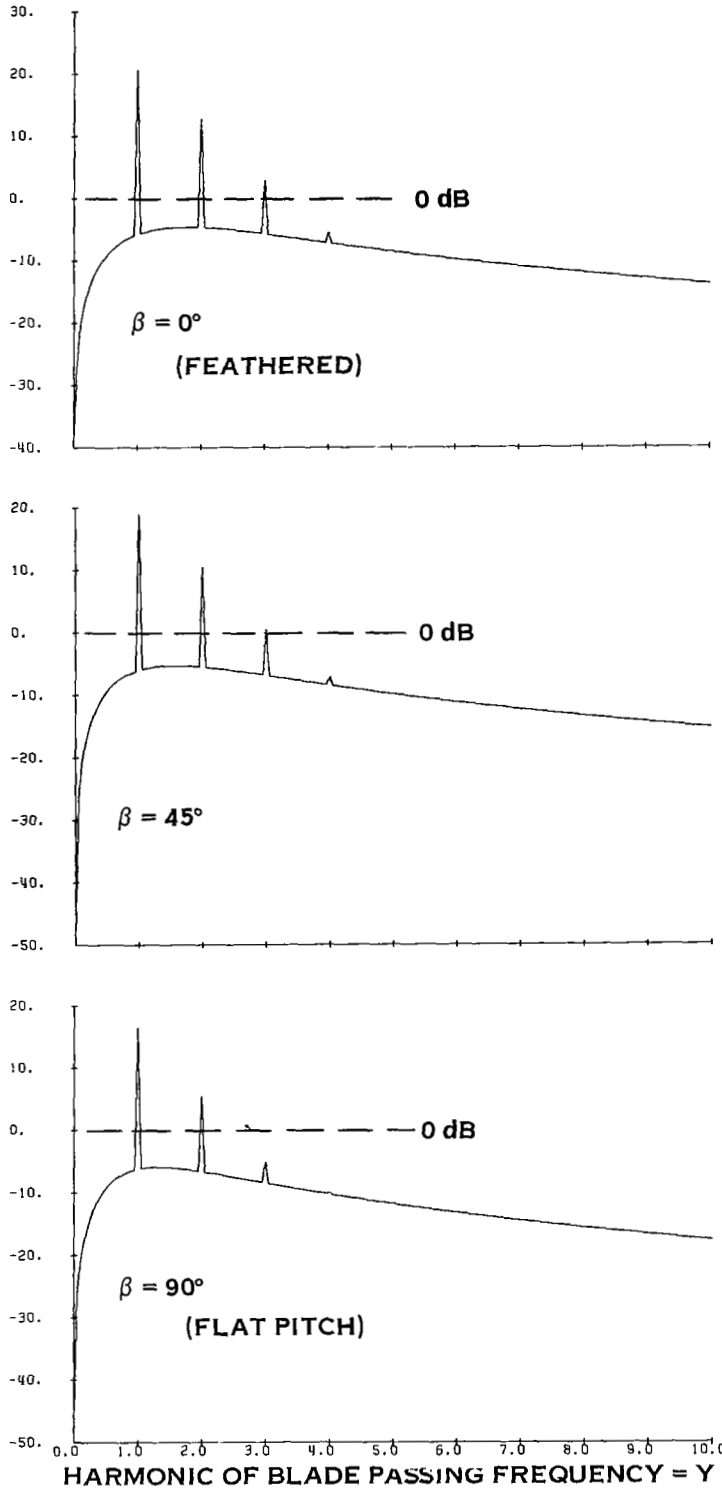
FIGURE 70 EFFECT OF STAGGER ANGLE ON POWER SPECTRUM

130
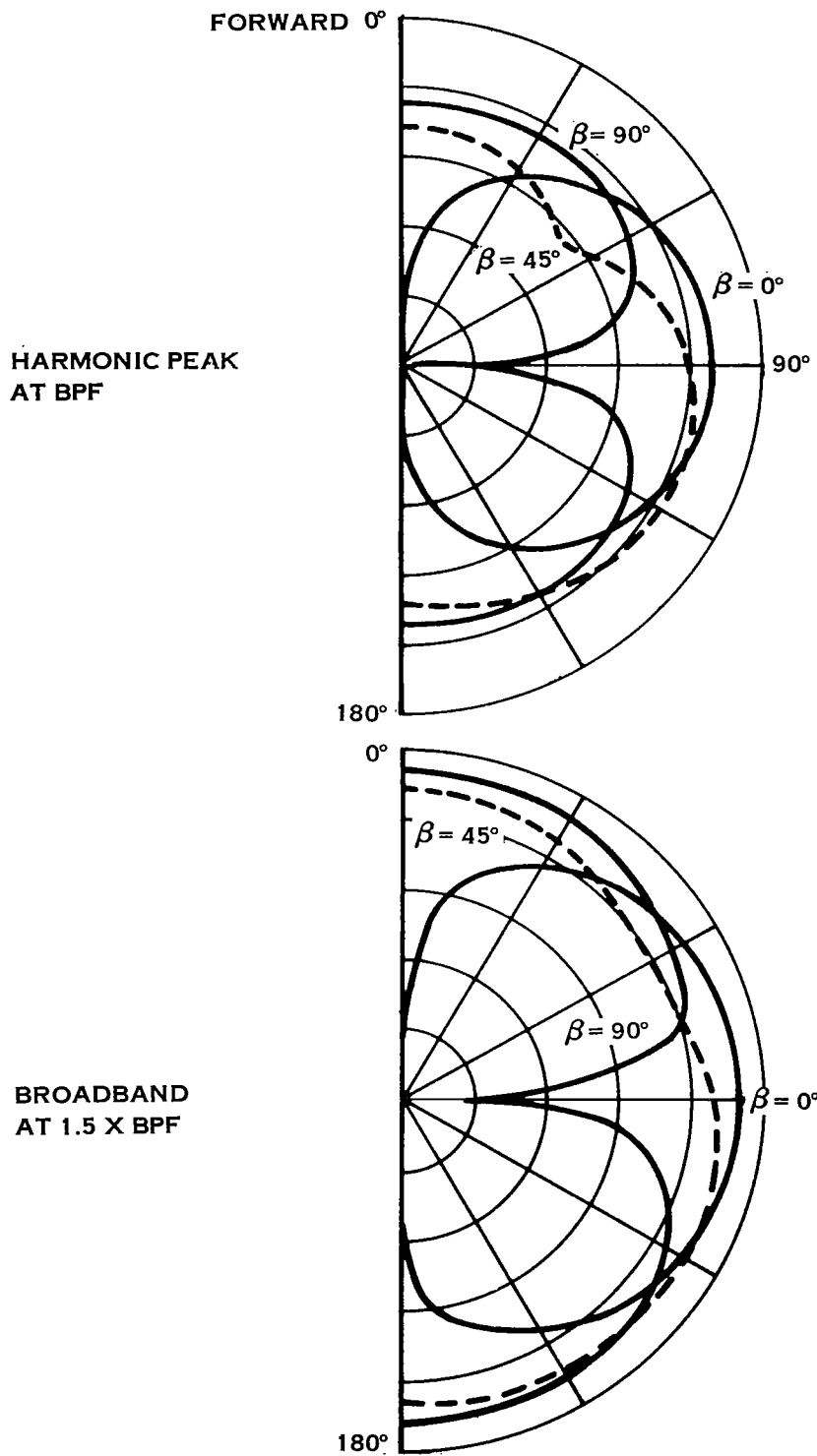
FIGURE 71 EFFECT OF STAGGER ANGLE ON DIRECTIVITY

131

BASE CASE:

Q-FAN DEMONSTRATOR
200 METERS/SEC TIP SPEED

15 HZ SPECTRUM OF SOUND POWER - DB

FREQUENCY – KILOHERTZ
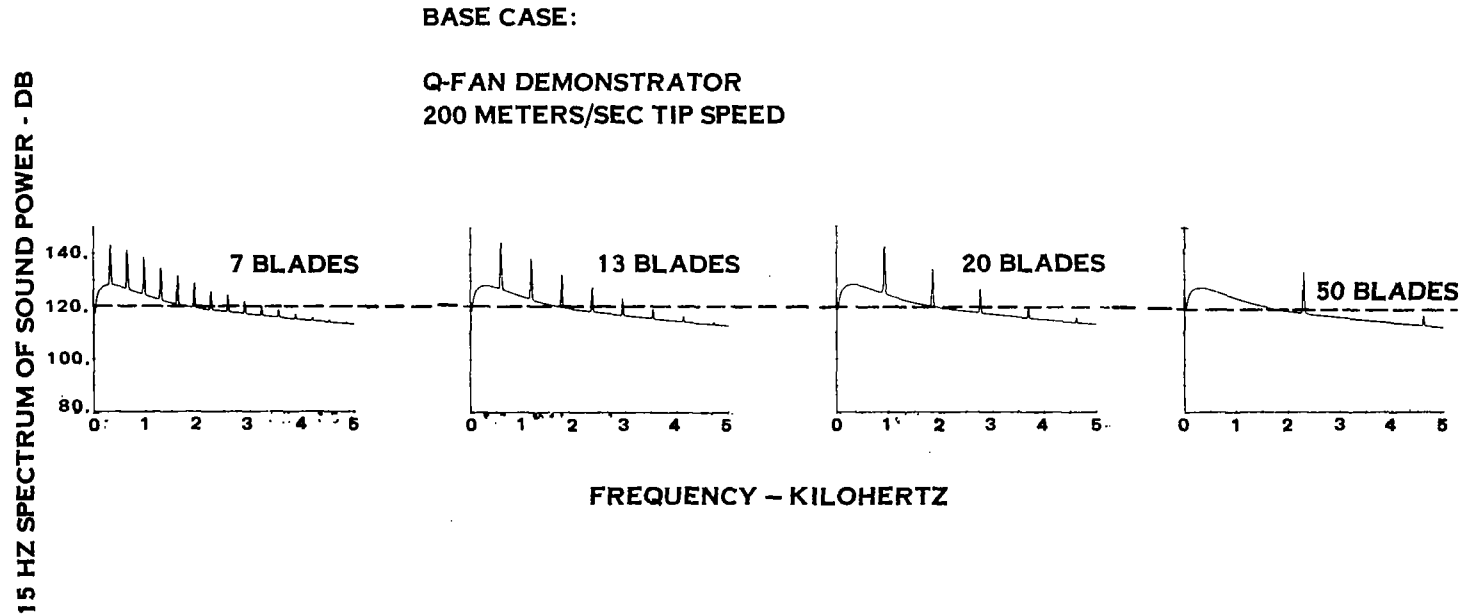
FIGURE 72. EFFECT ON ROTOR NOISE OF CHANGING NUMBER OF BLADES
IN ROTOR DESIGN WITH SOLIDITY HELD CONSTANT –

RESULTS • BROADBAND DOES NOT CHANGE
• PEAK ENERGY REDUCES FOR INCREASED NUMBER OF BLADES

TIP SPEED M/S (FT/S)	ROTOR STAGGER	c_0/c_{BO}	$W_{0.8}$ M/S
150 (492)	31.1°	1.590	183
200 (656)	39.3°	1.000	211
250 (820)	45.4°	0.682	249
300 (984)	50.1°	0.524	277

BASE CASE:
Q-FAN DEMONSTRATOR
200 METERS/SEC

SOUND POWER SPECTRUM (15.0 HZ BW)

150 METERS/SEC 200 METERS/SEC 250 METERS/SEC 300 METERS/SEC

FREQUENCY KILO HERTZ
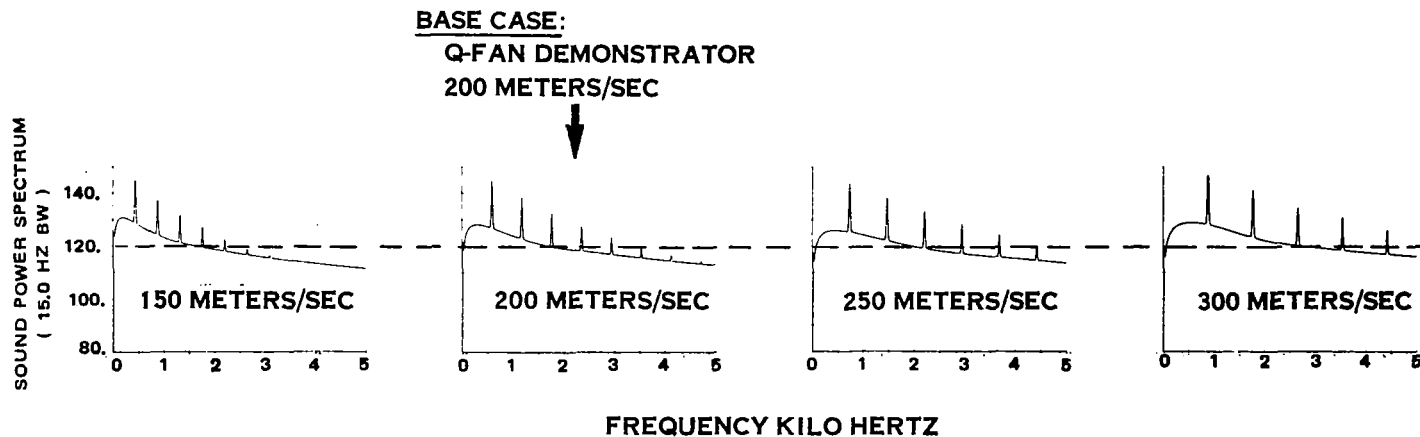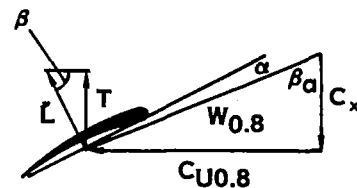
FIGURE 73. EFFECT ON ROTOR NOISE OF CHANGING DESIGN TIP SPEED AT CONSTANT PRESSURE RATIO. BLADE CHORD CHANGED TO HOLD $1/2 \, P \, V^2_{REL} c_B$ CONSTANT.

RESULTS: • PEAK AND BROADBAND LEVELS INCREASE WITH INCREASING DESIGN TIP SPEED.
• FASTEST INCREASE OCCURS NEAR SONIC TIP SPEED.
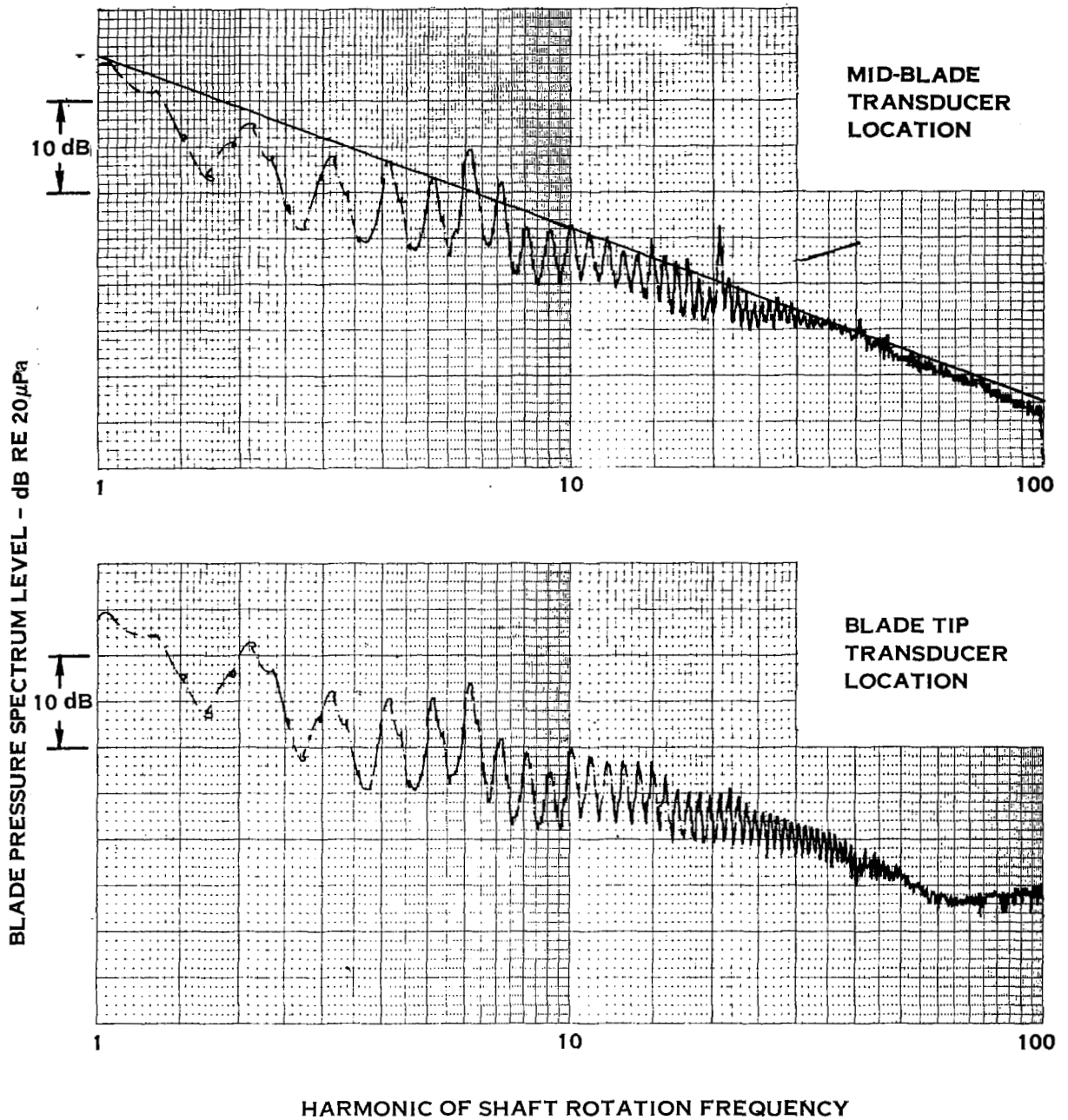
FIGURE 74. BLADE PRESSURE SPECTRA SHOWING STRAIGHT LINE BEHAVIOR OF PEAKS AT MID BLADE LOCATION ON LOG-LOG PLOT. (TEST CONDITION 0-3A).

MID BLADE LOCATION
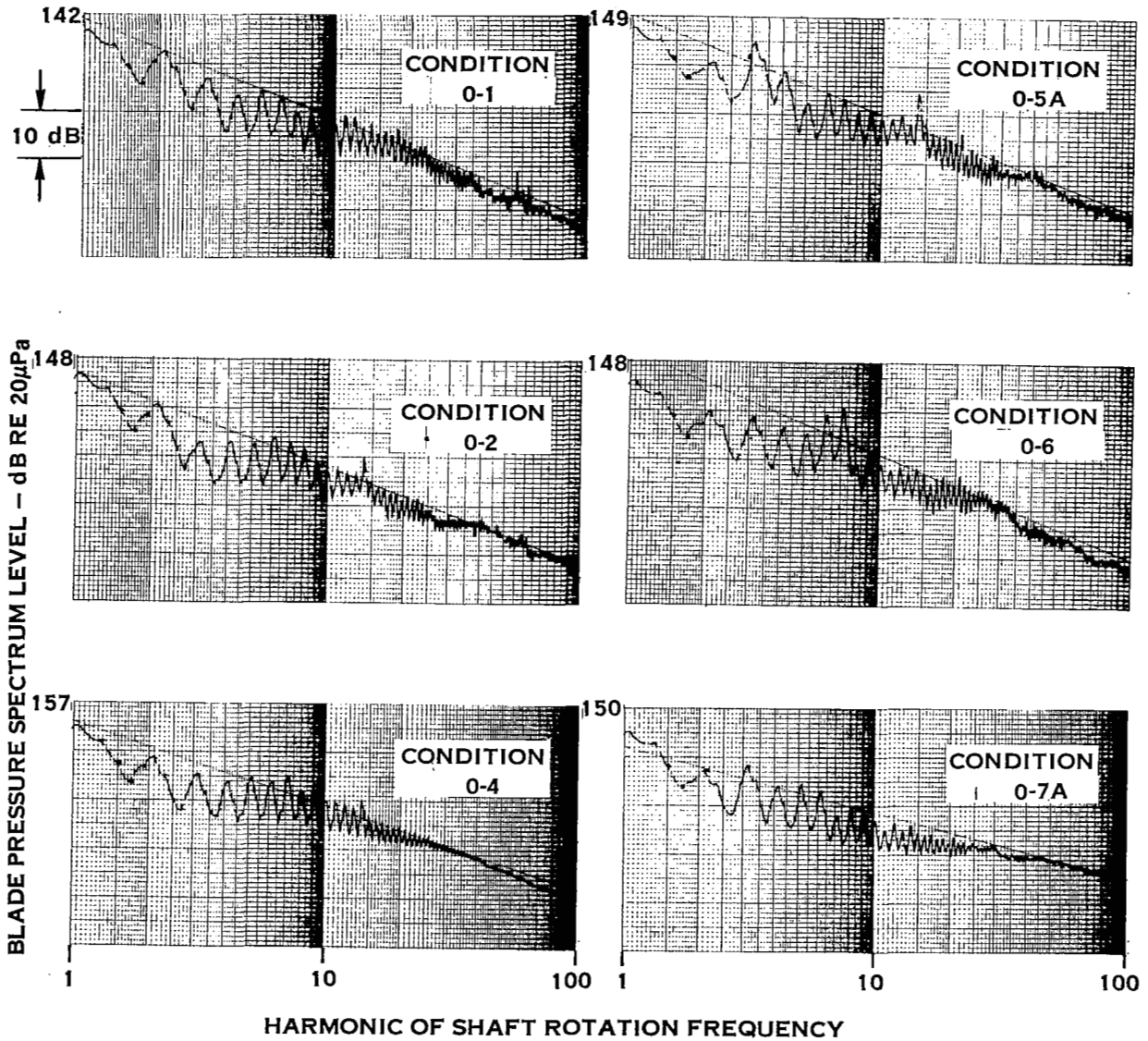
FIGURE 75. BLADE PRESSURE SPECTRA FOR VARIOUS TEST-CONDITIONS-MID BLADE TRANSDUCER LOCATION. (HIGH FREQUENCY PEAKS TEND TO FOLLOW STRAIGHT LINE)

135

BLADE TIP LOCATION
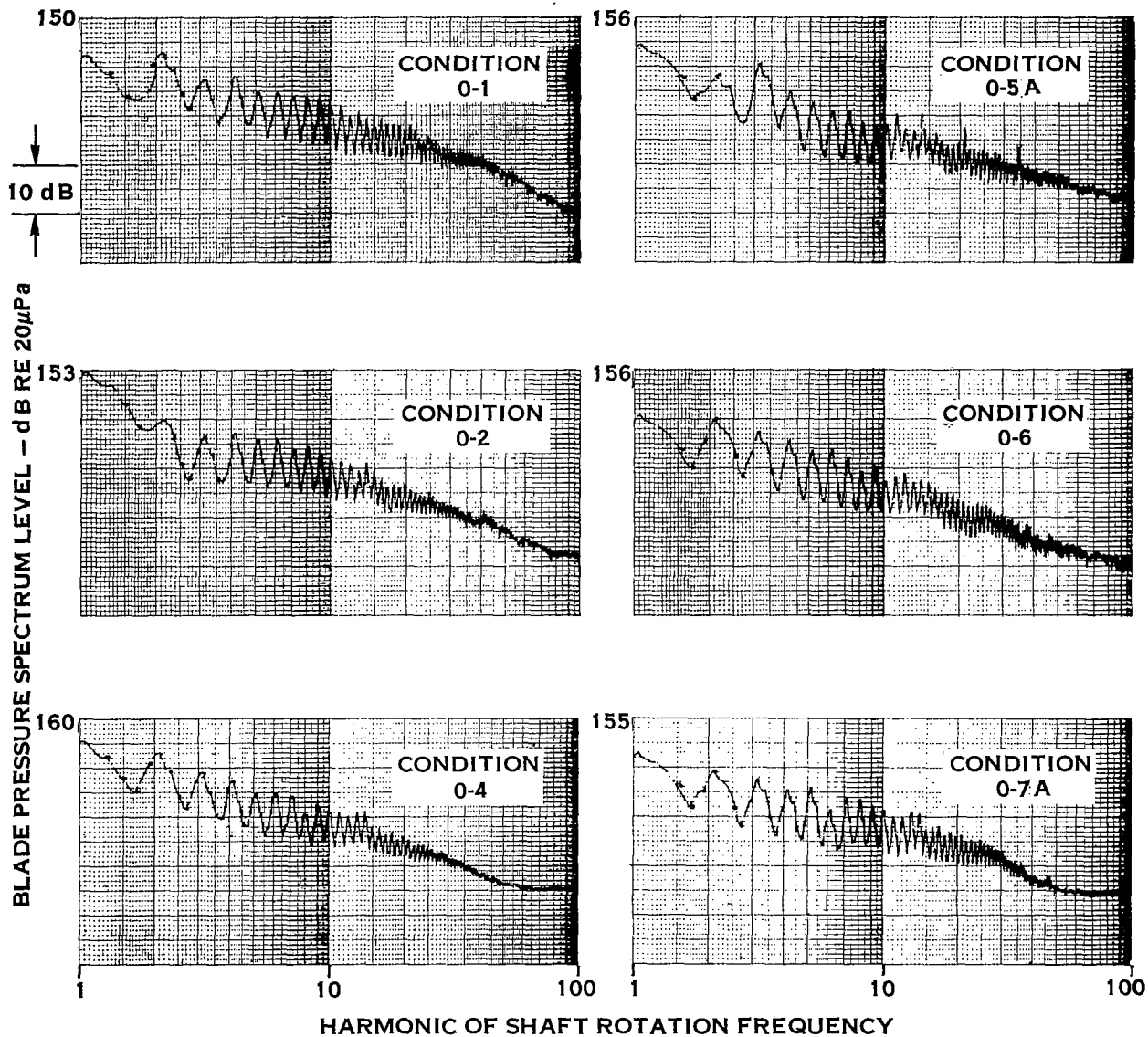
FIGURE 76. BLADE PRESSURE SPECTRA FOR VARIOUS TEST CONDITIONS – BLADE TIP TRANSDUCER LOCATION. (SPECTRUM PEAKS DO NOT TEND TO FOLLOW STRAIGHT LINE CLOSELY)